ONE-POT SYNTHESIS OF HYBRID CORE-SHELL NANOPARTICLES FOR ANTIBACTERIAL PHOTODYNAMIC THERAPY

A THESIS SUBMITTED TO

THE GRADUATE SCHOOL OF ENGINEERING AND SCIENCE

OF BILKENT UNIVERSITY

IN PARTIAL FULFILLMENT OF THE REQUIREMENTS FOR

THE DEGREE OF

MASTER OF SCIENCE

IN

MATERIALS SCIENCE AND NANOTECHNOLOGY

By

Seyed Ehsan Hadi

July 2019

ONE-POT SYNTHESIS OF HYBRID CORE-SHELL NANOPARTICLES FOR ANTIBACTERIAL PHOTODYNAMIC THERAPY
By Seyed Ehsan Hadi
July 2019

We certify that we have read this thesis and that in our opinion it is fully adequate, in scope and in quality, as a thesis for the degree of Master of Science.

Dönüş TUNCEL(Advisor)

Hilmi Volkan DEMİR

Talha ERDEM

Approved for the Graduate School of Engineering and Science:

Ezhan Karaşan
Director of the Graduate School

ABSTRACT

ONE-POT SYNTHESIS OF HYBRID CORE-SHELL NANOPARTICLES FOR ANTIBACTERIAL PHOTODYNAMIC THERAPY

Seyed Ehsan Hadi
M.S. in Materials Science and Nanotechnology
Advisor: Dönüş TUNCEL
July 2019

Multidrug resistance (MDR) in Escherichia coli (E. coli) has become a worrying issue that is not only increasingly observed in humans but also is widespread in veterinary medicine worldwide. Therefore, developing new and effective alternatives to conventional antibiotics has become an imperative need. The idea of using photodynamic therapy (PDT) for bacterial eradication is a solution for the cases that the bacteria are resisting to conventional antibiotics. Although in these cases, PDT can be an option, PDT-killing efficiency might still not be sufficient, and some enhancements are necessary. Metal-enhanced singlet oxygen generation (ME^1O_2) is one of the ways to enhance the PDT-killing efficiency of the E. coli. Hybrid core-shell structures can serve conveniently for this purpose. These structures can combine the flexible and tailorable features of polymers (shell) with the photophysical properties of plasmonic metals (core). In this work, using gold as a core and conjugated oligomer as a shell produced a novel hybrid core-shell nanoparticles which can enhance the singlet oxygen generation capacity and subsequently, improve the PDT-killing efficiency of the E. coli. In this structure, the shell is responsible for the spontaneous reduction of gold ions, forming gold nanoparticles and protecting them from the aggregation. With further investigation and optimization, the hybrid core-shell nanoparticles with the help of ME^1O_2 successfully improved the killing efficiency of E. coli bacteria by 40%.

Keywords: core-shell nanoparticle, antibacterial photodynamic therapy, metal-enhanced singlet oxygen generation, ROS, E. coli, conjugated oligomer, gold nanoparticle.

ÖZET

ANTIBAKTERIYEL FOTODINAMIK TEDAVIYE YÖNELIK HIBRIT ÇEKIRDEK-KABUK NANOPARÇACIKLARININ TEK ADIMDA SENTEZI

Seyed Ehsan Hadi
Malzeme Bilimi ve Nanoteknoloji, Yüksek Lisans
Tez Danışmanı: Dönüş TUNCEL

Temmuz 2019

E. coli bakterisindeki çoklu ilaç direnci (MDR) insanlarda olduğu kadar hayvanlarda da giderek yaygınlaşan endişe verici bir sorun haline gelmiştir. Bu nedenle geleneksel antibiyotiklere alternatif etkili ilaçlar geliştirmek zorunlu hale gelmiştir. Bakterilerin geleneksel antiboyatiklere karşı direnç gösterdiği durumlarda fotodinamik tedaviden (PDT) yararlanma düşüncesi bakterileri yok etmek için bir çözümdür. PDT bu durumlarda bir seçenek olmasına rağmen, bakter-ileri yok etme verimliliği çoğu zaman yeterli değildir ve bir takım iyileştirmeler yapmak gerekmektedir. Metalle artırılmış singlet oksijen (ME^1O_2) üretimi PDT ile E. coli bakterisini öldürme verimliliğini artırma yollarından biridir. Bu tür yapılar, polimerlerin (kabuk) esnek ve ayarlanabilir özelliklerini plasmonik met-allerin (çekirdek) optik, elektronik ve fotofiziksel özellikleriyle bir araya getire-bilir. Bu çalışmada, altını çekirdek olarak kullanıp konjuge oligomeri kabuk olarak kullanarak, yüksek singlet oksijen üretim verimine sahip olan ve E. coli bakterisini öldürme verimi artırılmış hibrit çekirdek-kabuk nanoparçacıkları sen-tezlenmiştir. Bu yapıda kabuk, altın iyonlarının spontane indirgenerek altın nanoparçacıkları oluşturmasından ve agregasyondan korunmasından sorumludur. Detaylı araştırma ve iyileştirmelerle, hibrit çekirdek-kabuk nanoparçacıkları, ME^1O_2'nin de yardımıyla, E. Coli öldürme verimini %40 artırmıştır.

Anahtar sözcükler: çekirdek-kabuk nanoparçacığı, antibakteriyel fotodinamik tedavi, metalle iyileştirilmiş singlet oksijen üretimi, reaktif oksijen türleri, E. coli, konjuge oligomer, altın nanoparçacığı.

Acknowledgement

First of all, I would express my sincere gratitude to my advisor, Prof. Dönüş Tuncel, for the continuous support of my master's study and research. Her guidance helped me to accomplish my thesis, develop my teamwork ability, and improve my academic personality.

I would like to thank the examining committee members, Prof. Hilmi Volkan Demir, and Prof. Talha Erdem, for their encouragement and insightful comments.

I want to extend my sincerest thanks to all faculty members and staff of the Bilkent University National Nanotechnology Research Center (UNAM) who have contributed to my scientific knowledge. I also thank Bilkent University, UNAM, and TÜBİTAK for financial support throughout my master's studies.

I need to express my deepest gratitude to Dr. Yogesh Kumar, Dr. Ahmet Koç, Dr. Rehan Khan, Dr. Aysan Khaligh Vazirabadi, and Dr. Timuçin Balkan for their guidance and support and special thanks to Melis Özkan for her tremendous help.

My sincere thanks go to my friend Abbas Khodadadi, for his support. Also members of the Demir research group and the Elbüken research group, especially Farzan Shabani, Nima Taghipour, Ali Kalantaifard, and Azimet Akber Karluk and many thanks to all friends and individuals who have directly or indirectly contributed to this work.

Finally, I have to offer my most special thanks to my family, especially Sol, for their support and care.

Contents

1 Introduction and Background **1**

1.1 Nanoscience and Nanotechnology 1

1.1.1 Properties 2

1.1.2 Characterization 3

1.1.3 Applications 4

1.2 Conjugated Polymers 5

1.2.1 Properties 5

1.2.2 Application 8

1.3 Plasmonic Nanoparticles 9

1.3.1 Properties and Applications 9

1.3.2 Gold Nanoparticles 10

1.4 Core-Shell Nanostructures 13

1.4.1 Synthesis of Core-Shell Nanoparticles 13

1.4.2 Properties 14

1.4.3 Applications 15

1.5 Colloidal Systems 16

1.6 Photothermal Therapy 19

1.7 Photodynamic Therapy 21

1.7.1 Metal-Enhanced Singlet Oxygen Generation (ME^1O_2) . . . 24

1.8 E. coli bacteria 26

1.9 Previous Works with Red-Emitting Conjugated Oligomer 27

2 Introduction to measurement techniques 28

2.1 Dynamic Light Scattering and Zeta Potential 28

2.2 Ultraviolet-visible Spectroscopy 32

2.3 X-ray Diffraction 34

2.4 Fluorescence Spectroscopy 36

2.5 Time-resolved Fluorescence Lifetime 38

2.6 X-ray Photoelectron Spectroscopy 39

2.7 Transmission Electron Microscopy 42

2.8 Scanning Electron Microscopy 44

2.9 Critical Point Dryer 46

2.10 Microplate reader 47

2.11 Fourier-transform Infrared Spectroscopy 48

3 Experimental 50

3.1 Materials 50

3.2 Synthesis 50

3.2.1 Synthesis of Red-Emitting Oligomer 50

3.2.2 Dispersion of Conjugated Oligomer Nanoparticles in Water 53

3.2.3 Synthesis of Hybrid Core-Shell Nanoparticles 54

3.3 Antibacterial Assays 55

3.3.1 Preparation of the Bacterial Solution and Minimum Inhibitory Concentration (MIC Assay) 55

3.3.2 Biocidal activities of COL and Au@COL nanoparticles toward E. Coli 56

3.3.3 Preparing the bacteria for imaging 56

3.3.4 Zeta Potential Measurements 57

3.3.5 ROS Measurements 57

3.4 Instrumentation 58

3.4.1 Transmission Electron Microscopy 58

3.4.2 Scanning Electron Microscopy 58

3.4.3 UV-Vis Absorbance Spectroscopy 58

3.4.4 Fluorescence Spectroscopy 59

3.4.5 Time-Resolved Fluorescence Spectroscopy 59

3.4.6 X-Ray Powder Diffraction 59

3.4.7 X-Ray Photoelectron Spectroscopy 59

3.4.8 Dynamic Light Scattering and Zeta Potential 60

3.4.9 Critical Point Dryer 60

3.4.10 Microplate reader 60

3.4.11 FT-IR Spectroscopy 61

4 Results and Discussion 62

4.1 Aim of the Study 63

4.2 Characterization 64

4.2.1 Characterization of Red-Emitting Conjugated Oligomer . . 64

4.2.2 Characterization of Water-dispersed Conjugated Oligomer Nanoparticles 68

4.2.3 Characterization of Water-dispersed Au@COL Nanoparticles 74

4.3 Interpretation of Characterization Data 83

4.3.1 Optical properties 84

4.3.2 Structural Analyses 87

4.3.3 Morphology, Size, and Surface Properties 91

4.3.4 Stability of the Au@COL nanoparticles aqueous solution over the time 92

4.4 Application of Au@COL Nanoparticles 93

4.4.1 Investigation of PDT-killing of E. coli 93

5 Conclusion **103**

5.1 Future works 104

List of Figures

1.1 Plot of the number of articles published on "nano" since 1992. . . 2

1.2 Molecular structures of typical conjugated polymers. 5

1.3 Band formation from molecular repeat unit to π-conjugated polymer. 6

1.4 Jablonski diagram demonstrating fluorescence and competing pathways for molecular relaxation from an excited state. 7

1.5 Effective parameters on the properties of CSNs. 15

1.6 Applications of CSNs. 16

1.7 Electrostatic stabilization of colloids. 18

1.8 Steric stabilization of colloids. 18

1.9 Scheme of PTT-Killing of E. coli bacteria. 20

1.10 Dissipation of energy through plasmon-mediated transformation mechanisms caused by SPR. 20

1.11 Jablonski diagram of small molecule PS for generation of $^1O_2$. . . 22

1.12 Jablonski diagram of conjugated polymer PS for generation of $^1O_2$. 22

1.13 A simplified scheme of the mechanism of PDT-induced tumor destruction. 23

1.14 Modified Jablonski diagram of the photosensitizer and metal-enhanced singlet oxygen generation. 25

1.15 The expected performance of Au@COL and COL nanoparticles in the singlet oxygen generation. 25

2.1 Scheme of working principle of DLS. 28

2.2 The Illustration of zeta potential. 32

2.3 XRD pattern of a semi-crystalline material. 35

2.4 Schematic diagram of the main components of TEM. 43

2.5 Schematic diagram of the main components of SEM. 45

3.1 A simplified scheme of the synthesis of the red-emitting oligomer. 51

4.1 FT-IR spectrum of COL. 64

4.2 UV-Vis absorbance and fluorescence spectra of COL dissolved in THF. 65

4.3 Photoluminescence decay curves of COL dissolved in THF. 66

4.4 The XPS spectra of COL. 67

4.5 FT-IR spectrum of COL nanoparticles. 68

4.6 UV-Vis absorbance and fluorescence spectra of COL nanoparticles in water. 69

4.7 Photoluminescence decay curves of COL nanoparticles in water. . 69

4.8 DLS and zeta potential results of COL nanoparticles in water. . . 71

4.9 SEM images of water-dispersed COL nanoparticles. 72

4.10 The XPS spectra of water-dispersed COL nanoparticles. 73

4.11 The FT-IR spectrum of Au@COL nanoparticles. 74

4.12 UV-Vis absorbance and fluorescence spectra of Au@COL nanoparticles in water. 75

4.13 Photoluminescence decay curves of Au@COL nanoparticles in water. 75

4.14 DLS and zeta potential measurements of Au@COL nanoparticles in water. 77

4.15 TEM and HAADF-STEM images of Au@COL nanoparticles. . . . 78

4.16 EDX spectrum and HAADF-STEM images of Au@COL nanoparticles. 79

4.17 The XPS spectra of water-dispersed Au@COL nanoparticles. . . . 81

4.18 X-ray diffraction pattern of Au@COL nanoparticles. 82

4.19 Suggested mechanism of reduction of gold ions and formation of gold atoms. 83

4.20 The scheme of formation of gold nanoparticles inside the shell. . . 84

4.21 UV-Vis absorbance and fluorescence spectra of COL dissolved in THF, COL nanoparticles in water, and Au@COL nanoparticles in water. 85

4.22 Photoluminescence decay curves of COL dissolved in THF, COL nanoparticles in water, and Au@COL nanoparticles in water. . . . 86

4.23 Quantum yield and fluorescence lifetime comparison bar charts of all structures. 86

4.24 FT-IR spectra of COL, water-dispersed COL nanoparticles, and water-dispersed Au@COL nanoparticles. 87

4.25 Comparison XPS diagram of COL dissolved in THF, COL nanoparticles in water, and Au@COL nanoparticles in water. . . . 89

4.26 HRTEM image of a gold nanoparticle. 90

4.27 UV-Vis absorbance and fluorescence spectra of aged core-shell, aged raspberry structure, and mixture of both structures. 92

4.28 The formation of DCF from DCFH in the presence of ROS such as singlet oxygen. 94

4.29 PL spectra of DCF and time response curve of PL intensity of DCF in the absence and the presence of (3.1 μM) COL nanoparticles under continuous white light irradiation. 95

4.30 PL spectra of DCF and time response curve of PL intensity of DCF in the absence and the presence of (3.1 μM) Au@COL nanoparticles under continuous white light irradiation. 95

4.31 Time response curve of PL intensity of DCF in the presence of Au@COL and COL nanoparticles. 96

4.32 MIC assay for different concentration of Au@COL and COL nanoparticles under white light irradiation. 97

4.33 Biocidal activities of COL nanoparticles toward E. coli in the dark and under light irradiation. 98

4.34 Biocidal activities of Au@COL nanoparticles toward E. coli in the dark and under light irradiation. 99

4.35 SEM images of E. coli in the dark and under light irradiation. . . 100

4.36 SEM images of E. coli treated with COL nanoparticles in the dark and under light irradiation. 100

4.37 SEM images of E. coli treated with Au@COL nanoparticles in the dark and under light irradiation. 101

4.38 Zeta potential comparison bar chart of E. coli upon the addition of COL and Au@COL nanoparticles in the dark and under light irradiation. 102

List of Tables

2.1 Electron levels and corresponded degeneracy. 41

4.1 The overall optical properties of COL dissolved in THF, COL nanoparticles in water, and Au@COL nanoparticles in water. . . . 85

4.2 Summary of reported sizes and calculated zeta potentials. 91

Chapter 1

Introduction and Background

1.1 Nanoscience and Nanotechnology

Nanometer word consists of two words Nano (Nanos), which means "dwarf" in ancient Greek and meter (Metron), which means "unit of measurement" in ancient Greek. It represents 10^{-9} m in International System of Units (Système international d'unités, SI) [1]. Nanotechnology is a broad term referring to more of an approach to engineering than a science; however, it requires multidisciplinary knowledge in materials science, chemistry, physics, and biology. Nanotechnology is going to revolute these sciences affectedly [2]. Nanotechnology has grown rapidly, and its bright future will attract many scholars [3]. According to Figure 1.1, the number of published articles on "nano" has increased from 6,075 in 2000 to 71,458 in 2018.

The 1925 Nobel Prize winner, Richard Adolf Zsigmondy, was the first who proposed the concept of the nanometer. Richard Feynman, the 1965 Nobel Prize winner, introduced the modern nanotechnology. The concept of manipulating matter at the atomic level was presented in 1959 in his lecture titled, "There is Plenty of Room at the Bottom". In 1974, the "nanotechnology" term firstly used by a Japanese scientist, Norio Taniguchi, to define semiconductor processes that

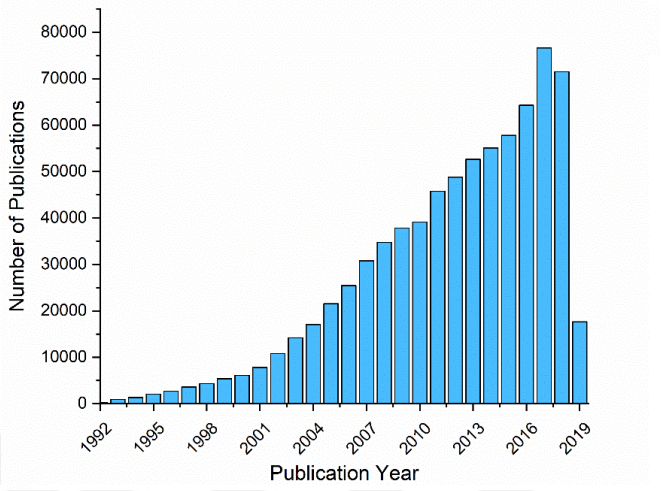


Figure 1.1: Plot of the number of articles published on "nano" since 1992. Source: Web of Science, as of July 2019.

have been conducted on the order of a nanometer. The golden era for nanotechnology began in the 1980s when Curl, Kroto, and Smalley discovered fullerenes. In the same decade, Eric Drexler used the term "nanotechnology" in his 1986 book titled, "Engines of Creation: The Coming Era of Nanotechnology" [4]. Looking at nature can be very helpful for a better understanding of the nanoworld. The diameter of a typical virus, an E. coli bacteria, and a hair are around 60-250 nm, 1,000-2,000 nm, and 50,000-100,000 nm, respectively. The smallest size that the naked eye can resolve is in the range of 55,000-75,000 nm depending on the conditions [5].

1.1.1 Properties

As we go to the nanoscale (within the range of 1-100 nm), the materials might show some extraordinary properties. All nanosystems obey the perfect law of nanomaterials. This law can be elaborated in a simple language: "Existence is perfect, and only the perfect can be existent." But, what does it mean in reality? For answering this question, it is better to take a look at the magic number rule of nanocrystals. According to this rule, only the atom clusters with the number of atoms of 13, 55, 147 and others are considered stable [6]. The same scenario can

be seen in carbon atoms. The probability of the existence of carbon 60 (C_{60}) and carbon 70 (C_{70}) in the fullerene structure is much higher than carbon 59 (C_{59}) and carbon 71 (C_{71}) [5], [7]. In macroscopic materials, most of the parameters like lattice constant, bond length, bond angle, the energy band, quantum state, and distribution function, are well determined. In nanoscale, however, most of the parameters may alter as the number of atoms changes, and this makes working with nanomaterials harder in comparison to macroscopic materials. This characteristic of nanomaterials also makes them incredibly tunable for getting new and different properties. Some examples will make previous statements more understandable. Some metals will lose their thermal and electrical conductivity as they are reduced down to the nanoscale [8]. Fe-Co alloy nanoparticles show significant enhancement in electrocatalytic activity compared to bulk alloys [9]. One of the most interesting size-properties dependence of materials belongs to gold. The conventional melting point of gold is 1,064 °C. However, gold nanoparticle with a size of 10 nm has a melting point of 927 °C. If the size of the gold nanoparticles reduces to 2 nm, surprisingly, the melting point will be 327 °C [10]. Another critical parameter in nanomaterials is the surface area to volume ratio of particles. As a rule, the higher the surface area to volume ratio, the higher the activity of the surface. This high activity can be explained with higher surface energy. High surface energy is not always a desirable characteristic. When the particles become smaller, the number of atoms at the surface in comparison to the internal atoms will be higher. This unbalanced distribution of atoms will result in high surface energy and eventually, instability. In order to confront instability and minimize the total energy of the system, the particles would like to combine with other particles and produce new particles with less surface area to volume ratio.

1.1.2 Characterization

Here is a concise explanation of some of the characterization techniques. More details regarding the characterization techniques can be found in chapter 2. Characterization is one of the most vital tasks when we deal with nanomaterials. As mentioned, some known macroscopic properties will not be valid in nanoscale,

and developing new methods to characterize nanomaterials is essential. Surface characterization, particle composition, crystallinity, size distribution, morphology, optical, electrical, mechanical, and other properties will be covered in a full characterization of nanomaterials. The most appealing characterization of nanomaterials is their morphology. Electronic microscopes and rarely optical microscopes can be used for this purpose. Optical microscopes due to their working principle cannot resolve objects smaller than 200 nm [11], [12]. Electronic microscopes, however, can resolve objects up to 4 angstroms (the size of an atom is in the range of 1 to 5 angstroms). Scanning Electron Microscope (SEM) and Transmission Electron Microscope (TEM) are the most common electronic microscopes used for imaging nanomaterials. Energy Dispersive X-Ray Spectroscopy (EDX) and X-Ray Photoelectron Spectroscopy (XPS) are two of the most useful techniques for surface characterization of nanomaterials. XPS can also be used for detecting the chemical bonds and the oxidation states. For determining the optical properties of nanomaterials, UV-Vis spectroscopy is an accurate technique. UV-Vis can provide handy information, which can be used for estimation of the size of nanoparticles, chemical structure, concentration, reaction kinetics [13], and the magnitude of the bandgap of compounds [14]. Crystallinity, crystal structure, and phase identification of nanomaterials can be monitored with the X-Ray Powder Diffraction (XRD) technique. Crystallinity and hardness are directly proportional. For some applications that hard material is desirable. XRD can also be helpful for monitoring the progress of synthesis [15], [16].

1.1.3 Applications

Nanomaterials, because of their exceptional properties compared to macroscopic materials, have a privilege to be used in a variety of applications. Some materials in nanoscale show completely different properties, which opens new windows for the scientists to utilize these new properties in many applications. Application of nanotechnology in the cancer therapy and imaging [17], [18], advanced dental materials [19], construction [20], cosmetics [21], water and wastewater treatment [22], and drug delivery [23] are proved. Nanotechnology has become

increasingly used for killing or reducing the activity of many microorganisms [24]. The mentioned applications are only a small portion of the potential applications of nanotechnology.

1.2 Conjugated Polymers

Conjugated polymers are organic macromolecules that are characterized by a backbone chain of alternating single and double bonds. Their overlapping p-orbitals create a system of delocalized π-electrons [25]. The term "conjugated" was invented in 1899 by Johannes Thiele [26]. The good examples of conjugated molecules can be conductive or fluorescent polymers and oligomers. Although, the first conjugated polymer named Polyaniline (PAN) was synthesized by Runge in 1834, further serious studies on conjugated polymers conducted after the 1950s [27], [28]. Figure 1.2 shows the molecular structures of Polypyrrole (PPy), Polythiophene (PT), Polyamide (PA), Polyaniline (PANI), Poly(p-phenylene vinylene) (PPV), and Poly(3,4-ethylene dioxythiophene) (PEDOT).

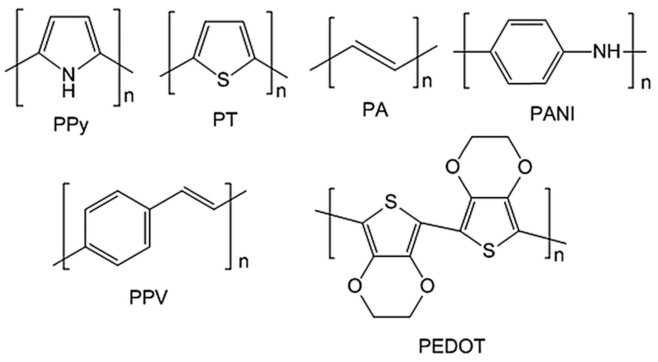


Figure 1.2: Molecular structures of typical conjugated polymers.

1.2.1 Properties

Due to the presence of π-electrons delocalized along the polymer chain, their electronic properties are different from typical polymers. Conjugated polymers

are semi-conductive; however, the typical polymers are insulators. This metal-like behavior of conjugated polymers is because of their delocalized electrons [29]. The highest occupied molecular orbital (HOMO) is formed by the π-electrons of the conjugated polymer in the ground state. Lowest unoccupied molecular orbital (LUMO) is another free energy state which its energy is higher than HOMO. The energy difference between these levels is called the bandgap. The π-electrons can travel through this gap when they are excited ($\pi\pi^{\star}$ electrons). The magnitude of this bandgap is significant since it indicates the electrical and optical properties of the material. Semiconductors have a bandgap in the range of 0.5 to 3.5 eV, which provides unique and tunable optical and electrical properties to these materials [30].

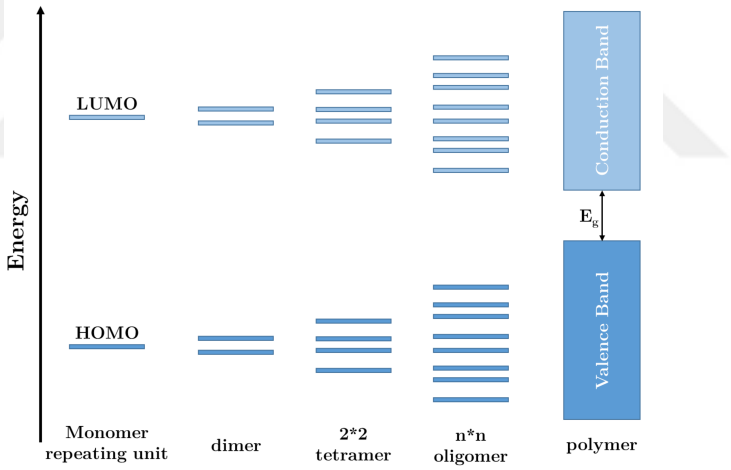


Figure 1.3: Band formation from molecular repeat unit to π-conjugated polymer.

When a conjugated polymer is exposed to light, which is an electromagnetic wave, the electrons can go to an excited state if the energy (frequency) of light is enough for the excitation. The absorbed energy allows the electrons to travel from HOMO to LUMO. When the electrons are in this excited state, they are extremely unstable and tend to come back to the ground state to reduce their energy and gain stability. The relaxation of electrons from an excited state to the ground state can happen in two possible ways: fluorescence and phosphorescence. Fluorescence occurs when the electrons in the singlet-excited state directly travel back (relax) to singlet ground state. During this relaxation process, photons lose some energy because of internal conversions of energy (vibrational relaxation and

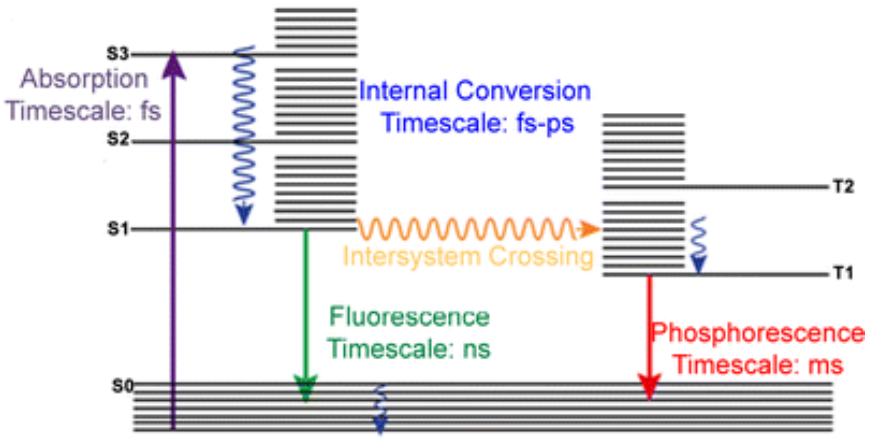


Figure 1.4: Jablonski diagram demonstrating fluorescence and competing pathways for molecular relaxation from an excited state. Reprinted with permission from [31]. Copyright (2015) American Chemical Society.

the heat lost to the environment), so the emitted energy (frequency) will be less than the absorbed energy. Fluorescence is the primary emission pathway for conjugated polymers. If the excited state electrons follow a nonradiative relaxation pathway from singlet-excited state to triplet-exited state, the intersystem crossing will happen. The radiative relaxation from triplet-excited state to singlet ground state is called phosphorescence. All these phenomena are represented as the Jablonski energy diagram in Figure 1.4.

To use conjugated polymers or oligomers in applications such as drug delivery or cell labeling, they should be water-soluble [32]. Most of these conjugated polymers due to lack of polar functional groups are not water-soluble, so the best way to use them in aqueous systems (biomedical applications) is to make them water dispensable and make a stable colloidal solution out of them. The most typical way to make them water-dispersed is fabricating their nanoparticles. Fabrication of water-dispersed conjugating polymer nanoparticles can be done in two common ways: nanoprecipitation technique and miniemulsion. In the miniemulsion method, the conjugated polymer, which is dissolved in a water-immiscible solvent, is added to an aqueous surfactant solution under ultrasonication. In this case, the size of nanoparticles will be in the range of 30-500 nm depending on the power of ultrasonication and its duration. In the nanoprecipitation technique,

the hydrophobic polymer is dissolved in a good organic solvent such as THF or DMSO and then gradually added (dropwise) to a poor solvent such as water, under ultrasonication. As the hydrophobic polymer or oligomer enters the water, to prevent itself from interacting with water or at least minimize this interaction tries to form spherical nanoparticles. The size of nanoparticles, in this case, depends on the concentration of polymer in the good solvent, amount of the water, temperature, and pH of solutions, power and duration of ultrasonication, and rate of evaporation of the organic solvent from the final solution. With this method, nanoparticles smaller than 100 nm can be formed. The advantage of this method is that it does not require any other additives such as surfactants [33].

1.2.2 Application

The bandgap of conjugated polymers can be modified to obtain the desired optical properties. These optical and other exceptional properties allowed the conjugated polymers to be used in vast kinds of applications. The applications of conjugated polymer nanoparticles have been demonstrated in energy [34], catalysts for photocatalytic hydrogen evolution [35], electroluminescent devices [36], optoelectronics [37], and biomedical [38].

1.3 Plasmonic Nanoparticles

Nanoparticles, whose electron density can couple with the electromagnetic waves having wavelengths larger than the particles, can be called plasmonic nanoparticles [39]. Depending on the size and geometry of plasmonic nanoparticles, they can show remarkable absorption, scattering, and coupling properties, which will enable them to be exploited in many applications.

1.3.1 Properties and Applications

Some of the metal nanoparticles display resonance in the visible region, which can enable them to absorb a portion of the visible light spectrum. Their solutions exhibit vivid colors due to a phenomenon called localized surface plasmon resonance (LSPR). Gold (Au) [40] and silver (Ag) [41] nanoparticles have a quite strong resonance in visible range. Copper (Cu) nanoparticles [42] also show a great resonance, but because of surface oxidation, they are not stable. Resonance of palladium (Pd) and platinum (Pt) nanoparticles are weak in visible region [43]. Resonance of aluminum (Al) nanoparticles occurs in the UV region [44], which is used in a variety of applications. As mentioned earlier, the shape and size of plasmonic nanoparticles are affecting their optical properties. Optical properties of the nanomaterials are also tightly bonded to their electronic configuration and physical structure. For instance, quantum confinement in semiconductor nanoparticles like CdSe causes a shift in its emission spectra [45]. As the size of semiconductor particle decreases below its Bohr radius, the electrons will be more confined in the material. This confinement will increase the bandgap of the material. The Bohr radius of CdSe is 5.6 nm [46], which means if the particle size goes smaller than 5.6 nm, the emission shifts to lower wavelengths. The optical properties of plasmonic nanoparticles can be explained with the help of Surface Plasmon Resonance (SPR). When a plasmonic metal nanoparticle is irradiated by light, the oscillating electric field causes the free electrons (electrons in conduction band) to oscillate coherently. This oscillation frequency depends on the density of electrons, the effective electron mass, dielectric constants of both

the medium the metal, and the shape and the size of the charge distribution at the surface, which corresponds to the shape and size of the nanoparticle. The resonance can occur more effectively for shorter wavelengths in smaller and more spherical particles. Thus, a solution of 20 nm spherical gold nanoparticles is red. For gold and silver nanoparticles, this frequency is in the visible region. This will allow estimating the shape and the size of the nanoparticles with UV-Vis spectroscopy. As the size of nanoparticles increases, the absorption occurs in lower energies (red region) and the solution color will be bluer. If the shape of the gold nanoparticles changes from spherical to non-spherical, e.g., urchin shape, the color of the solution changes to blue since the urchin shape particles are a better scatterer rather than an absorber [47], [48]. Changing the environment of nanoparticles will change the plasmonic resonance frequency; therefore, capping nanoparticles with organic and/or inorganic materials (core-shell nanostructure) can cause a significant shift in surface plasmon absorption maximum [49]. Studies also showed that increasing the dielectric constant of the surrounding medium will make the SPR peak broader [50]. The wide-ranging tunable optical properties of plasmonic nanoparticles enabled them to be tuned for specific applications. The application of the plasmonic nanoparticles has proved in biomedical [51], energy conversion [52], and surface-enhanced Raman spectroscopy (SERS) [53].

1.3.2 Gold Nanoparticles

One of the most studied plasmonic nanomaterials is the gold nanoparticle. Extensive potential applications of gold nanoparticles (AuNPs) in bio labeling, catalysis, drug delivery, and therapies due to their novel optical and electrical properties have attracted many scholars' attention in recent years [54]. AuNPs because of their straightforward synthesis, functionalization and characterization, biocompatibility, and unique optical properties have been widely used in a variety of applications. AuNPs tend to penetrate to the tumor cells, and this will enable them to scatter the irradiated light, which will expose the location of the tumor [55]. The size and the shape of AuNPs influence their optical properties, so it is necessary to control these parameters during the synthesis.

1.3.2.1 Synthesis

The synthesis of gold nanoparticles can be done in both top-down or bottom-up approaches. Top-down approaches are possible, but they are much more challenging in comparison to bottom-up approaches. Laser ablation synthesis is one of the most common top-down approaches for the synthesis of gold nanoparticles [56]. In bottom-up approaches, however, the nanoparticles are synthesized from atomic building blocks; therefore, the control of the morphology, arrangement, and size of these nanoparticles is much easier. A variety of methods, including chemical, thermal, electrochemical, and sonochemical, have been introduced for the synthesis of AuNPs. The preparation of the AuNPs by chemical reduction method has two steps. First, the reduction of gold ions by the agents and second, adding the stabilizer agents to avoid the aggregation. One of the most famous methods for synthesis of the gold nanoparticle is adding chloroauric acid to the trisodium citrate aqueous solution, which is introduced by Turkevich in 1951. In this method, the gold ions will be reduced by the trisodium citrate (adding trisodium citrate to boiling gold solution). This method can produce gold nanospheres up to 20 nm. Citrate ions, which were reducing agents, can also act as a stabilizer. [57]. Frens improved the method of Turkevich in 1973. In this optimized method, gold nanoparticles have been produced in the range of 15-150 nm by controlling the ratio of precursors. For instance, using a high concentration of trisodium citrate will stabilize the solution faster; therefore, smaller gold nanoparticles can be achieved. However, using a low concentration of trisodium citrate will end up to bigger particles because the particles have more time to aggregate [57]. Some studies have reported that smaller particles and narrower size distribution can be obtained if the inverse sequence of adding precursors being followed (adding chloroauric acid to boiling trisodium citrate). This method is called reversed Turkevich [58]. Shulz et al. have reported by controlling the pH and adding EDTA more spherical nanoparticles can be produced.

1.3.2.1.1 Seed-mediated Growth Method The seeding growth method is relatively quick, easy, and cheap. In this method, first, small gold nanoparticles

are prepared then these small nanoparticles serve as the center of condensation for further growth of gold nanoparticles [59].

1.3.2.1.2 Non-aqueous Gold Colloidal Sols Aqueous sols in some cases are not desirable, therefore using organic solvents for the synthesis of gold nanoparticles is preferred. Sols obtained in organic solvents are usually unstable (they tend to aggregation and eventually from sediment) and they are highly polydisperse. For preventing aggregation, stabilizing agents such as PVP can be used to prepare gold nanoparticles. Brust-Schiffrin method is a conventional method to prepare gold nanoparticles in a two-phase system [54].

1.3.2.1.3 Ultrasound-assisted Synthesis of Gold Nanoparticles One of the methods, which is very useful in synthesizing the gold nanoparticles is the ultrasound-assisted synthesis of gold nanoparticles. In most of the synthesizing methods, for mixing the precursors and acceleration of reaction, the stirrer will be used; however, in the ultrasound-assisted method, the reaction will be done under ultrasonication. The particles produced by the ultrasound-assisted method are usually smaller, and highly monodisperse [60], [61], [62]. These benefits cannot be achieved by a conventional magnetic stirrer.

1.3.2.1.4 Conjugated Polymer-assisted Synthesis of Gold Nanoparticles By utilizing the redox chemistry of conjugated polymers for reducing the gold ions, gold nanoparticles can be directly synthesized through a conjugated polymer mediated technique. This method provides modulation of the morphology, structure, and the size of the gold nanoparticles and nanocomposite and enable the one-step synthesis of gold nanoparticles [63]. Only metal ions having a higher reduction potential than conjugated polymer can be spontaneously reduced to form zero-valent metal; otherwise, the additional electric field is necessary to force the reduction of these metal ions [64]. The reduction potential of Au^{3+}/Au is 1.52 V, which means its ions can be spontaneously reduced to zero-valent gold by the conjugated polymers whose reduction potential is less than

1.52 V.

1.4 Core-Shell Nanostructures

The idea of designing new structures, which can provide a combination of properties of different materials in one platform has become more realistic with recent developments in nanotechnology. A core-shell structure is a well-organized nanostructure consisting of two, three, or more types of distinct nanocomponents constructed based on cores (inner material) and shells (outer layer material). Many different properties can be obtained by wisely harmonizing the core(s) and the shell(s) of such materials.

1.4.1 Synthesis of Core-Shell Nanoparticles

The synthesis of core-shell nanoparticles (CSNs) can be done in both top-down or bottom-up approaches. Top-down approaches are possible, but they are much more complex in comparison to bottom-up approaches. Microfabrication techniques and mechanical stress are the most common top-down approaches for the synthesis of CSNs. In bottom-up approaches, however, the nanoparticles are synthesized from atomic building blocks; therefore, controlling the morphology, arrangement, and size of these nanoparticles is much simpler. The bottom-up synthesis of CSNs can be done in a stepwise or one-pot manner. Preventing lengthy separation and purification processes, and the simplicity of the whole reaction procedure are the main benefits of the one-pot synthesis over the stepwise synthesis. With this in mind, the one-pot synthesis of the CSNs would be much more profitable for scholars. The polymerization chemical reaction is one of the most common methods for synthesizing the CSNs. In this method, surface-active materials such as CuO and SiO_2 nanoparticles will be selected as the core. The polymerization will be initiated at the surface of these nanoparticles (cores), and ultimately, the polymeric shell will be formed over the core [65]. With this

method, a shell with a thickness of 2-10 nm can be obtained. The surface chemical reaction (surface deposition) is another method, which can be used for the synthesis of the CSNs. In this method, both the core and the shell are dispersed in an aqueous solution. Changing the pH of the solution and/or heating it can cause the formation of CSNs. TiO_2 @ SiO_2 is one of the CSNs that can be synthesized with this method [66]. The ultrasonic chemical method also can be used for the synthesis of the CSNs. In this method, the ultrasonic cavitation effect causes an increase in the chemical interaction between the surface of the core and the coating metrical and the CSNs can be formed more efficiently. Depositing gold on the SiO_2 nanoparticles is one of the examples of this method.

1.4.2 Properties

CSNs can possess completely new properties and/or synergistic properties among the cores and shells. Such features are one of the reasons that CSNs have received increased attention in recent years. Theoretically, CSNs can be designed almost in infinite ways. CSNs can be divided into four classes depending on the composition and the arrangement of the core and shell materials. Inorganic/inorganic, inorganic/organic, organic/inorganic, and organic/organic are typical types of CSNs [67], [68], [69]. Nanoparticles with metal (inorganic) cores and polymer (organic) shells are captivating materials. Both the properties of the core and the shell can be exploited in this kind of CSNs. These CSNs show a complex behavior while they are dispersed in a liquid. These complex behaviors are because of the interactions of core and shell, shell and shell (repulsion), and shell and continuous phase (dispersant). As a result of these behaviors, they can be called smart multi-functional materials. In these hybrid structures, the shell has pivotal functions. Prevent aggregation and protecting the core are the most crucial functions of the shell. Although it is mentioned that CSNs can be designed almost in infinite ways, practically, there are obstructions. Therefore, selecting the materials for the core and especially the shell(s) is not a straightforward task and requires further studies. For instance, the conjugated polymer-assisted synthesis of metal nanoparticles is only possible when the reduction potential difference

of the metal and the conjugated polymer is greater than zero. Structural and compositional parameters of CSNs can affect CSNs properties. Some of these parameters can be seen in Figure 1.5.

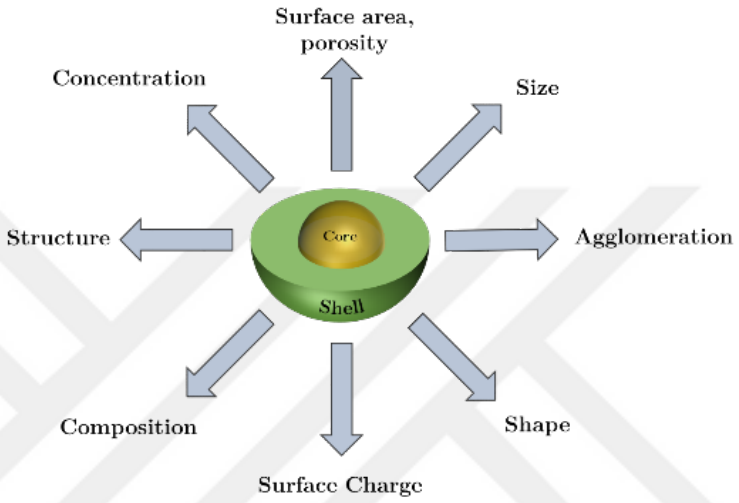


Figure 1.5: Effective parameters on the properties of CSNs.

1.4.3 Applications

CSNs can possess both the properties of the core and the shell in a synergistic manner; therefore, it is expected that they can be utilized in many applications. Drug delivery [70], hyperthermia [71], catalysis , sensing [72], energy storage [73], solar energy conversion [74], electromagnetic wave absorption [75], environmental [76], and combined photothermal and photodynamic therapy [77] are the some these applications.

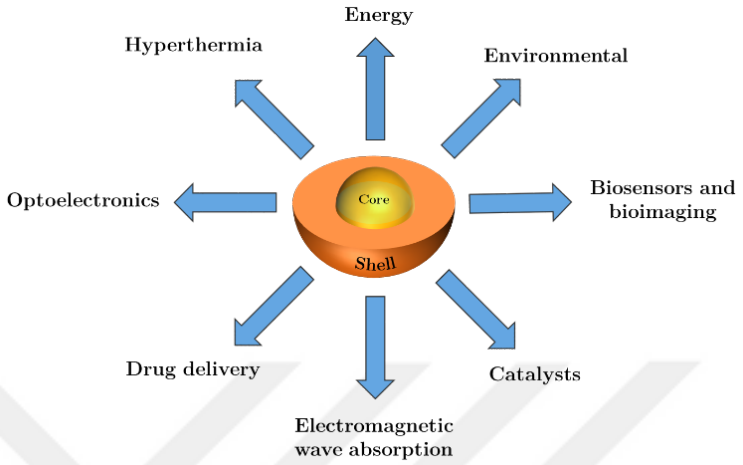


Figure 1.6: Applications of CSNs.

1.5 Colloidal Systems

A colloidal system implies a dispersed phase that has been disseminated all over a dispersing medium, which consists of two or more components mixed. Colloids can be a two-phase system or a single-phase (true solution) depending on the interaction of the dispersed phase particles and the continuous dispersant phase. The colloidal particles have a high interfacial area. It is also known that smaller particles possess a higher interfacial area. This causes the colloidal systems to have unique properties; therefore, for a better understanding of these properties, it is necessary to study colloids and surface chemistry together. According to the interaction of the dispersed phase particles and the continuous dispersant phase, colloids can be categorized as lyophobic or lyophilic. "Lyo" refers to the continuous dispersant phase, "phobic" means fearing, and "philic" loving. Lyophobic colloids maintain very high interfacial free energy; therefore, they are thermodynamically unstable and have a high tendency to aggregate so that they can reduce this interfacial free energy by forming a two-phase system. Lyophilic colloids, however, because of owning relatively stronger forces of interaction among dispersed phase particles and dispersion medium, are single-phase and their stability is much higher [78]. Some properties of colloids depend on the type of them. For instance, surface tension in a lyophilic colloid is less than its medium;

however, in lyophobic colloid is nearly the same as its medium. In lyophilic colloids, viscosity is usually higher than the medium. However, viscosity is almost the same as the medium in lyophobic colloids. When a colloid is called stable, it means that the repulsive forces among its particles are dominant. These repulsive forces can be steric or electrostatic. In steric repulsion, two particles preventing entwining due to the presence of active components on their surface. Electrostatic repulsion, however, is due to the presence of charges on the surface of the particles that prevent them from being close enough and start aggregating [79]. One of the best ways to roughly evaluate the stability of the colloidal solution is zeta potential calculation (measurement) [80]. The magnitude of repulsive forces is directly proportional to zeta potential absolute value. Negative values of zeta potential correspond to negatively charged particles, and positive values of zeta potential correspond to positively charged particles. Electrostatic repulsions are more effective than the steric repulsions. Usually, the absolute value of zeta potential of colloids, which their particles undergo electrostatic repulsions is higher than the particles undergo steric repulsions. Although it is mentioned in the literature that solutions owning zeta potential absolute value of 30 mV and higher are stable, some colloidal systems are stable even with zeta potential absolute values of less than 30 mV [81], [82], [83]. Hence, more studies are needed for the investigation of the stability of colloids. Adding an electrolyte to the lyophobic colloidal solutions can make them unstable. The phenomenon, which is called flocculation caused by forming aggregates and eventually sediment by the gravity [79]. All of the colloids cannot be fitted into one of these classifications, and some of them may have common characteristics with more than one of these categories; therefore, it can be said that whatever behavior like colloids can be called a colloid.

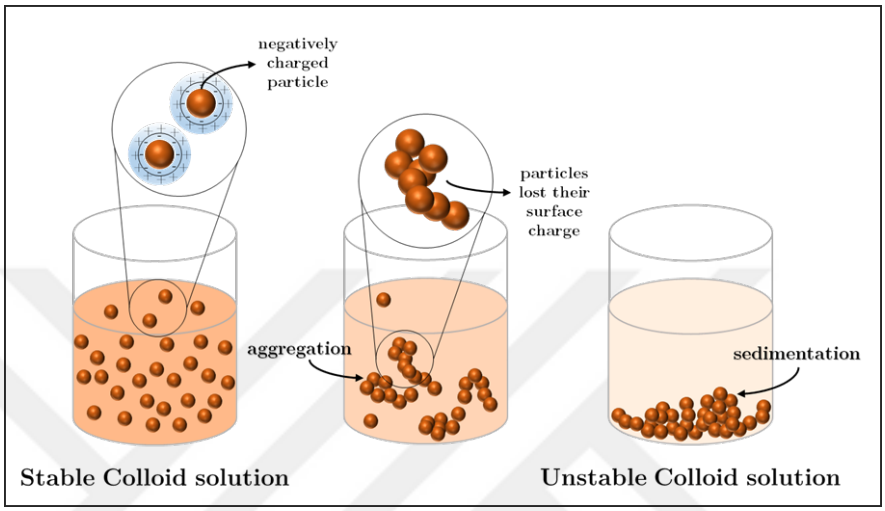


Figure 1.7: Electrostatic stabilization of colloids; adding strong electrolytes will cause the particles to lose their charges and this end up with aggregation and eventually sedimentation.

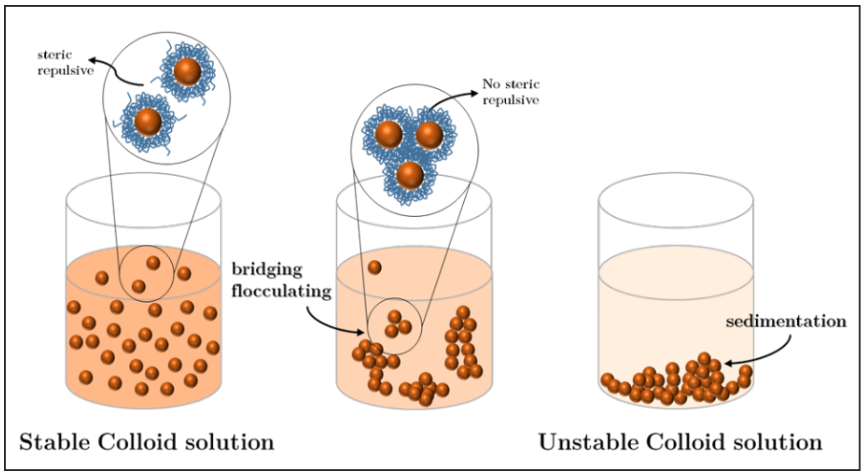


Figure 1.8: Steric stabilization of colloids; any modification usually ends up with aggregation and eventually sedimentation.

1.6 Photothermal Therapy

Using the heat for tumor therapy has been recorded in history. In 1700 BC, the glowing tip of a fire drill has been used for breast cancer therapy. With further developments in technology, the source of heating has been changed. Microwaves [84], ultrasound waves [85], [86], and radiofrequency [87], [88] are the modern sources for the heating. Heating a specific target tissue to a temperature in a range of 41-47 °C with a duration of ten minutes, can be defined as Hyperthermia [89]. Tumor cells, because of their poor blood support, cannot tolerate the heat as much as a normal tissue can do. With this in mind, heating the tumor in the mentioned range of temperature can damage the tumor. The drawback of hyperthermia with the conventional heat source is the permanent damage to the membrane of healthy cells as well as the tumor cells. By utilizing lasers as a heat source, scientists could tackle this problem partially with thermal damaging the tumor tissue in a controlled and confined way. Although the amount of damage is reduced substantially, still the biggest shortcoming of laser therapy is its selectivity. Both the normal and tumor cells will be affected in the path of laser beam [90]. Photothermal therapy (PTT), is another method for tumor therapy. In this method, the photothermal agents are utilized to achieve the heating of the local environment selectively [91], [92], [93], [94]. Gold nanoparticles, thanks to their strong absorption in the visible and NIR regions because of their surface plasmon resonance (SPR) oscillations, are widely being used in PTT. Since the gold nanoparticles are plasmonic, the treatment with gold nanoparticles is called plasmonic photothermal therapy (PPTT) or (PPT). Light-to-heat conversion efficiency and absorption cross-sections are two of the main properties of the PPTT agent, which should be considered for the initial design. Plasmonic metal nanoparticles such as gold and silver have a higher resistance to photobleaching, and their absorption cross-sections due to their SPR is around 5 to 6 times greater than non-plasmonic metal nanoparticles. With this in mind, the best candidates for PTT agent can be selected form these novel metals [95]. If cancer cells or bacteria (in the presence of gold nanoparticles) have been irradiated with a laser beam with a specific wavelength (usually at which SPR absorption occurs), the laser energy will be absorbed by gold nanoparticles in a few femtoseconds and

part of absorbed energy will be converted to heat, which can kill the cancer cells or bacteria. To discuss this in more detail, when a gold nanoparticle is exposed to the light, its electrons can be excited from the ground state to excited state by absorbing the light energy. These excited electrons will relax back to the ground state through nonradiative decay channels. This relaxation will increase the overall kinetic energy and ultimately overheat the local environment of the nanoparticle. Conversion of light energy to heat can be initiated with the collision of electron-electron and then followed by electron-phonon interactions will create a hotspot, which can increase the temperature by tens of degrees and eventually cause permanent damage to the wall or the DNA of the cell or the bacteria (Figure 1.9). The shape, size, and surface charge of the gold nanoparticles are crucial for PPTT. These properties are directly affecting the yield of the conversion of light energy to heat. Positively charged gold nanoparticles can effectively bind to the surface of the gram-negative bacteria, which are negatively charged.

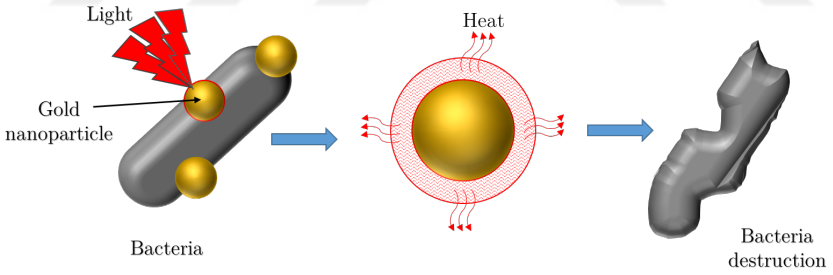


Figure 1.9: Scheme of PTT-Killing of E. coli bacteria; the generated heat will cause permanent damage to the bacteria wall.

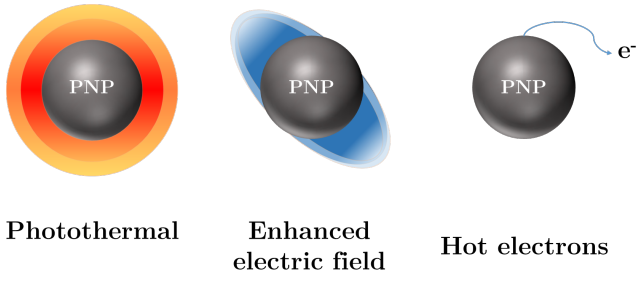


Figure 1.10: Dissipation of energy through plasmon-mediated transformation mechanisms caused by SPR.

1.7 Photodynamic Therapy

Photodynamic therapy (PDT), also known as photochemotherapy is a tumor therapy method. In this method, a chemical that is photosensitizer will be injected into the body and after a certain amount of time absorbs by the tumor cells [96], [97], [98]. A photosensitizer (PS) is a molecule that can be activated by light in order to generate reactive oxygen species (ROS), such as singlet oxygen ($^1O_2$). When a PS is stimulated with light, it will react with triplet oxygen ($^3O_2$) and generate the singlet oxygen ($^1O_2$) that is toxic to cells and tissues. The $^1O_2$ induces disarrangements in the cell wall and the DNA that will cause irreversible damages. An ideal PS should be a pure compound with a determined chemical structure and contain no heavy metals. It should maintain a high conversion yield of triplet oxygen ($^3O_2$) to singlet oxygen ($^1O_2$), low accumulation rate in the skin, and be inactive (harmless to the cells and the bacteria) in the dark. Porphyrin-based PSs are commonly used in clinical applications since their high capacity of singlet oxygen generation and biocompatibility. PSs can be also be used in water treatment [99]. Conjugated-polymer-based PSs are much more efficient in singlet oxygen generation in comparison to their small-molecule analogs. This can be caused by better intersystem crossing (ISC) which will end up with more singlet oxygen production [100], [101], [102], [103]. ISC is an isoenergetic radiationless transition between two electronic states having different multiplicities [104]. Conjugated polymers due to special electronic configuration own many energy levels in each energy band [105]. This special electronic configuration will enable the conjugated polymers to have less energy difference between S_1 and T_1 (ΔE), which is profitable for the singlet oxygen generation [106].

Cancer cells, in comparison with healthy cells, are more sensitive to hyperthermia therapy due to their high growth rate and fast metabolism. For having efficient PDT, the light should penetrate through tissue. The magnitude of wavelength and depth of penetration are directly proportional; therefore, scientists are looking for such PS having an appropriate light absorption at near-infrared region (NIR). Besides the penetration depth, it is better to choose less energetic lights to minimize the side effects associated with PDT. Hemoglobin in the blood

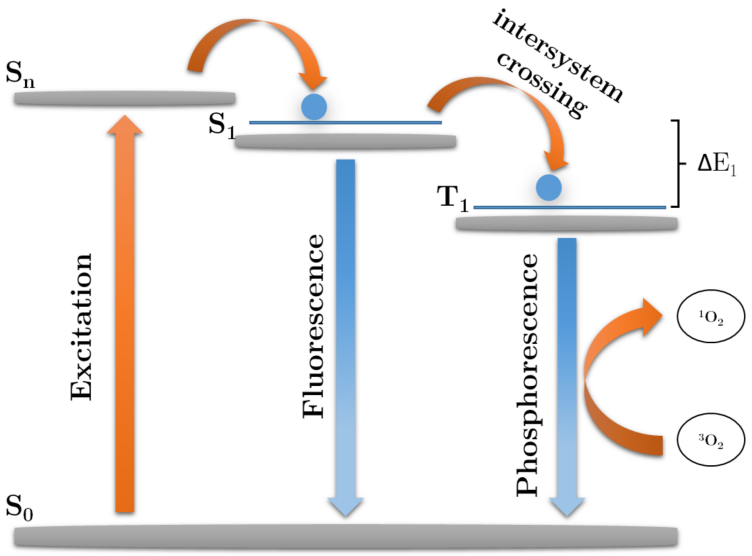


Figure 1.11: Jablonski diagram of small molecule PS for generation of $^1O_2$.

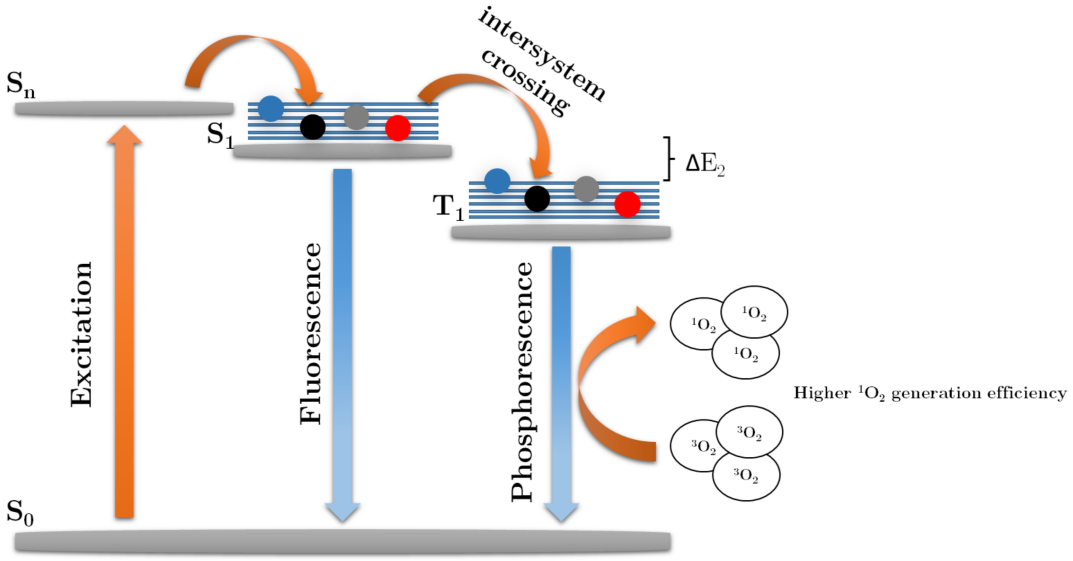


Figure 1.12: Jablonski diagram of conjugated polymer PS for generation of $^1O_2$; in comparison to small molecule PS, the $^1O_2$ generation efficiency of conjugated polymers PS is higher.

absorbs light up to the wavelengths of 600 nm. It means that the tissue should be illuminated by the wavelengths higher than 600 nm. At the wavelengths higher than 850-900 nm, the energy for the conversion of triplet oxygen to singlet oxygen cannot be granted; therefore, usually, the red light will be used in PDT [103].

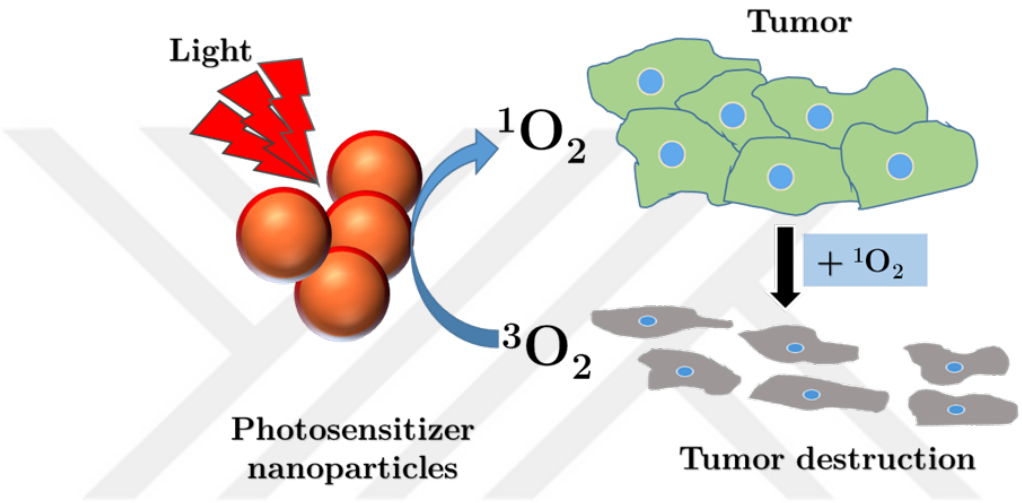


Figure 1.13: A simplified scheme of the mechanism of PDT-induced tumor destruction.; singlet oxygen generated with PS will cause substantial damage to the tumor cell wall.

The side effect of photodynamic therapy is negligible, and it does not create any scar. The biggest drawback of PDT is that the PS remains in the body and causes problems while the patient is exposed to the light.

1.7.1 Metal-Enhanced Singlet Oxygen Generation (ME^1O_2)

Multidrug resistance (MDR) in Escherichia coli (E. coli) has become a serious issue that is not only increasingly observed in humans but also is widespread in veterinary medicine worldwide. Therefore, new and effective alternatives to conventional antibiotics should be developed urgently. The resistance of E. coli to most or all of the antibiotics has been observed [107]. An emerging alternative approach for fighting pathogens such as PDT is an outgrowth of MDR. Since PDT does not possess any specific mechanism of action, regardless of the kind of bacterium and its level of resistance, it can be effective for most of the cases [108]. In some cases, however, the PDT agent is ineffective, and it needs further reinforcement. As mentioned earlier, the gold nanoparticles because of their high resistance to oxidation, possessing a well-known absorption peak, relatively easy synthesis, and almost no toxicity in the dark can be used for ME^1O_2. Considering this, improving the singlet oxygen generation efficiency will enhance the overall effectiveness of therapy. It can act as a reinforcement and compensate for the low killing efficiency provided by PS alone. Hybrid core-shell structures can be suitable for the ME^1O_2 and can provide higher singlet oxygen generation capacity for killing the bacteria [109]. In the presence of metallic nanoparticles such as gold and silver next to or inside the fluorophore, near-field interactions of fluorophores with metallic nanoparticles will occur. These interactions due to mirror dipole effect will enable both metal-enhanced fluorescence (MEF) [110] and metal-enhanced phosphorescence (MEP) [111], [112]. The higher singlet oxygen generation can be an outcome of an increase in the net system absorbance, enhancement in the triplet excited state yield of the sensitizer, and enhancement in the intersystem crossing. Figure 1.14 summarizes the previous statements and showing the Jablonski diagram of the photosensitizer and metal-enhanced singlet oxygen generation.

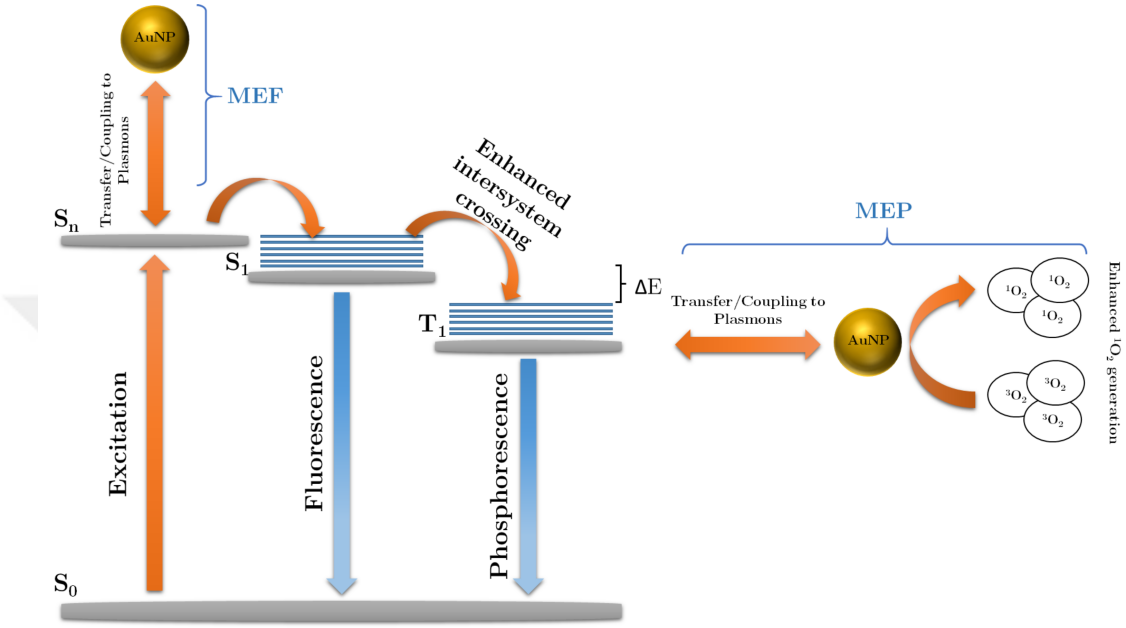


Figure 1.14: Modified Jablonski diagram of the photosensitizer and metal-enhanced singlet oxygen generation. Adapted with permission from [113].

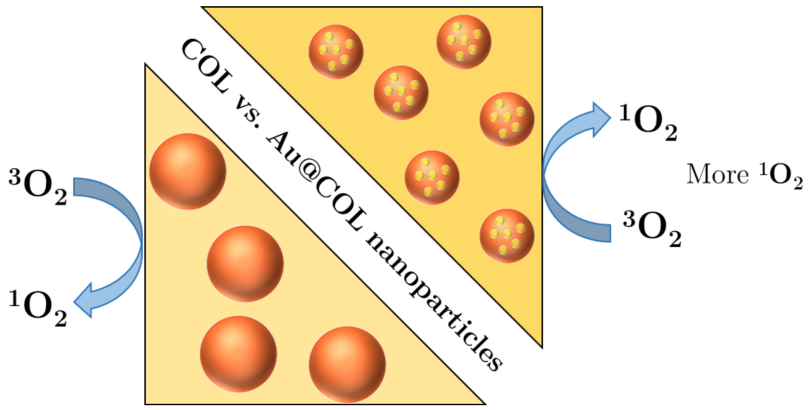


Figure 1.15: The expected performance of Au@COL and COL nanoparticles in the singlet oxygen generation. Au@COL nanoparticles, theoretically due to ME$^1O_2$ possess higher singlet oxygen generation capacity. Adapted with permission from [109].

1.8 E. coli bacteria

The oldest form of cellular life is bacteria. They can be classified into four classes according to their composition of the prokaryotic cell wall; gram-positive bacteria, gram-negative bacteria, bacteria with chemically different cell walls, and the bacteria with no cell wall. Gram-positive bacteria are such bacteria that take up the crystal violet stain, and their gram stain test is positive. Oppositely, gram-negative bacteria are such bacteria that retain the crystal violet color, and their gram stain test is negative. Bacillus subtilis and Escherichia coli are gram-positive and gram-negative bacteria, respectively. The gram-positive bacteria possess a single-layered cell wall, which is rigid due to the high amount of peptidoglycan. The gram-negative bacteria, however, own a bi-layered cell wall with less rigidity in comparison to gram-positive bacteria. The wall in gram-positive bacteria is porous and usually thicker than gram-negative bacteria. Gram-negative bacteria possess an outer membrane in their cell wall, which results in a low degree of permeability. This outer membrane is the main reason why the gram-negative bacteria resist many antibiotics. The same reason can also explain the higher prevalence of gram-negative infections. E. coli is a gram-negative bacterium with bacillus (rod-shaped) shape. It retains wavy and uneven walls and can be found in the gut of warm-blooded animals and humans. Most strains of E. coli are not harmful to the human body [114]. However, some strains, such as shigatoxigenic E. coli (STEC) and verotoxigenic E. coli (VTEC), can cause severe diseases. E. coli can easily be transmitted to humans, mainly by the consumption of contaminated foods (usually raw foods). During the last decades, a rising number of resistance genes have been discovered in E. coli isolates. These resistance genes are mostly acquired by horizontal gene transfer [115]. E. coli can act as a donor and recipient of resistance genes. High capacity to accumulate resistance genes, made the E. coli to be considered as a real public health concern. Multidrug resistance (MDR) in Escherichia coli (E. coli) has become a critical problem affecting both the animals and humans. As described earlier, E. coli, like other gram-negative bacteria, holds an outer membrane, which allows it to resist the ordinary antibacterial agents. PDT can be a solution, but it is reported that E. coli is unaffected by conventional PSs. Therefore, designing a new generation of

PS is needed for the PDT-killing of gram-negative bacteria. To execute antimicrobial PDT, the PS has to breach into the cell walls of the bacteria. Considering this, the membrane barriers in the gram-negative bacteria, limit the PS penetration, especially if the PS is anionic (negatively charged). Hence, PDT-killing of gram-negative bacteria is much harder than the gram-positive bacteria [117]. The gram-negative bacteria enjoy negatively-charged cell wall because of teichoic acid residues [116]. Therefore, cationic PS (positively charged) can be used to bind with the cell wall of gram-negative bacteria.

1.9 Previous Works with Red-Emitting Conjugated Oligomer

Balkan et al. have reported the one-pot synthesis of hybrid silver-conjugated oligomer nanoparticles. This work has proven that the spontaneous reduction of silver ions by COL is possible, and by modifying the reaction conditions, nanoparticles in different structures such as core-shell and raspberry and different sizes can be produced. For instance, different concentration ratios such as 1:1, 1:2, 1:4 (Ag:COL) have resulted in different optical and morphological properties. The resulting nanoparticles further characterized by UV-Vis and fluorescence spectroscopy, SEM, TEM, and DLS. These analyses showed that with increasing the concentration of silver ions, the fluorescence intensity quenches. The hydrodynamic diameter measured by DLS for the hybrid core-shell nanoparticles with the configuration of the silver core with conjugated oligomer shell (Ag@COL) was 50 nm. Possible applications for such hybrid core-shell nanoparticles are claimed to be in photocatalysis, plasmonic sensing, and theranostics [118]. Successfully spontaneous reduction of silver ions indicates the reduction potential of COL is at least 0.8 V. It means that it can theoretically reduce the metal ions possessing the reduction potential of 0.8 V and higher. With this in mind, the spontaneous reduction of gold ions would be possible with this oligomer since the reduction potential of Au^{3+}/Au is 1.52 V. Considering this, the one-pot synthesis of hybrid gold-conjugated oligomer nanoparticles would be possible.

Chapter 2

Introduction to measurement techniques

2.1 Dynamic Light Scattering and Zeta Potential

Dynamic light scattering (DLS), also known as photon correlation spectroscopy and sometimes as quasi-elastic light scattering is a non-invasive technique for measuring the size of particles and molecules in suspensions.

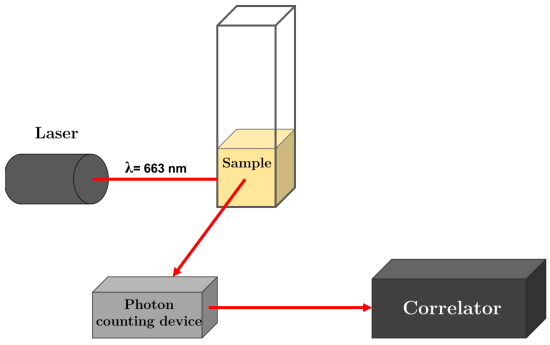


Figure 2.1: Scheme of working principle of DLS.

DLS measures the speed at which these particles undergo this Brownian motion. Brownian motion is a random movement of particles and molecules. The origin of this random movement is that particles are constantly being bombarded by the solvent molecules that surround them. Small particles diffuse rapidly while large particles diffuse slowly. The velocity of this Brownian motion is called the translational diffusion coefficient (D). The size of particles can be calculated by the Stokes-Einstein equation:

$$d(H) = \frac{kT}{3\pi\mu D} \tag{2.1}$$

where,
$d(H)$ = hydrodynamic diameter
D = translational diffusion coefficient
k = Boltzmann's constant
T = absolute temperature
μ = viscosity

Hydrodynamic size is the diameter of a hard-sphere that diffuses at the same speed as the particle and molecule being measured. It depends on various parameters, such as ionic strength, surface structure, and shape of particles. Ionic strength will be effective on Debye length. Debye length is the thickness of the electrical double layer formed by the cloud of ions that exists around the surface of the particle and the molecule. Debye length is inversely proportional to ionic strength, so as the ionic strength goes higher, it compresses the Debye length; therefore, the recorded size from DLS for any particle suspended in a salt solution will be smaller than the same particle in deionized water. The surface structure can influence hydrodynamic diameter because it affects the diffusion speed. If the shape of particles is irregular, they undergo a random diffusion. During a measurement, the instrument will measure different diffusion coefficients depending on the orientation of the particles; therefore, the reported average size might not be reliable. Small changes in the length of rod-shaped particles will change the rod's diameter; however, because it hardly affects the diffusion speed, DLS cannot detect the size change. The sample holder can be a disposable plastic

(polystyrene), glass, or quartz cuvette. The disposable holder cannot be used for most organic solvents such as THF. For organic solvents, usually, the glass cuvette is being used. In the reported results, the intercept in the correlation function diagram is the signal to noise ratio. The values higher than 0.9 determine a high-quality signal. The amount of time it takes the correlation function to begin the decay indicates the mean size of particles. Faster decays, usually mean smaller particles. The slope of the correlation function shows the polydispersity of the sample. The higher slope (more vertical) means less polydispersity in the sample. The baseline exposes whether there are aggregations (big particles) or not. The flat and smooth baseline shows there are no big particles. For analyzing the correlation function, two different analyses are performed: First, the cumulants analysis and second, the distribution analysis. Cumulants analysis provides mean size (z-average), and polydispersity index (PDI) and distribution analysis provides the distribution of sizes. For cumulants analysis, only the dispersant refractive index and viscosity are required. If the z-average is much higher than the reported size distributions in the results, big particles are present in the sample. The z-average diameter and PDI are tightly bonded in the way that reported z-average diameter of particles with PDI of 0.08 or less are more likely to be the same as average sizes reported by TEM images. However, in the PDI of 0.2 or higher, the z-average diameter is greater than the reported size in distribution analysis. Number, volume, and intensity distributions can be found in the software report. Each of them can be useful for specific purposes. As it is mentioned, the larger particles scatter the light more than the smaller particles so, in intensity distribution, the reported sizes are based on the particles, which scattered the light more efficiently. So the reported sizes in intensity distribution are larger than average sizes reported by TEM. The intensity distribution diagram is the best source to investigate the presence of large particles inside the sample. In volume distribution, the reported size is smaller than the intensity distribution reported size, and it is based on the volume of the particles. In number distribution, the number of particles having the same size determines the reported size. The reported size by number distribution is smaller than the sizes reported by intensity distribution and volume distribution, and it is much closer to reported size by TEM. Although reporting the number distribution is

usually preferred, but it is more accurate to report the sizes by all three distribution in the articles. Zeta potential is the overall charge a particle acquired in a particular medium. Zeta potential depends on both the chemistry of the surface of particles and the dispersant. Zeta potential can be calculated with the help of electrophoretic mobility. The sample is inserted into a capillary cell with electrodes. As the instrument applies the voltage across two electrodes since the distance of two electrodes is known, the electric field strength can be calculated by instrument. The charged particles can gain velocity, and the instrument can measure the velocity of these particles by Doppler shifts. Small changes in pH and concentration of ions can lead to dramatic changes in the zeta potential value. For electrostatically stabilized dispersions, the higher the value of zeta potential, the more stable the dispersion is likely to be. The effect of the pH on the value of the zeta potential can determine the isoelectric point location and how much acidic or basic the surface of particles are. If a charged particle has been dropped into the water, oppositely charged ions (counterion) will associate right around that particle and create a layer called the stern layer. Right after the stern layer and up to a particular distance mixture of counterions and coions form another layer named the diffuse layer. These two layers together are called the electrical double layer. Zeta potential indicates a potential that belongs to an arbitrary plane named slipping plane, which is located close to the stern layer (Figure 2.2). Electrical double layer width is reversely proportional to ionic strength. The valency of the ions will also effect double layer thickness. For instance, Al^{3+} will shrink the electrical double layer more effectively in comparison with Na^{+}. Zeta potential does not indicate the actual charge of the surface of particles, so it determines how much effective is the surface charge. The zeta potential can be calculated by Hemry's function. In this function, depending on the polarity of the medium Huckel (non-polar) and Smoluchowski (polar) approximation can be used. The stability of colloidal systems is determined by the balance of repulsive and attractive forces. If there is mutual repulsion, then the dispersion will resist flocculation. Oppositely, if there is not repulsion, then flocculation or coagulation will eventually take place.

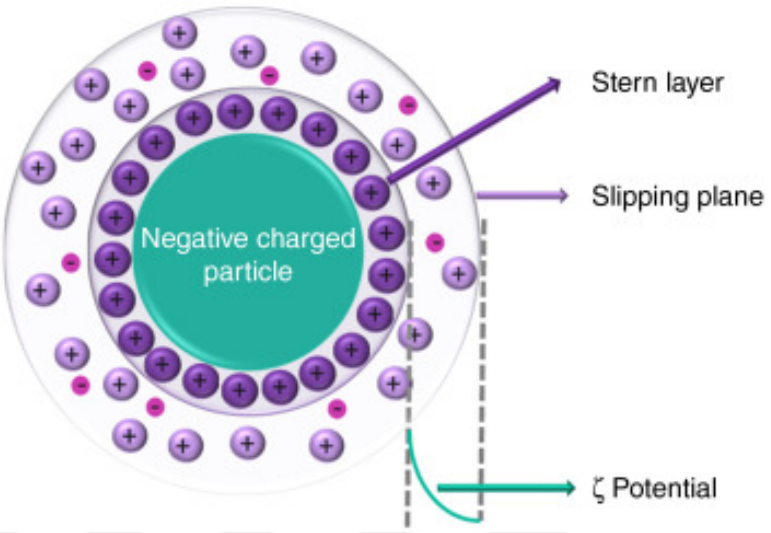


Figure 2.2: The Illustration of zeta potential. Reprinted with permission from [119].

2.2 Ultraviolet-visible Spectroscopy

In ultraviolet-visible spectroscopy (UV–Vis or UV/Vis) the electromagnetic wave with the wavelength in the range of 200 nm to 800 nm will be emitted to the cuvette (usually a pathlength of 1 cm) containing the sample. The interaction of the light and the chemicals in the sample will result in absorption in the spectrum. The wavelength and the magnitude of the absorption (location and intensity of peak) can reveal information about the chemicals or changes in the structure. In the UV-Vis spectrum, the Y-axis is optical density (OD), which is dimensionless, and the X-axis is the wavelength in nanometer. The instrument can calculate the optical density, by the Lambert-Beer law, which is more commonly known as Beer's law.

$$OD = \varepsilon cl \tag{2.2}$$

where,

ε is molar attenuation coefficient of the material in $L.mol^{-1}.cm^{-1}$

c is the molar concentration of those species in $L.mol^{-1}$ and

l is the pathlength in cm.

As it is demonstrated in Equation 2.2, the OD value is directly proportional to the concentration of the sample. This direct relation is only valid when there is no aggregation in the sample. UV–Vis can be used for comparing two different compounds. During the comparison, usually, the shifts in position and intensity of peaks are considered. In the bathochromic shift, the absorption peak moves towards the longer wavelength or lower energies. This can be due to the formation of different auxochromes (a group of atoms attached to a chromophore), adding conjugation and solvent effect. When a solute is dissolved in a polar solvent if the excited state of solute is more polar in comparison to its ground state, the polar solvent tries to stabilize the excited state more than the ground state. In this case, the gap between the excited state and the ground state (bandgap) decreases, which means less energy is required for the excitation, and there will be a redshift in the absorption spectrum. The hypsochromic shift, also known as the blueshift is the absorption peak move towards the shorter wavelengths or, the higher energies. It may be caused by the removal of conjugation or by the change in the polarity of the solvent. On the contrary of redshift, when a solute is dissolved in a polar solvent if the excited state of solute is less polar in comparison to its ground state, the polar solvent tries to stabilize the ground state more that excited state. In this case, the gap between excited and the ground states (bandgap) increases, which means higher energy is required for the excitation, and there will be a blueshift in the absorption spectrum. In addition to these two shifts, there are other possibilities related to the change in the intensity of peaks. The hyperchromic effect is an effect due to which the intensity of absorption maximum increases. This can be caused by changes in the absorption coefficient (chemical structure) or concentration. An excellent example of this effect is the conversion of the pyridine to 2-methylpyridine in the same concentration, which causes a redshift from 257 nm to 262 nm and an increase in the absorption coefficient from 2,750 to 3,560 $L.mol^{-1}.cm^{-1}$. Another effect is hypochromic. Hypochromic is an effect due to which the intensity of an absorption maximum peak decreases. The best example of this effect is the conversion of the biphenyl to 2-methyl biphenyl in the same concentration which causes a blueshift from 250 nm to 237 nm and a decrease in the absorption coefficient from 19,000 to 10,500 $L.mol^{-1}.cm^{-1}$. In the case of gold nanoparticles, UV-Vis spectroscopy can

reveal information about the size and shape of the nanoparticles. For instance, the gold nanospheres with the size of 20 nm, possess an absorption peak at the wavelength of 520 nm. In this case, they absorb the blue and green portions of the light and transmit the orange and red portions of light, so the color of 20 nm gold nanospheres is red. Urchin-shaped gold nanoparticles, however, own an absorption peak at the wavelength of 680 nm that makes the color of its solution blue. With the help of UV-Vis spectroscopy, it can also be said whether the gold solution is aggregated or not. The redshift in the UV-Vis spectrum of gold nanoparticles that results in a bluer solution color, which usually can be interpreted as an increase in the size of particles and/or the aggregation. The reason for that can be explained by the shift in the surface plasmon resonance to a lower frequency. When gold nanoparticles get closer, the conduction electrons of particles become delocalized, and the probability of being shared with other gold nanoparticles conduction electrons gets higher. Hence, less energy is needed to excite the electrons from the ground state to an excited state. Aggregation can also make the peak broaden or form a secondary peak at longer wavelengths.

2.3 X-ray Diffraction

XRD also knowns as X-ray diffraction is a quick analytical technique that can be used for phase identification of crystalline materials. It also can offer information on unit cell dimensions. X-ray diffraction is based on the interaction of the incident rays with crystalline material. If this interaction satisfies Bragg's law, it will produce constructive interference.

$$n\lambda = 2dsin\theta \tag{2.3}$$

The Bragg's law relates the lattice spacing in a crystalline sample and diffraction angle to the wavelength of incident electromagnetic radiation. The d-spacings provide some information about the identity of the materials. Compering these d-spacings with standard reference patterns will reveal the identity since some minerals have sets of exclusive d-spacings. X-ray diffraction is broadly has been

used in the characterization of crystalline materials, purity of the sample, monitoring the evolution in the sample during the reaction, and quantitative analysis. It can also be used for crystallites (grain) size measurements using the Scherrer equation. In polymer science, the degree of crystallinity is a crucial parameter. Investigating the crystallinity of the polymer will help to utilize them for certain applications. Higher crystallinity makes polymers to be more robust, harder, translucent, and opaque to some extent. The percentage of crystallization can be calculated using the following equation.

$$\%Xc = \frac{Ac}{Ac + Aa} * 100 \tag{2.4}$$

In this equation, A_c is the area under the peaks until the baseline (crystalline area), and A_a is the area under the baseline (amorphous area). These areas are depicted in Figure 2.3.

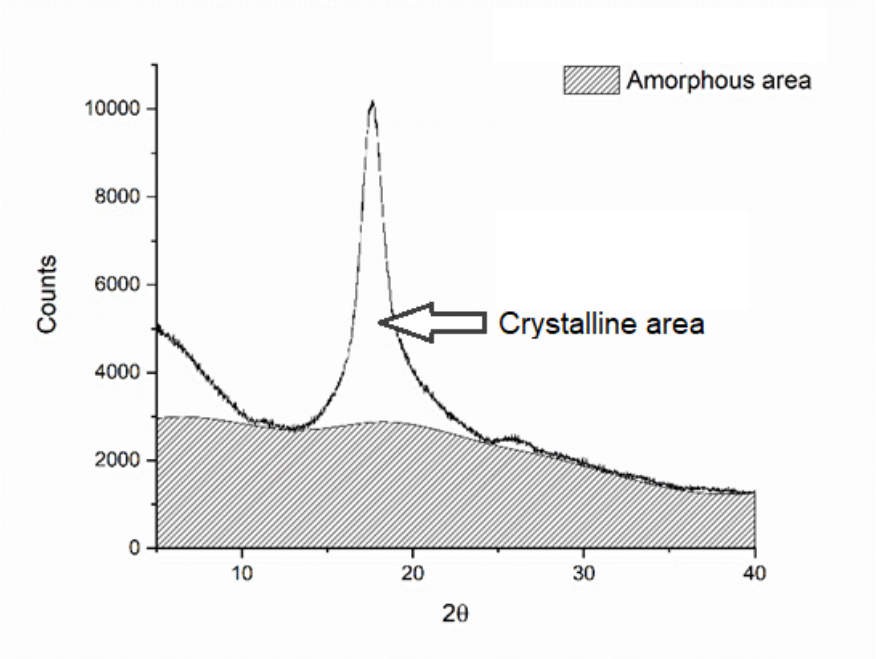


Figure 2.3: XRD pattern of a semi-crystalline material.

2.4 Fluorescence Spectroscopy

Fluorescence is one type of luminescence. Luminescence broadly can be defined as light emission from any substance. This emission occurs in a longer wavelength (or lower energy) than the excitation wavelength. There are several types of luminescence. Photoluminescence occurs when light energy or photons stimulate the emission of photons. Chemiluminescence is observed when chemical energy stimulates the emission of a photon, and this includes bioluminescence, which is seen in fireflies and many forms of sea life. Electroluminescence happens when electrical energy or strong electric field stimulates the emission of a photon. In fluorescence spectroscopy, a specific wavelength of electromagnetic wave (light) usually in the range of 200 nm to 800 nm is passed through a solution containing fluorophores. The solution will emit the light towards a filter and then to the detector for counting. This process will provide an emission spectrum that its X-axis is wavelength in nm, and its Y-axis is intensity. A fluorophore can be excited by light at a specific wavelength at which or where the strongest absorption occurs. This specific wavelength can be easily obtained by UV-Vis spectroscopy. The fluorophore can be excited by the light with wavelengths close to the excitation maxima wavelength, but the intensity of emission will be much lower. The emission spectrum can be useful to identify, quantify, and investigate the chemical activities of the fluorophore. The Intensity emission spectrum is usually directly proportional to the concentration of the fluorophores. In some cases, this direct proportion is just valid up to a certain concentration. For instance, in some of the porphyrin-based molecules adding more of the fluorophore will decrease the overall intensity. Short-range interactions between the fluorophores may cause this self-quenching. It can be said that for some of the luminescence materials, there is a global maximum (extremum) in the intensity-concentration diagram. It means that with trying different concentrations, the highest possible intensity for such materials can be measured. In other words, they exhibit non-monotonic behavior. Finding this trend is not an easy task since a wide range of concentrations should be measured. Physical properties including temperature, concentration, colloidal stability (aggregation), solvent polarity, pH of the solution, and presence of plasmonic metals in the solution shape the wavelength and intensity of the emission

maxima. The presence of plasmonic metal nanoparticles near the fluorophore can modify the optical properties of the fluorophore. They can either enhance or quench the intensity of the emission. Significant fluorescence quenching was reported by Dulkeith et al. for Lissamine dye molecules in the presence of 2 nm gold nanoparticles. On the contrary, Nakamura and Hayashi's research proved that in the presence of 100 nm gold nanoparticles, there is a considerable enhancement in the fluorescence properties of the Rose Bengal fluorophore. Changing the solvent of the solution usually causes a shift in the wavelength and/or intensity of emission. The shift in emission maxima can be indicative of highly polar excited state formation, which experiences relaxation by the solvent. The magnitude of the shift will vary concerning the solvent polarity. Another factor that can cause a shift in the wavelength and/or intensity of emission is the local dielectric environment of fluorophore. In water dispersed florescence oligomers, nonradiative interaction between oligomer molecules in close vicinity can cause a shift in the wavelength of emission. The difference between the wavelength of the absorption and emission peaks is called the Stokes shift. The energy loss of the fluorophore through molecular vibrations during its excitation state causes the Stokes shift. The surrounding solvent molecules will heat up by this energy, which has been dissipated as the heat by the fluorophore. The electronic structure of the fluorophore is the main factor for the magnitude of the Stokes shift. Other factors such as complex formation, solvent effects, excited-state reactions can also affect the magnitude of the Stokes shift.

2.5 Time-resolved Fluorescence Lifetime

Fluorescence lifetime is the time that a molecule spends in the excited state. TCSPC or time-correlated single-photon counting, also known as time-resolved fluorescence lifetime (TRF) or time-domain fluorescence lifetime is the most common technique for measuring the fluorescence lifetime. In TCSPC, the lifetime will be measured as decay, and the resulting decays will be fitted to a rate (or multiple rates) equation(s). When a population of molecules is excited with the flash, after a while, the population randomly decays back down to the ground state, which leads to emit one photon from each molecule. The instrument can measure the intensity at each time point over the fluorescence emission of this population and draw a decay of intensity versus time. The lifetime (tau) can be estimated as the (1/e) value for a single exponential decay. Depending on the source, the detector, and the timing electronics, the lifetimes in the range of 5 picoseconds to seconds can be recorded. Fluorescence lifetimes can also be indicators of the local environment. For instance, a molecular rotor is used to monitor the viscosity of a sol-gel process by fluorescence lifetime. The more viscous the sol-gel, the longer the lifetime of the fluorescence probe [120]. Another optical property of the material is the quantum yield (QY). In simple words, quantum yield is the probability of getting emission from a fluorophore which has been excited with proper wavelength. In other words, quantum yield is the radiative rate over the total rate (radiative rate + nonradiative rate). The calculated QY is usually reported as a percentage. An ideal fluorophor possesses the QY of 1 or 100%.

2.6 X-ray Photoelectron Spectroscopy

X-ray photoelectron spectroscopy (XPS) is a technique for analyzing the structure of atoms and getting information about electron structure as well as ionization energies. With this technique, the chemical composition of various materials can be obtained. It shows which chemical elements are present at the surface, such as carbon and oxygen. The chemical bond nature, which exists between these elements, will be reported as well. The first advantage of XPS is that it is a non-destructive method, as well as a surface-sensitive method. It has some disadvantages. Being expensive and the requirement of a high vacuum for the operation are two main downsides. It is a relatively slow measurement, so it might need a whole night to provide results. It only detects elements with an atomic number of three and above. The working principle of the XPS is based on the phenomenon, which is known as the photoelectric effect. When an atom absorbs an x-ray with enough energy, an inertial electron will be ejected. The energy of an x-ray with a particular wavelength is known. The ejected photoelectrons have kinetic energy that can be calculated to be equal to the energy of the incident x-ray minus the binding energy and the work function of the element. The work function is defined as the minimum energy needed to remove an electron from a solid to the vacuum instantly outside the solid surface. Auger electrons, which are also generated during the measurement, can be utilized for further characterization. When an atom is excited by X-ray radiation, the inner shell electrons of the atom can be excited and leave the atom while they leave a hole in the shell. Outer shell electrons will undergo a relaxation process to fill the hole. The excess energy is emitted as an upper shell electron moves to the vacant spot. This excess energy can then be transferred to another outer shell electron causing it to leave the atom. These electrons are called the Auger electrons. The sampling depth for XPS is in the range of 3-10 nm. The outcome spectrum of the XPS possessing intensity at Y-axis and binding energy in (eV) at the X-axis. Usually, the X-axis is reversed, so the right of the spectrum is the starting point (lower eV). The intensity can be used in quantitative analysis and comparative diagrams. Chemical shifts (shifts in the binding energies) are very important. The peak positions can determine the purity of the sample, oxidation

states, and chemical composition. As mentioned, the ejected electrons are the main source for XPS measurement. For each element, the shell and the subshell, which the electrons come from, can be different. For instance, 1s is selected as the primary XPS region for carbon element, while for sulfur element, 2p is selected. Although the 2p is selected as the primary XPS region for sulfur, it can also be measured with 2s. The reason that the primary XPS region for sulfur is 2p can be referred to as the quality of signal in that particular binding energy belonging to 2p and less probability of overlapping with other peaks belonging to other species. Palladium can also be measured in both 3p and 3d, but in 3p measurement, the peak for palladium overlaps with oxygen 1s peak, so palladium 3d is preferred. In measurements, p, d, and f orbitals, possessing a doublet peak while the s orbital possesses a singular peak. The doublet peak is formed due to the spin-orbital splitting, whose explanation is beyond the scope of this work. Spin-orbital splitting and peak area ratios will be beneficial for element identifications. Differences among the electronegativity of elements affect the peak positions in the way that more electronegative species such as oxygen can shift the peaks to higher binding energies while more electropositive species such as metals shift the peaks to lower binding energies. In simple words, when the atom loses one or more valence electrons, the binding energy of the atom will increase, while when the atom gains electrons, the binding energy of the atom will decrease. The reason is that the atoms with higher positive oxidation states possess extra coulombic interaction between the photoemitted electron and the ion core. For instance, the elemental tin (Sn^0) possesses a doublet peak at $3d_{5/2}$ = 484.65 eV and $3d_{3/2}$ = 493.15 eV while the Tin (IV) oxide (SnO_2) owns a doublet peak at $3d_{5/2}$ = 486.5 eV and $3d_{3/2}$ = 495 eV. The shift with the magnitude of 1.85 eV is an indication of the change in the environment of elemental tin. The magnitude and direction of the shift can reveal some information. In this case, oxygen molecules (more electronegative species) have reacted with the elemental tin and shifted the doublet peaks to higher binding energies since the energy required for ejecting electrons from metal oxides is higher than elemental metal. Another parameter that should be considered in the interpretation of data is the degeneracy. The total angular momentum quantum number (j) is equal to absolute value of angular quantum number (l) $\pm$ spin projection quantum number

(s), j = | l ± s |. Degeneracy is an integer and is equal to 2j+1. The ratio of degeneracies for the same orbital corresponds to the ratio of the intensity of its doublet peak. Table 2.1 shows the concept of degeneracy.

Table 2.1: Electron levels and corresponded degeneracy.

Orbital	l	j	Degeneracy	Electron Level
1s	0	1/2	1	1s
2s	0	1/2	1	1s
2p	1	1/2	2	$2p_{1/2}$
2p	1	3/2	4	$2p_{3/2}$
3d	2	3/2	4	$3d_{3/2}$
3d	2	5/2	6	$3d_{5/2}$
4f	3	5/2	6	$4f_{5/2}$
4f	3	7/2	8	$4f_{7/2}$

2.7 Transmission Electron Microscopy

Transmission Electron Microscope (TEM), uses a high-energy electron beam, which is focused on a thin sample at a thickness of about 200 nm. As the electrons penetrate the sample, they can undergo elastic or inelastic scattering. Both the scattered and the transmitted electrons can be exploited for imaging. In TEM, the imaging can be done in different modes. In bright field imaging, the transmitted electrons are collected, and the scattered electrons are blocked; therefore, the areas that the electron beam can pass through readily are brighter while the other spots that the electrons are scattered are darker. On the contrary, in the dark field imaging, the transmitted electrons are excluded while the scattered electrons are collected. In this mode, more scattering ends up with brighter spots in the image. Atoms with a higher atomic number (Z) can scatter the electrons more efficiently; therefore, the bright filed mode, the darker spots belong to the heavier species. In contrast, in dark field mode, the brighter spots belong to the heavier species. Crystalline materials can also scatter the electrons in a better way; hence, they will be brighter in the dark field mode. These unique traits will be helpful for investigation of the possible crystal lattice defects and determining the crystal structure. Scanning transmission electron microscopy (STEM) as its name represents is similar to very similar to TEM. In TEM, the parallel electrons beams are perpendicularly focused on the sample, while in STEM, the beam is converged into a focal point, which enables it to scan the sample. The most widespread detector for the STEM is high-angle annular dark-field (HAADF). HAADF is very helpful when an enhanced contrast in needed [121]. It is more sensitive to a lower atomic number and tiny nanoparticles; hence, in some cases, which TEM images do not provide enough contrast, HAADF can be a good option. This feature of HAADF can be used when two species are not distinguishable in the dark field mode. For instance, Pt and MnS cannot be distinguished by TEM while they will be in HAADF [122]. Since each species has different d-spacings, it is possible to determine crystal identity with the help of TEM, which helps to distinguish different species. SnO_2 vs Pt. With a special setup, it is possible to measure some of the transmitted beam characteristics at different locations of the sample. For example, once can measure the electron energy loss (EELS). To

this aim, a magnetic prism is used to detect the beam more or less depending on the energy. The more the beam loses energy, the more it is deflected. The measure of this deflection allows for characterizing different pairs of the sample. This technique can be used for visualizing and identifying the chemical nature of molecules in ultra-thin samples. Another mode of TEM is diffraction mode. In this imaging mode, the image is the result of Bragg scattering when the electron beam passes through the crystalline sample. The results depending on the degree of crystallinity can be an array of dots in single-crystal materials or a set of diffuse rings in polycrystalline materials.

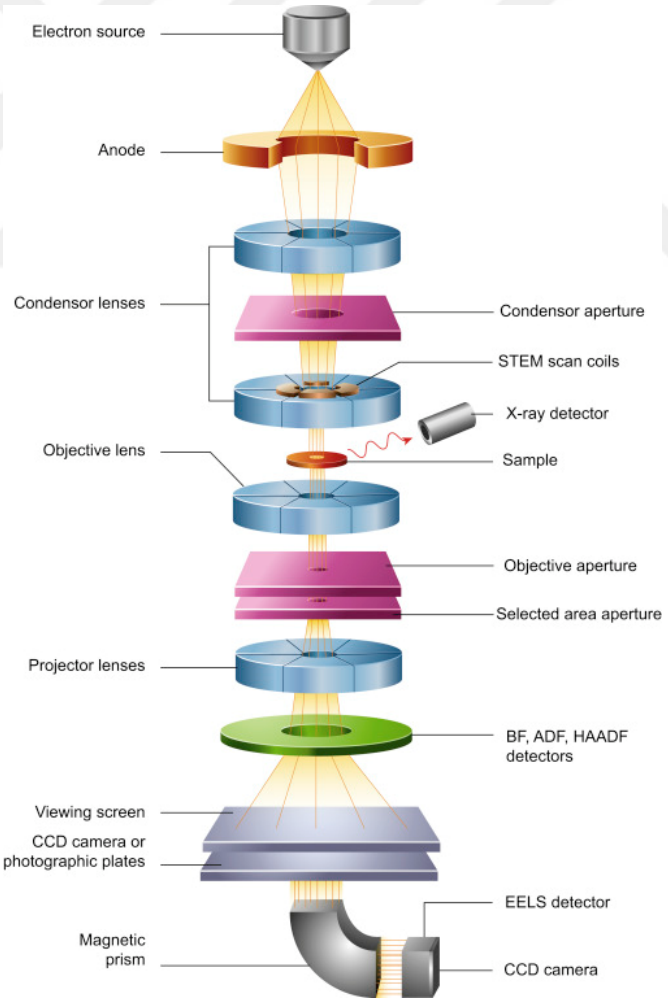


Figure 2.4: Schematic diagram of the main components of TEM. Reprinted with permission from [123].

2.8 Scanning Electron Microscopy

Scanning Electron Microscope (SEM) is an electron microscope that can image the surface of the sample via a focused beam of electrons. When a beam of electron interacts with the atoms of the surface of the sample, signals, which contain information about the morphology and topology of the surface as well as the composition of the surface, will be produced. The computer can render these signals and translate them into a graphical image. The secondary electrons are usually the primary source of the signals; however, backscattered electrons can also be detected in advanced detectors. The resolution of backscattered electrons' image is less than the secondary electrons' image; therefore, most of the SEM devices come with the SE detector. Moreover, the electron beam can also ionize the atoms and make them emit X-rays. The energy of the rays depends on the elementary composition of the sample. These signals can be combined with secondary electrons signals and reveal the chemical nature and the spatial variation of the material. As we deal with electrons in SEM, for better images in terms of resolution and details, the sample should be electrically conductive. If the sample is not conductive, the image is usually blurry, and the surface of the sample will be burnt. For preventing blurry images, it is recommended to coat the nonconductive samples with a very thin layer of Au/Pd alloy (around 2-5 nm). This will help the electrons not to accumulate on the surface of the sample. Using thick layer coating will change the surface morphology, and some features such as porosity cannot be exposed in that case. Finding the optimum coating thickness is one of the most critical steps in sample preparation. Another crucial step in sample preparation is to make sure the sample is dried. SEM needs a vacuum condition for operation. Existing a small portion of water inside the chamber will change the sample morphology. In biological specimens, using a high vacuum setup is not possible since most biological specimens contain water [124]. To tackle this problem, using Environmental SEM (ESEM), which utilizes a low vacuum setup with a relative humidity of 90% in the chamber, is a solution. Low resolution and blurry images in high magnification are drawbacks of ESEM. Another solution for imaging biological using SEM is drying the samples with the CPD method. In this method, the samples will be dried out theoretically

without any change in their surface. In the normal drying process, the tension between liquid water and vapor water interface will damage the surface of the biological object while in CPD method, the interface will not be formed, and liquid water can be converted to water vapor without any tension at the interface so the surface of the sample will be untouched. Conventional SEMs can resolve images up to 50 nm while the least generation SEMs can go further up to 10 nm.

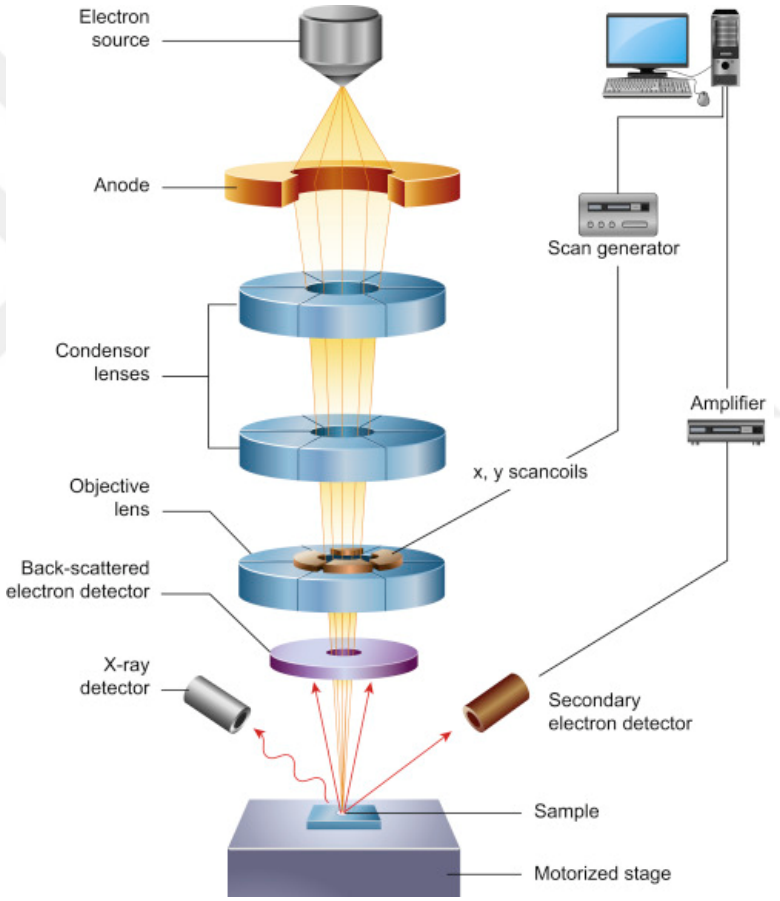


Figure 2.5: Schematic diagram of the main components of SEM. Reprinted with permission from [123].

2.9 Critical Point Dryer

Every substance has a critical temperature and critical pressure. When a substance is subjected to temperature and pressure that both exceed these critical values, it enters what is called a supercritical state. Any pure substance can exist in three phases: solid, liquid, and gas. These phases can be shown by using a diagram called the phase diagram. A typical phase diagram possesses pressure on the Y-axis and temperature on the X-axis (P-T diagram). This graph shows the location of the different phases of a pure substance in relation to pressure and temperature. The three phases are separated from each other by three separation lines: the sublimation line, which divides the solid and the vapor phases (the sublimation line ends at the triple point, which is the point where all three phases coexist), the melting line, which divides the solid and the liquid phases, and the vaporization line that splits the liquid and the gaseous phases (the vaporization line finishes at the critical point). The temperature on the critical point is called the critical temperature and usually is designated by symbol T_c. The corresponding pressure for the critical point is called the critical pressure, which has the symbol P_c. Each element or compound has its P_c and T_c. Exceeding the pressure and temperature from the critical temperature and critical pressure will end up entering the supercritical state. In this state, the interface between the liquid phase and the gas phase disappears the surface tension between this interface goes to zero, and continuity of state will occur. This phenomenon can be utilized in Critical Point Drying (CPD). The zero surface tension can be exploited to dry out the biological specimens without any substantial damage to their morphology and ultrastructure. Biological samples contain water; therefore, as described earlier, they should be heretofore dried out to be imaged by the SEM. Considering this, drying the biological samples with conventional methods cannot be practical since these methods will damage the surface of the biological specimens. Hence, the way of removing water plays a pivotal role in imaging the biological samples. As reported in the literature [ref need], the critical point for the water is at +374 °C and 3212 psi. Drying the sample in this temperature will damage the sample, and it may undergo a thermal degradation and or surface deformation. Therefore, water is not a good transitional medium for CPD.

Carbon dioxide (CO_2), which owns a critical point at 31 °C and 1072 psi can be a proper transitional medium for CPD since it requires a relatively much lower temperature to be supercritical. The only drawback for CO_2 is its miscibility in the water. CO_2 is not miscible in the water. Therefore, the involvement of third medium so-called intermediate fluid such as ethanol or acetone is necessary.

2.10 Microplate reader

For PDT-killing of gram-negative bacteria, first, the Minimum Inhibitory Concentration (MIC) should be determined. MIC is the lowest concentration of the antibacterial agent required to inhibit the growth of microorganisms and usually is reported in the unit of μg/ml. Minimum Bactericidal Concentration (MBC), however, is the lowest concentration of the antimicrobial agent required to kill microorganisms, which is also reported as μg/ml. The most common way to determine the MIC of species is the Broth microdilution method. In a concise explanation, in this method, the antibacterial agent will be added to a set of plates containing bacteria. The concentration of the agent will increase stepwise for each plate. Parallel to experiment sets there will be the control sets, which are set of plates contain only the bacteria. In control sets, the bacteria are unrestricted to reproduce, but in experiment sets, which contain a mixture of the bacteria and the antibacterial agent, the inhibition of the bacteria reproduction is expected. Due to this inhibition, the optical properties of the experiment sets and the control sets are different. The microplate reader can determine the relative number of bacteria for each plate. In this instrument, depending on the selected mode, different optical properties of the solution can be obtained. In absorption mode, the light with the wavelength of 600 nm will be emitted the plate. As the light passes through the plate, some portion of it will be absorbed by the bacteria and remaining will be transmitted to the detector. The resulted optical density at 600 nm (OD_{600}) is directly proportional to the numbers of the bacteria inside the plate. Therefore, any decrease in the OD_{600} value means a lower rate of reproduction, which ends up in the less number of bacteria in that particular plate. The microplate reader will provide data, which can be drawn

as a diagram possessing OD_{600} at its Y-axis and agent concentration in (μg/ml) at its X-axis. A typical MIC diagram looks like an exponential decay with the maximum of (0,1 1.2). When there is a negligible change in the magnitude of OD_{600} with respect to a step-change in the concentration, it is hard to find the MIC, since it is relatively behaving like a constant function. In this case, the MIC will be the concentration, corresponding to the point, which the exponential decay starts to behave like a constant function (reaches a plateau). Therefore, MIC will not always be the concentration of the agent, corresponded to the lowest OD_{600} value.

2.11 Fourier-transform Infrared Spectroscopy

Fourier-transform infrared spectroscopy (FT-IR) is a technique used to determine the functional groups or bonds present in the structure. In this technique, the inferred laser will be emitted to the sample, which can be solid, liquid, and gas. The interaction of the incident infrared with the molecules of the sample will cause absorption, which can be detected by the instrument detector. The intensity and position (wavenumber) of absorption will reveal the information about the structure of the sample and possible functional groups. Different groups of atoms vibrate at different frequencies. These vibrations can be in-plane or out-of-plane and can be categorized into six major groups: symmetrical stretching, asymmetric stretching, scissoring, rocking, wagging, and twisting. The infrared itself can be categorized into three main regions according to its frequency (wavenumber):

1. The higher energy near-IR 14,000-4,000 cm^{-1} (0.8-2.5 μm wavelength)
2. The mid-infrared, 4,000-400 cm^{-1} (2.5-25 μm wavelength)
3. The far-infrared 400-10 cm^{-1} (25-1,000 μm wavelength)

which, according to their energy, can be used in different conditions. The mid-infrared region has been exploited for IR spectroscopy since most of the functional

group vibrations frequency is in this frequency of this region. The material can be Raman or IR active depending on their stretch. If the stretch is asymmetric, the material is IR active so it can be concluded that polar molecules are always IR active since they possess a net dipole. Sample preparation for FT-IR is an exhausting task, but with the help of Attenuated Total Reflectance (ATR), there is (almost) no sample preparation required. ATR is a technique used in combination with FT-IR spectroscopy, which allows samples to be studied in all states without any preparation. When an infrared light shines to the ATR crystal, it sets up an evanescent wave. The evanescent wave leaves the crystal and penetrates the sample in certain depth, which is called penetration depth. The wavenumber of emitted light effects the DP (depth of penetration). As the magnitude of wavenumber increases, the light energy will go higher, and DP will drop; It can be concluded that using a shorter wavelength will end up with a shallower penetration. The other factor, which affects the DP is the incident angle. The most crucial factor is the refractive index of the crystal we use for the ATR. ATR manufacturing companies are using Diamond or Germanium crystals. The refractive index of diamond is approximately 2.4, which enables the beam to penetrate around 2 microns, and Germanium refractive index is around 4.0, and its DP is around 0.7 micron.

Chapter 3

Experimental

3.1 Materials

All reagents and solvents used in the syntheses were of analytical grade and were purchased from Sigma-Aldrich. All reactions were performed under air and solvents were dried and distilled before use, unless otherwise stated. Milli-Q water (18.2 MΩ·cm @ 25 °C) was used in synthesizing nanoparticles.

3.2 Synthesis

3.2.1 Synthesis of Red-Emitting Oligomer

Red-emitting conjugated oligomer (COL), namely, 3,3',3",3"'-[(1E,1'E)-2,1,3-benzothiadiazole-4,7-diylbis (ethene-2,1-diyl)]-bis (9H-fluorene-9,9,2-triyl) -tetrakis (N,N-dimethylpropan-1-amine), has been synthesized and reported in our group's previous works [125]. A very brief synthesis pathway has been depicted in Figure 3.1.

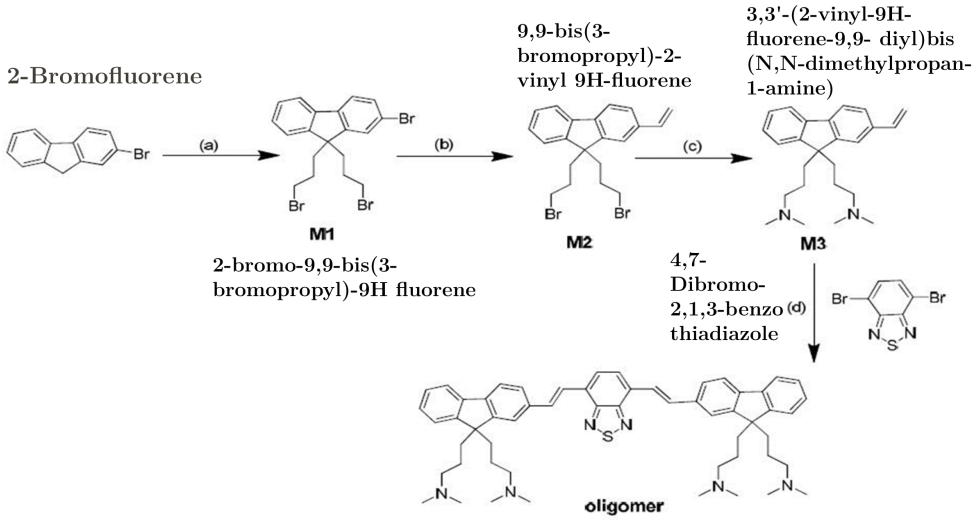


Figure 3.1: A simplified scheme of the synthesis of the red-emitting oligomer.

The synthesis of this oligomer consists of four main steps:

3.2.1.1 Synthesis of 2-Bromo-9, 9-bis(3-bromopropyl)-9H-fluorene, M1.

In the first step, 50% w/w KOH solution is prepared in a two-neck round-bottom flask. Then 263 mg (0.851 mmol) of TBAB and 41.145 g (20.19 mmol) of 1,3-dibromopropane were added to the solution while stirring then 2.5 g (10.19 mmol) of 2-bromofluorene was added to the flask. The solution was heated for 45 minutes at the temperature of 80 °C. The solution, first, extracted with water and DCM. The collected organic layer then again extracted with two molar solution of hydrochloric, water, and eventually brine solution. After the removal of excess 1,3-dibromopropane from the solution with vacuum distillation, it was further purified with the silica column using cyclohexane as the eluent solvent. The yield for this step was 64%.

3.2.1.2 Synthesis of 9,9-Bis(3-bromopropyl)-2-vinyl-9H-fluorene, M2.

The second step (b) is the synthesis of the 9,9-Bis(3-bromopropyl)-2-vinyl-9H-fluorene, M2. In this step, 700 mg (1.43 mmol) of M1 and 4.54 mg (0.022 mmol) of 2,6-ditertiary butyl phenol were poured in a two-neck round-bottom flask then dried under vacuum for half an hour. Then, 20ml of toluene and 544 mg (1.72 mmol) tributyl vinyl tin were added to the flask while stirring. For removing the oxygen, the reaction mixture, then, subjected to three freeze-pump-thaw cycles. Under nitrogen flow, 15.4 mg (0.022 mmol) of $PdCl_2(PPh_3)_2$ was added to reaction mixture. Then the mixture refluxed for one day while stirring @ 100 °C. Next, the solvent has been removed with a rotary evaporator. The product was further purified with the silica column using cyclohexane/ DCM (9:1) as the eluent solvent. The yield for this step was 90%.

3.2.1.3 Synthesis of 3,3'-(2-vinyl-9H-fluorene-9,9- diyl)bis (N,N-dimethylpropan-1-amine), M3.

The third step (c) is the synthesis of the 3,3'-(2-vinyl-9H-fluorene-9,9-diyl)bis(N,N-dimethylpropan-1-amine), M3. In this step, 550 mg (1.27 mmol) of M2 was dissolved in THF in a two-necked flask. The solution was cooled down to -78 °C and next, 8 ml of 2 molar dimethylamine in THF was added. The mixture left to warm up at room temperature and kept one day while stirring. Next, the solvent has been removed with a rotary evaporator. The product further was purified with the silica column using cyclohexane/ DCM (7:3) as the eluent solvent. The yield for this step was 91%.

3.2.1.4 Synthesis of 3,3',3",3"'-[(1E,1'E)-2,1,3 benzothiadiazole-4,7-diylbis (ethene-2,1-diyl)]-bis(9H-fluorene-9,9,2-triyl) tetrakis (N,N-dimethylpropan-1-amine), the conjugated oligomer.

The fourth and last step (d) is the synthesis of the 3,3',3",3"'-[(1E,1'E)-2,1,3 benzothiadiazole-4,7-diylbis (ethene-2,1-diyl)]-bis(9H-fluorene-9,9,2-triyl) tetrakis (N,N-dimethylpropan-1-amine), the oligomer. In this step, 788 mg (2.25mmol) of M3 and 322 mg (1.1 mmol) of 4,7-Dibromo2,1,3-benzothiadiazole was placed in a two-neck round-bottom flask. Then the mixture was dried out under vacuum for half an hour. 10 ml of DMF was added to the mixture and stirred. Then 756 mg (5.5 mmol) of K_2CO_3 was dissolved in the 10 ml of water and the resulting solution, was added to the mixture. Next, for removing the oxygen, the mixture was subjected to three freeze-thaw-pump cycles. Afterward, 26 mg (0.023 mmol) of $Pd(PPh_3)_4$ and 25.3 mg (0.113 mmol) $Pd(OAc)_2$ was added to the mixture. The resulting mixture was heated up to 90 °C while stirring under nitrogen flow. Next, the solvent has been removed with a rotary evaporator. Then crude product extracted by chloroform. After evaporation of the solvent, again it was washed with cyclohexane. The product was further purified by dissolving it in THF and then precipitation it into cold MeOH. The yield for this step was 80%. The synthesized oligomer is brownish sticky solid, which can be dissolved into THF, $CHCl_3$, and DMF while it is not soluble in water.

3.2.2 Dispersion of Conjugated Oligomer Nanoparticles in Water

Conjugated oligomer (COL) dissolved in THF was dispersed in water as follows: 45 mg (0.053 mmol) of conjugated oligomer was dissolved in 10 ml of THF. Then, 1 ml of resulting solution was injected dropwise into 15 mL of Milli-Q water in a 100-mL beaker while sonicating. The mixture was sonicated for 40 minutes at 35 °C. As a final point, the solution was exposed to air for gradual removal of THF for one day.

3.2.3 Synthesis of Hybrid Core-Shell Nanoparticles

One-pot synthesis of gold-conjugated oligomer core-shell nanoparticles (Au@COL) have been done at different concentrations ratios such as 1:2, 1:4, and 1:8. COL dissolved in THF were dispersed in water containing gold ions as follows:

COL stock solution: 5.0 mg (0.0058 mmol) of conjugated oligomer dissolved in 5 ml of THF. Resulting solution possessed a concentration of 1.12 mM.

Gold stock solution: 27.0 mg (0.088 mmol) of gold (III) chloride dissolved in 20 ml of Milli-Q water. Resulting solution possessed a concentration of 4.4 mM.

(a) Au:COL (1:2): 267 μl (1.18 μmol) of gold stock solution was injected to 15 mL of Milli-Q water in a 100-mL beaker. Then 2 ml (2.35 μmol) of COL stock solution was injected dropwise into mixture while sonicating. The mixture was sonicated for 40 minutes at 35 °C. As a final point, the solution was exposed to air for gradual removal of THF for one day.

(b) Au:COL (1:4): 133 μl (0.6 μmol) of gold stock solution was injected to 15 mL of Milli-Q water in a 100-mL beaker. Then 2 ml (2.35 μmol) of COL stock solution was injected dropwise into mixture while sonicating. The mixture was sonicated for 40 minutes at 35 °C. As a final point, the solution was exposed to air for gradual removal of THF for one day.

(c) Au:COL (1:8): 67 μl (0.3 μmol) of gold stock solution was injected to 15 mL of Milli-Q water in a 100-mL beaker. Then 2 ml (2.35 μmol) of COL stock solution was injected dropwise into mixture while sonicating. The mixture was sonicated for 40 minutes at 35 °C. As a final point, the solution was exposed to air for gradual removal of THF for one day.

Although the experiments have been done in three different concentrations, the best result in terms of stability, and effectiveness were obtained in 1:2 (Au:COL) ratio; therefore, core-shell nanoparticles with the concentration ratio of 1:2 were used for further studies and the results of the 1:4 and 1:8 ratios are not covered in results and discussion section. Considering this, the term Au@COL in the whole thesis refers to the 1:2 mole ratio (Au:COL).

3.3 Antibacterial Assays

3.3.1 Preparation of the Bacterial Solution and Minimum Inhibitory Concentration (MIC Assay)

The broth microdilution method was utilized for determining the MIC values of the Au@COL and the COL nanoparticles [126]. For growing bacterial, a single colony of E. coli on a solid Luria-Bertani (LB) agar plate was transferred to 5.0 mL of liquid LB culture medium and incubated at 37 °C in 200 rpm for 15 hours. The bacterial mixture then diluted 2-fold with pure LB. For starting the measurements, the initial OD_{600} value was adjusted to 1.0 and 25 different concentrations consist of 0.30, 0.65, 0.95, 1.25, 1.60, 1.90, 2.20, 2.50, 2.80, 3.10, 3.40, 3.70, 3.95, 4.25, 4.55, 4.80, 5.10, 5.35, 5.65, 5.90, 6.20, 6.45, 6.70, 6.85, and 7.20 μg/ml of both structures was prepared. A 100 μl of the bacterial mixture was injected to 1.5 ml Eppendorf tubes and then 10 μl from each prepared concentrations was added to the mixture. An equal volume of 10 mM PBS was used for the control experiment. Au@COL, COL and blank containing tubes were irradiated with white light for 30 seconds with the flux of 22 mW/cm^2. The same experiment has been repeated in the dark to study the dark toxicity of Au@COL and COL nanoparticles. Next, the Eppendorf tubes incubate for 16 hours at 37 °C and 200 rpm. Finally, the incubated mixtures relocated from Eppendorf tubes to 96-Well microplates to conduct the measurement with a microplate reader.

3.3.2 Biocidal activities of COL and Au@COL nanoparticles toward E. Coli

The E. coli suspension (2 ml, $OD_{600} = 1.0$) was diluted 5 times with PBS. After determining the MIC values, which in the case of Au@COL nanoparticles is 4.0 μM and in the case of COL nanoparticles is 5.5 μM, in separate measurements, was added to 2 ml of diluted bacteria suspension. The resulting mixture was incubated at 37 °C for 15 minutes in 200 rpm. After incubation, the mixture was irradiated for 30 seconds with white light with the flux of 22 mW/cm^2. A 50 μl of the diluted bacterial suspension (10^4 fold in PBS) was distributed on the solid LB agar plate. After 14 hours incubation at 37 °C, the number of formed colonies were counted. The same procedure has been followed for the COL incubated with E. coli in the dark and control experiments in both dark and light exposure.

3.3.3 Preparing the bacteria for imaging

The E. coli Suspensions (100 μl, $OD_{600} = 1.0$) in 1 ml of PBS were incubated for two different measurements with 5.5 μm of COL for first measurement and 4.0 μm of Au@COL nanoparticles for second measurement at 37 °C for 15 minutes in 200 rpm. The incubated mixture was irradiated by white light with the flux of 22 mW/cm^2 for 30 seconds. For the control experiment, an equal volume of PBS was used. For removing organic contamination, silicon wafers (1 cm * 1 cm) were incubated for half an hour with isopropanol. After incubation, they were dried with nitrogen gas and then located to six well-plate. Four samples were prepared for imaging; first, the irradiated mixture of bacteria and Au@COL nanoparticles, second, the non-irradiated mixture of bacteria and Au@COL nanoparticles, third, the irradiated suspension of bacteria (light-control), and fourth, the non-irradiated suspension of bacteria (dark-control). The same preparation procedure has followed for COL nanoparticles. For fixing the bacteria on the silicon wafers, 2.5% glutaraldehyde solution in PBS was used (12 h at 4 °C). Next, the wafers were washed with PBS, water, 25% (v/v) ethanol, 50% (v/v) ethanol, 75% (v/v) ethanol, and finally with pure ethanol. As a final point, the wafers were dried by

a critical point dryer. (CPD) [101].

3.3.4 Zeta Potential Measurements

E. coli suspensions (100 μl, $OD_{600} = 0.95$) in 500 μl of PBS were incubated with 4.0 μg/ml of Au@COL nanoparticles and 5.5 μg/ml of COL nanoparticles for 30 seconds at 37 °C in 200 rpm. After treatment with light (for one minute with the flux of 22 mW/cm^2), the centrifuge at 7,000 rpm for two minutes was used for harvesting the bacteria. Then the bacteria were washed with water and resuspended in 1.0 ml of water. The resulting mixtures of bacteria were kept on the ice for zeta potential measurements.

3.3.5 ROS Measurements

2.4 mg (0.005 mmol) of dichlorofluorescein diacetate (DCFH-DA) was dissolved in 5 ml of ethanol. Next, 500 μl of the resulting solution was added to 2 ml of 0.01 N NaOH and left at room temperature and in the dark for 30 minutes. Then, 10 ml of 25 mM sodium phosphate buffer (pH 7.4) were added to the mixture. The resulting mixture (DCFH) with a concentration of 40 μM was kept on ice and dark until further use. For blank measurements, 500 μl of DCFH was diluted with 1 mL of water and was added to standard fluorescence cuvette. The sample was excited at 488 nm and emission data was collected from 498 nm to 800 nm with a slit width of 5 nm for both excitation and emission. The PL intensity of diluted DCFH solution without PS was measured (blank 0 min) then the solution was irradiated under white light (1 mW/cm^2) for one minute (blank 1 min). The light irradiation repeated four times (each time one minute) and the PL intensity of fluorophore recorded. For Au@COL and COL nanoparticles measurements, 100 μl of 3.1 μM of each structure in separate measurements was added to 500 μl of DCFH then the mixture was diluted with 1 mL of water and was added to standard fluorescence cuvette for measurements. The same procedure as blank measurements were followed for Au@COL and COL nanoparticles [127], [128].

3.4 Instrumentation

3.4.1 Transmission Electron Microscopy

Morphological characterization and Energy-Dispersive X-Ray Spectroscopy for determining compositions of the nanocomposite have been performed by using FEI Tecnai G2 F30 transmission electron microscope. Bright-field and HR (with the beam voltage of 300 keV) and STEM modes were utilized. All the samples were drop-casted on the TEM support grid and dried out at room temperature.

3.4.2 Scanning Electron Microscopy

3.4.2.1 Imaging the nanoparticles

Morphological characterizations of the nanoparticles were obtained via Quanta 200 FEG instrument at different beam voltages and spot sizes depending on the optimum condition. All the samples were drop-casted on the p-type silicon wafer (single side polished) and not coated with Au/Pd alloy unless otherwise stated.

3.4.2.2 Imaging the bacteria

The bacteria were fixed on the silicon wafers with the help of a 2.5% glutaraldehyde solution in PBS. The dried samples were coated with 5 nm of Au/Pd alloy.

3.4.3 UV-Vis Absorbance Spectroscopy

In this work, all the measurements have been done using Cary 300 UV-Vis spectrophotometer equipped with Xenon flash lamp. Standard UV Quartz Cuvettes (with two matt sides) with a 1 cm pathlength was selected for measurements. All

the measurements have been carried out in the range of 300 to 800 nm.

3.4.4 Fluorescence Spectroscopy

Varian Cary Eclipse fluorescence spectrophotometer was used to record the PL spectra of the nanoparticles and the ROS measurements. The measurements have been done in room temperature using the standard quartz fluorescence cuvette with a 1 cm pathlength.

3.4.5 Time-Resolved Fluorescence Spectroscopy

TRF measurements were carried out using a Pico Quant FluoTime 200 spectrometer. A picosecond pulsed laser at a wavelength of 375 nm has been used for the excitation of nanoparticles. The resulting fluorescence decay curves were recorded by a TimeHarp time-correlated single-photon counting unit then fitted to multiexponential decays with the help of the FluoFit software.

3.4.6 X-Ray Powder Diffraction

Wide Angle Pananalytical X'PertPro with CuKα X-Ray Radiation ($\lambda = 0.15418$ nm) was selected for XRD measurements. The patterns were recorded in the 2θ diffraction with angles in the range of 20 to 80 with 0.02 step size.

3.4.7 X-Ray Photoelectron Spectroscopy

For XPS analysis, the Thermo Scientific K-Alpha X-Ray Photoelectron Spectrometer system has been used. The device was equipped with AlKα micro-focused monochromator source. All the measurements have been done while the flood gun was on and 200 eV and 30 eV were selected for survey and resolution scans

respectively. All the samples were drop-casted on the p-type silicon wafer (single side polished), dried out in room temperature, etched for 60 seconds with the voltage of 500 V and low current for avoiding surface contamination and oxidation. All the peaks have been fitted with the help of the Thermo Scientific's Avantage software.

3.4.8 Dynamic Light Scattering and Zeta Potential

For this work, the size and zeta potential of the nanoparticles were measured by the Malvern Zetasizer Nano ZS with 663 nm laser. All the measurements were performed at room temperature. For DLS measurements, standard fluorescence cuvette was used for both the aqueous and non-aqueous samples. For zeta potential measurements, folded capillary zeta cell has been used. For the sake of accuracy, the measurements were repeated at least three times for each set, and the average of results are reported.

3.4.9 Critical Point Dryer

All the drying has been done with Autosamdri-815B, Series B, using CO_2 at 7.39 MPa and 31 °C for drying and ethanol as an intermediate fluid.

3.4.10 Microplate reader

SpectraMax M5 multi-detection microplate reader system has been used for measurement of optical density at 600 nm (OD_{600}) of bacteria. All the measurements have been conducted at room temperature.

3.4.11 FT-IR Spectroscopy

Bruker Alpha-II Platinum ATR FT-IR spectrometer was used for determining the chemical functional groups of the materials. The spectra were obtained in the range of 400-4,000 cm^{-1} with resolution of 2 cm^{-1}.

Chapter 4

Results and Discussion

This chapter contains four sections. In the first section, the aim of the study has been discussed. In the second section, the characterization of core-shell nanoparticles and conjugated oligomer nanoparticles are covered. In the third section, the mechanism of formation of core-shell nanoparticles and conjugated oligomer nanoparticles are discussed, and the characterization data are interpreted as well as the stability of the Au@COL nanoparticles colloid over time has been investigated. Finally, in the fourth section, the studies on the PDT-killing of E. coli bacteria with the COL nanoparticles have been compared with enhanced PDT-killing of E. coli bacteria with the Au@COL nanoparticles.

4.1 Aim of the Study

The aim of this study is the one-pot synthesis and characterization of a hybrid core-shell nanostructure material that can be used in antibacterial photodynamic therapy. In order to fulfill this objective, this hybrid core-shell nanostructure material should satisfy some criteria; the criteria such as biocompatibility for both the shell and core, plasmonic core for ME^1O_2 and a shell, which can generate singlet oxygen efficiently for PDT while it is under light irradiation. Considering this, the red-emitting conjugated oligomer, which is a suitable PS and can spontaneously reduce metal ions due to the presence of amine functional group in the chain of the oligomer, is synthesized. In this core-shell structure, the oligomer will act as a shell and would form a stable colloid in water and protect the core (metal nanoparticles) from aggregations. The gold is selected for the core since its salt is soluble in water, the oligomer can spontaneously reduce it and more importantly, its nanoparticles are plasmonic and show resistance to oxidation, and they can be utilized in ME^1O_2 and photocatalysis. E. coli bacteria are selected for performing antibacterial photodynamic therapy since as mentioned earlier, MDR in E. coli has become a worrying issue, and conventional antibiotics are not able to kill the E. coli efficiently. Besides, the surface charge of E. coli is negative, which enables them to bind with hybrid core-shell nanoparticles and increase the efficiency of PDT-killing of E. coli.

Furthermore, the hybrid core-shell nanoparticles were characterized by TEM, SEM, Zetasizer, UV-Vis absorbance and fluorescence spectroscopies, TRF, XPS, FT-IR, and XRD techniques. Finally, the COL and Au@COL nanoparticles were used to kill the E. coli bacteria.

4.2 Characterization

4.2.1 Characterization of Red-Emitting Conjugated Oligomer

The red-emitting conjugated oligomer is fully characterized and reported in our previous works [118], [125].

4.2.1.1 FT-IR Spectroscopy

For acquiring data, two drops of COL dissolved in the THF was added on top of the ATR crystal. The FT-IR spectrum of COL shows sharp peaks at 740, 834, 967, 1,040, 1,152, 1,231, 1,450, 1,675, 2,750, 2,940 cm^{-1} as expected (Figure 4.1).

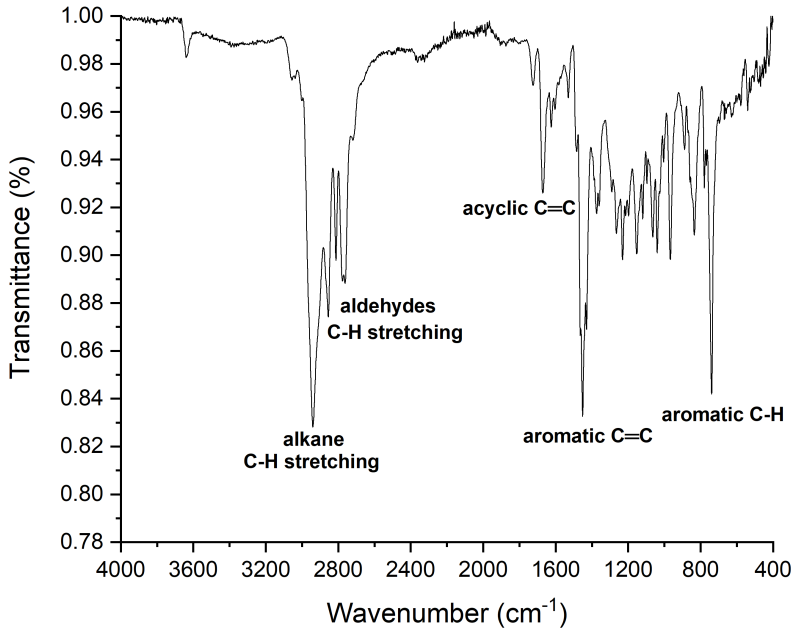


Figure 4.1: FT-IR spectrum of COL.

4.2.1.2 Optical Characterization

COL dissolved in THF with the concentration of (38 μM), owns an absorbance maximum in the visible region at 467 nm, and it emits at 581 nm (Figure 4.2). Its fluorescence quantum yield in the THF was calculated as 65%.

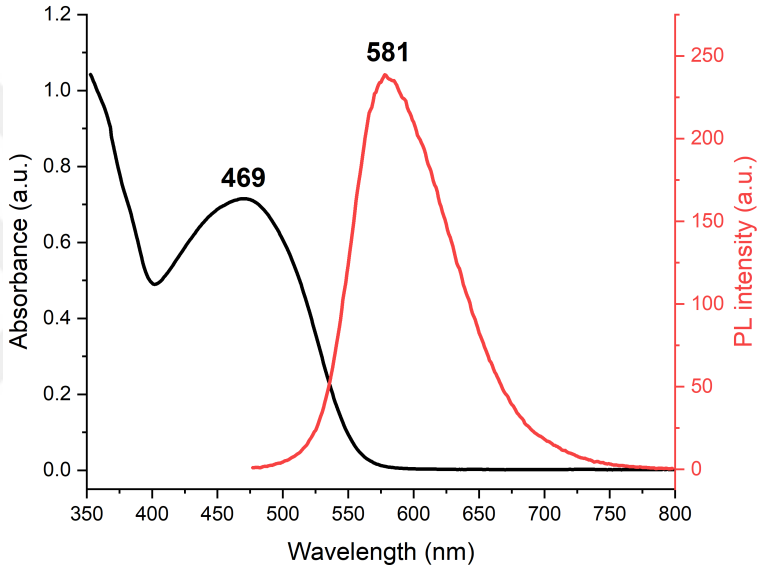


Figure 4.2: UV-Vis absorbance and fluorescence spectra of COL dissolved in THF.

Figure 4.3 demonstrates the photoluminescence decay curve of the conjugated oligomer dissolved in THF (38 μM). The resulting decay curves were fitted by two-exponential functions. After fitting the data using the FluoFit software, the average lifetime for COL dissolved in THF was reported as 4.41 ns and 3.30 ns for the intensity-averaged and amplitude-averaged lifetime, respectively.

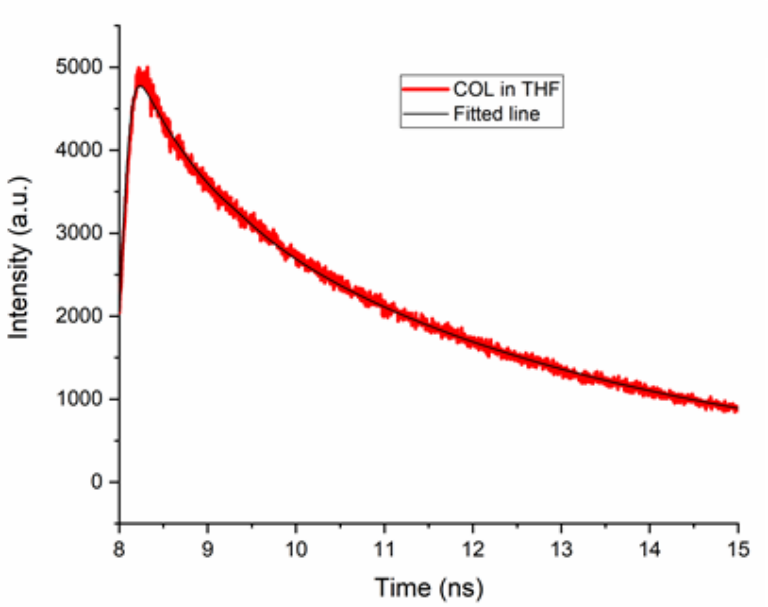


Figure 4.3: Photoluminescence decay curves of COL dissolved in THF, collected at the COL PL emission peak in THF.

4.2.1.3 XPS

Figure 4.4 shows the XPS spectra of conjugated oligomer which was drop casted on the silicon wafer. The resolution scan for the sulfur possesses two doublet peaks at 163.3 ± 0.1 eV and 164.4 ± 0.1 eV for (R-S), and 165.6 ± 0.1 eV and 166.8 ± 0.1 eV for benzothiadiazole (N-S-N). The resolution scan for the carbon owns five peaks at 284.1 ± 0.1 eV for carbon sp^2, 284.8 ± 0.1 eV for carbon sp^3, 285.6 ± 0.1 eV for (C-N), 286.5 ± 0.1 eV for (C-O), and 287.7 ± 0.1 eV for (C=O). The resolution scan for the nitrogen shows at least two peaks at 399.8 ± 0.1 eV for benzothiadiazole (N-S-N) and 399.0 ± 0.1 eV for ($-NR_2$) [129]. The resolution scan for the oxygen depicts at least two peaks at 531.6 ± 0.1 eV and 532.7 ± 0.1 eV, which both correspond to the oxide of organic compounds.

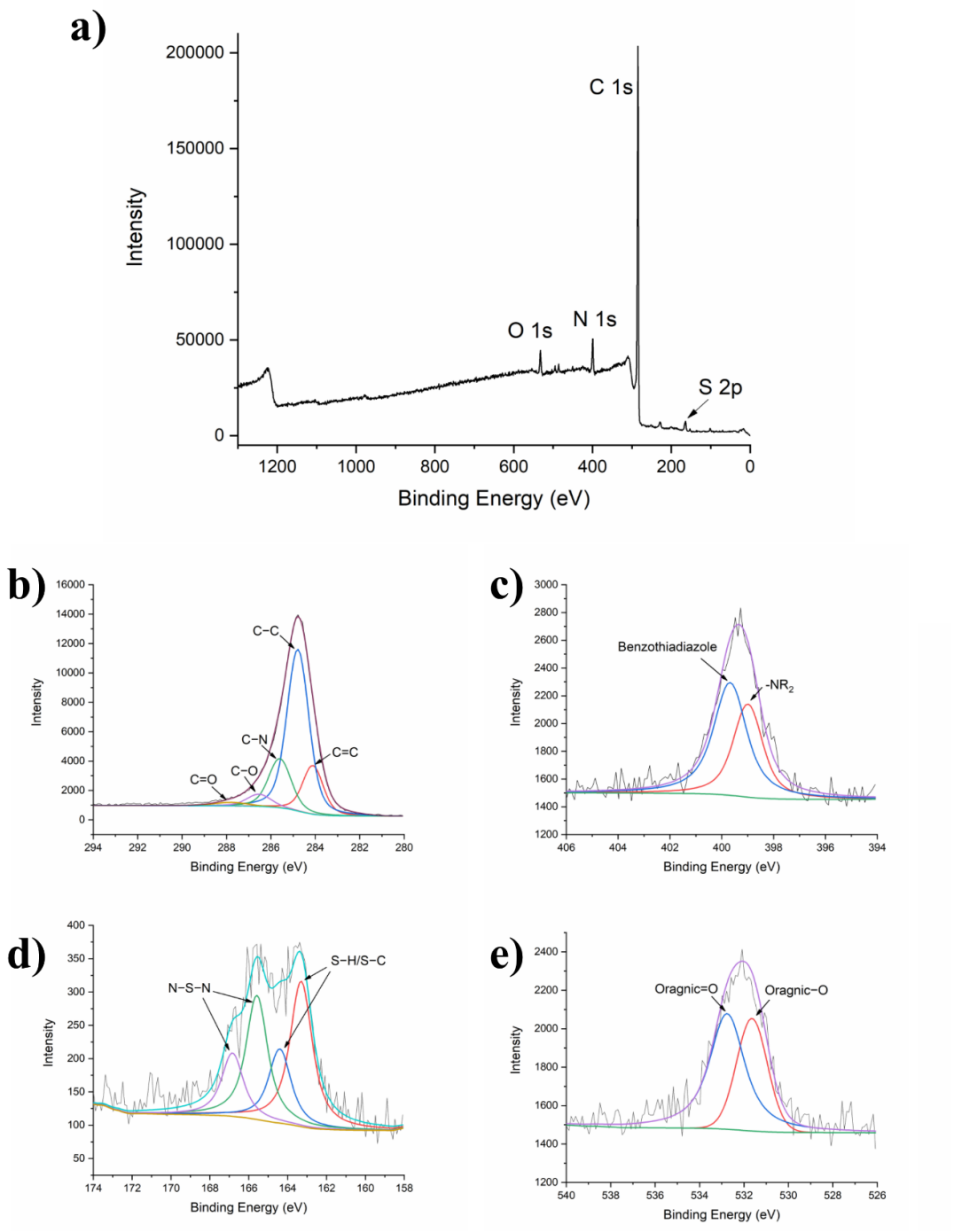


Figure 4.4: The XPS spectra of COL which was drop casted on the silicon wafer. a) Survey scan, b) C 1s , c) N 1s, d) S 2p, and e) O 1s.

4.2.2 Characterization of Water-dispersed Conjugated Oligomer Nanoparticles

4.2.2.1 FT-IR Spectroscopy

A small amount of water-dispersed COL solution was dried out in a 5 ml round bottom flask at room temperature, and the residues were dissolved in THF. For acquiring data, two drops of the resulting solution were added on top of the ATR crystal. The FT-IR spectrum of water-dispersed conjugated oligomer nanoparticles shows sharp peaks at 740, 834, 967, 1,040, 1,130, 1,450, 1,660, 2,750, 2,940 cm^{-1} and a weak broad peak at 3,400 cm^{-1} as expected (Figure 4.5).

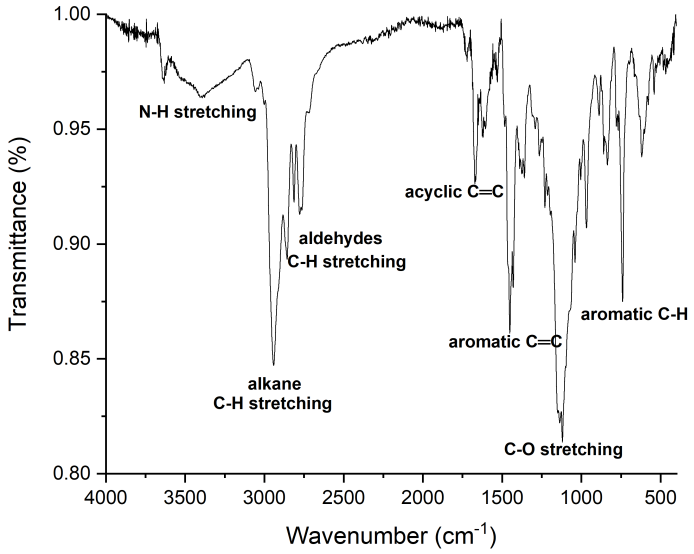


Figure 4.5: FT-IR spectrum of COL nanoparticles.

4.2.2.2 Optical Characterization

Water-dispersed COL nanoparticles with the concentration of ($9.8\mu M$) owns an absorbance maximum in the visible region at 459 nm, and it emits at 617 nm (Figure 4.6). Its fluorescence quantum yield in water was calculated as 6%.

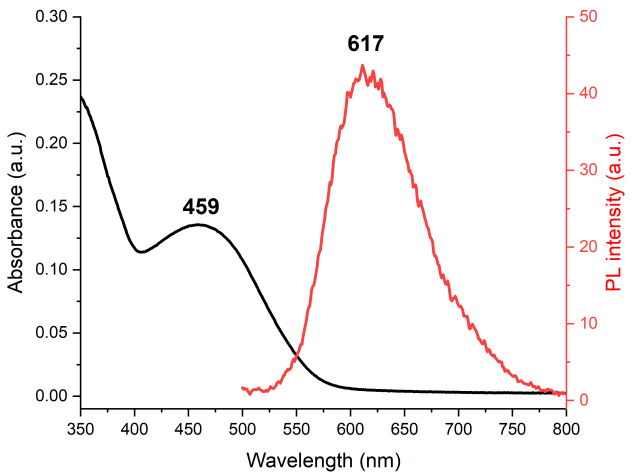


Figure 4.6: UV-Vis absorbance and fluorescence spectra of COL nanoparticles in water.

Figure 4.7 represents the photoluminescence decay curve of the conjugated oligomer dispersed in water ($9.8\mu M$). The resulting decay curves were fitted by two-exponential functions. After fitting the data using the FluoFit software, the average lifetime for COL nanoparticles dispersed in water was reported as 0.50 ns and 0.30 ns for the intensity-averaged and amplitude-averaged lifetime, respectively.

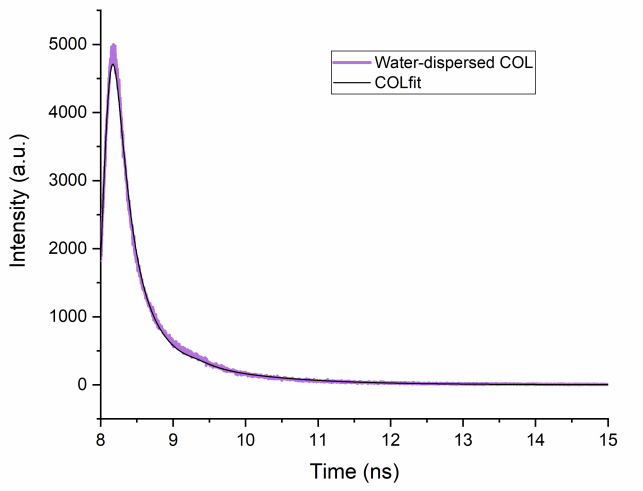


Figure 4.7: Photoluminescence decay curves of COL nanoparticles in water, collected at the COL PL emission peak in water.

4.2.2.3 DLS and Zeta Potential

DLS and zeta potential results of the COL nanoparticles dispersed in water are given in Figure 4.8. The reported z-average size is 107 nm. The sizes reported according to intensity, volume, and number distributions are 120 nm, 105 nm, and 76 nm, respectively. The correlogram is smooth and represents there are no big (like 400 nm) particles in the solution. The PDI value (0.127) can be called perfect for such a colloidal solution, which means the size of particles is uniform. The electrophoretic mobility is reported 3.393 μm.cm/V.s, and the calculated zeta potential is 43.3 mV, which represents stability for this particular colloidal system.

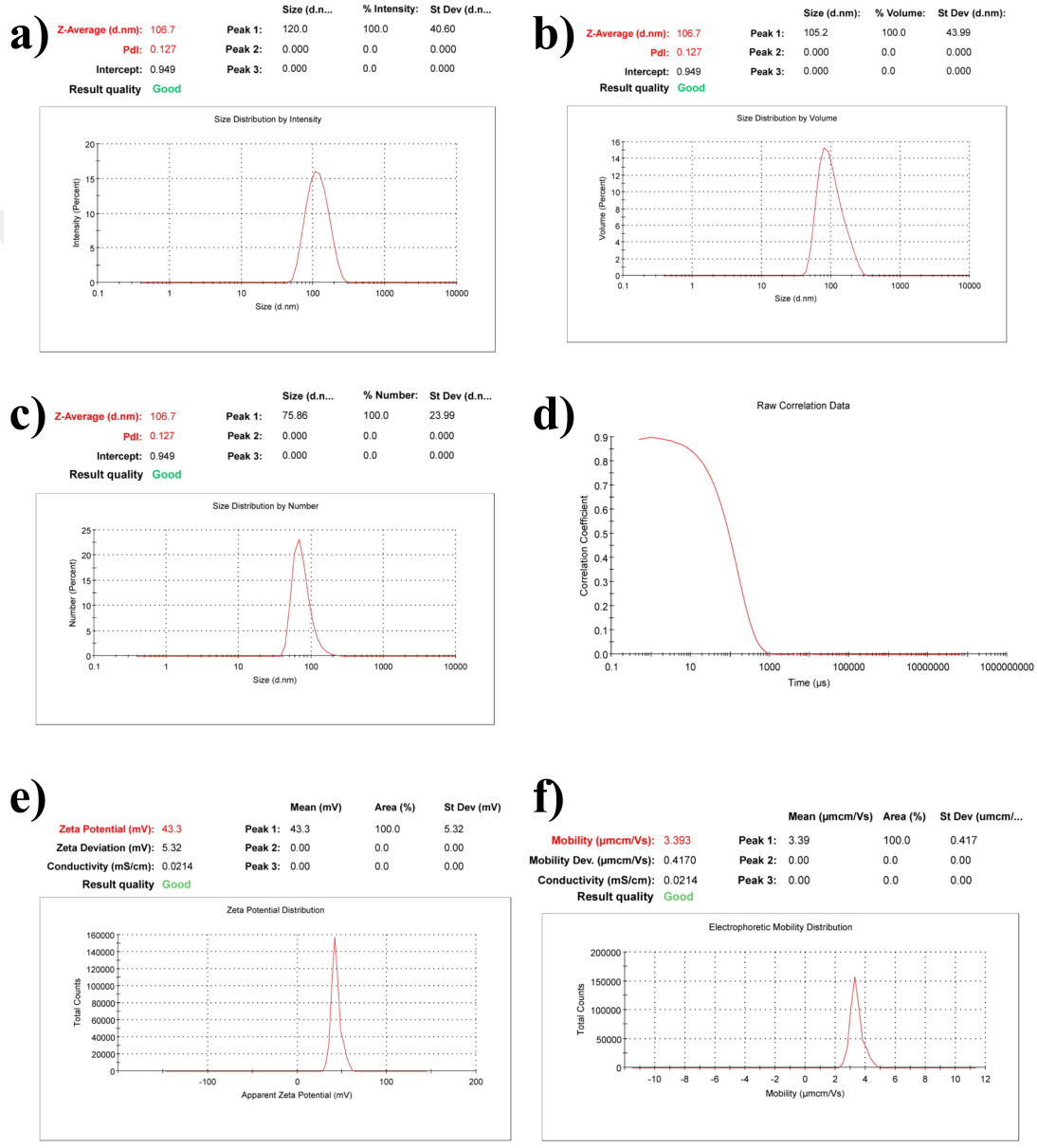


Figure 4.8: DLS and zeta potential results of COL nanoparticles in water. a) intensity distributions, b) volume distributions, c) number distributions, d) correlogram, e) zeta potential, f) electrophoretic mobility.

4.2.2.4 Electron Microscopic Images

According to SEM images (Figure 4.9), the morphology of water-dispersed COL nanoparticles is spherical. The size of these spherical nanoparticles is reported around 70 nm, which is in line with the sizes reported by DLS.

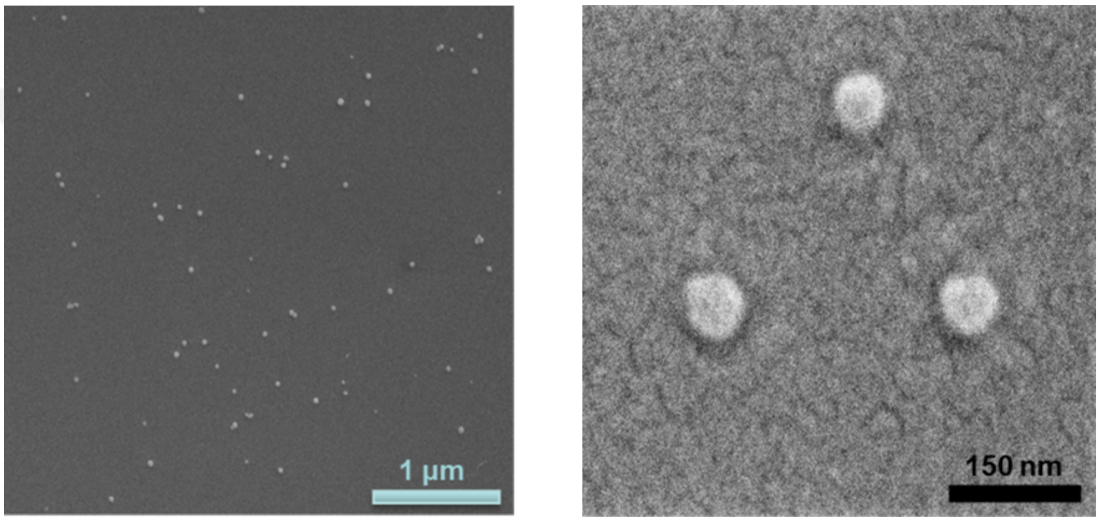


Figure 4.9: SEM images of water-dispersed COL nanoparticles which was drop casted on the silicon wafer.

4.2.2.5 XPS

Figure 4.10 shows the XPS spectra of water-dispersed COL nanoparticles, which was drop casted on the silicon wafer. The resolution scan for the carbon owns five peaks at 284.1 ± 0.1 eV for carbon sp^2, 284.8 ± 0.1 eV for carbon sp^3, 285.6 ± 0.1 eV for (C-N), 286.4 ± 0.1 eV for (C-O), and 287.7 ± 0.1 eV for (C=O). The resolution scan for the oxygen depicts at least two peaks at 531.5 ± 0.1 eV and 532.6 ± 0.1 eV, which both correspond to the oxide of organic compounds. The resolution scan for the sulfur possesses two doublet peaks at 163.4 ± 0.1 eV and 164.4 ± 0.1 eV for (R-S), and 165.7 ± 0.1 eV and 166.9 ± 0.1 eV for benzothiadiazole (N-S-N). The resolution scan for the nitrogen shows at least two peaks at 399.8 ± 0.1 eV for benzothiadiazole (N-S-N) and 399.0 ± 0.1 eV for ($-NR_2$).

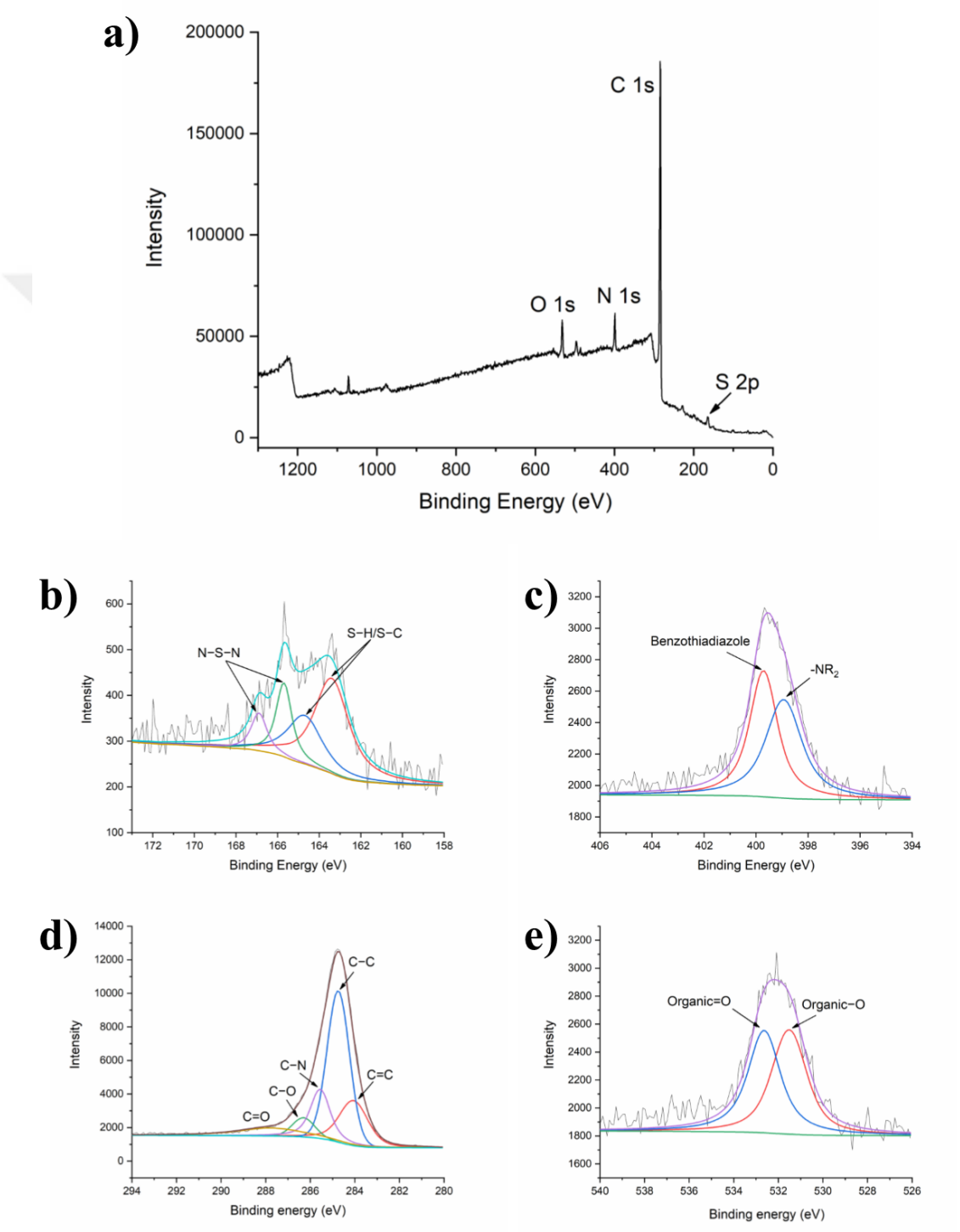


Figure 4.10: The XPS spectra of water-dispersed COL which was drop casted on the silicon wafer. a) Survey scan, b) S 2p, c) N 1s, d) C 1s , and e) O 1s.

4.2.3 Characterization of Water-dispersed Au@COL Nanoparticles

4.2.3.1 FT-IR Spectroscopy

A small amount of water-dispersed Au@COL solution was dried out in a 5 ml round bottom flask at room temperature, and the residues were dissolved in THF. For acquiring data, two drops of the resulting solution were added on top of the ATR crystal. The FT-IR spectrum of Au@COL nanoparticles shows sharp peaks at 3,100, 3,000, 2,850, 1,650, 1,470, 1,240 cm^{-1} as expected (Figure 4.11).

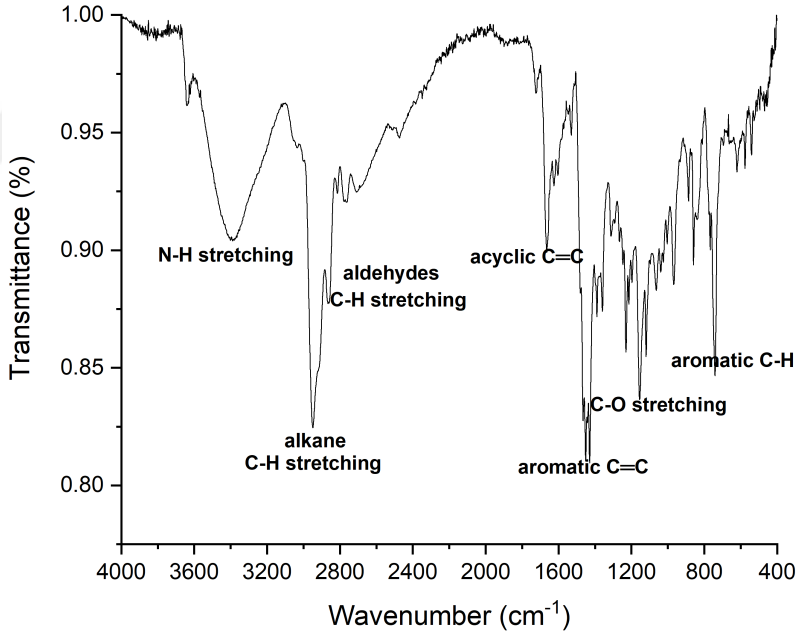


Figure 4.11: The FT-IR spectrum of Au@COL nanoparticles.

4.2.3.2 Optical Characterization

Au@COL nanoparticles in water with the concentration of ($9.79\mu M$) owns an absorbance maximum in the visible region at 457 nm, and it emits at 620 nm (Figure 4.12). Its fluorescence quantum yield in water was calculated as 3%.

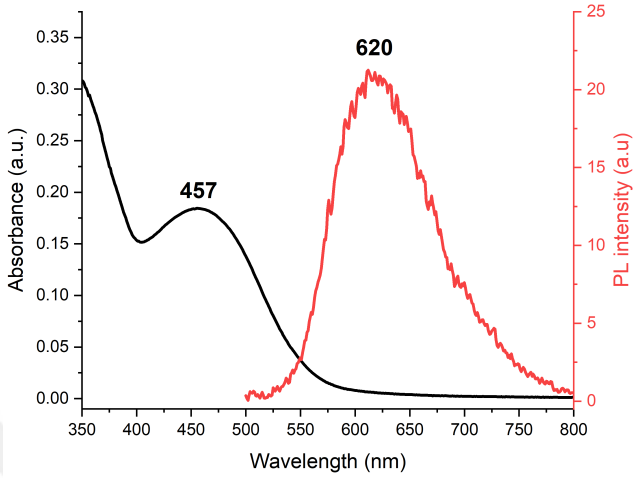


Figure 4.12: UV-Vis absorbance and fluorescence spectra of Au@COL nanoparticles in water.

Figure 4.13 represents of the photoluminescence decay curve of the Au@COL nanoparticles in water (9.8 μM). The resulting decay curves were fitted by two-exponential functions. After fitting the data using the FluoFit software, the average lifetime for Au@COL nanoparticles dispersed in water was reported as 0.37 ns and 0.20 ns for the intensity-averaged and amplitude-averaged lifetime, respectively.

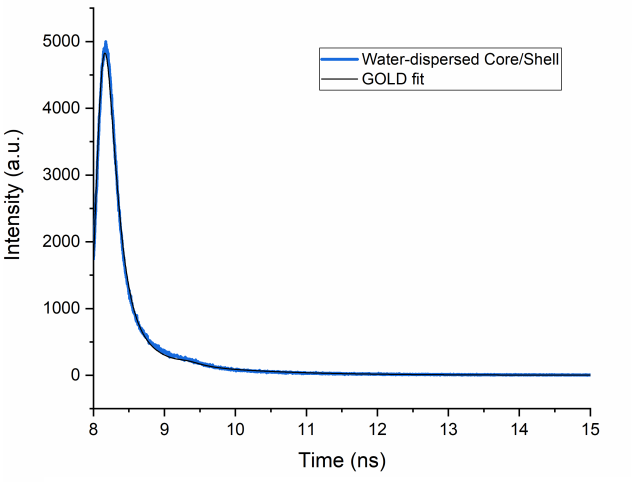


Figure 4.13: Photoluminescence decay curves of Au@COL nanoparticles in water, collected at the Au@COL nanoparticles PL emission peak in water

4.2.3.3 DLS and Zeta potential

DLS and zeta potential results of Au@COL dispersed in water are given in Figure 4.14. The reported z-average size is 75. The sizes reported according to intensity, volume, and number distributions are 89 nm, 61 nm, and 45 nm, respectively. The correlogram is smooth and represents there are no big (like 400 nm) particles in the solution. The PDI value (0.249) can be called perfect for such a colloidal system, which means the size of particles is uniform. The electrophoretic mobility is reported 3.68 μm.cm/V.s, and the calculated zeta potential is 47.0 mV, which represents stability for this particular colloidal system.

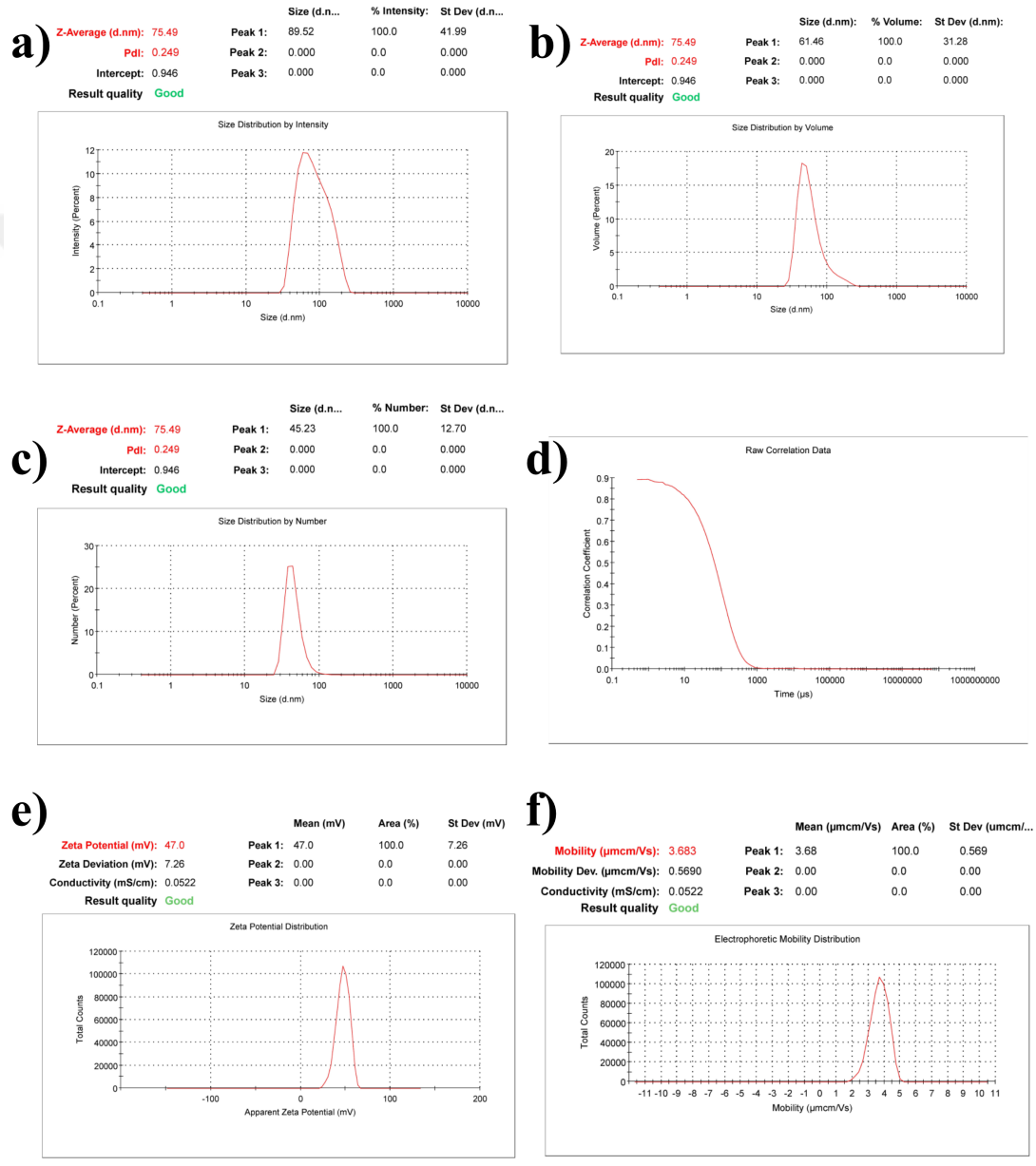


Figure 4.14: DLS and zeta potential measurements of Au@COL nanoparticles in water. a) intensity distributions, b) volume distributions, c) number distributions, d) correlogram, e) zeta potential f) electrophoretic mobility.

4.2.3.4 Electron Microscopic Images

According to SEM and TEM images, the morphology of the Au@COL nanoparticles is spherical. The average size of these spherical nanoparticles is reported around 60 ± 10 nm, which is in line with the sizes reported by DLS. The average size of cores is calculated by ImageJ software and reported in the range of 7 ± 2 nm (Figure 4.15).

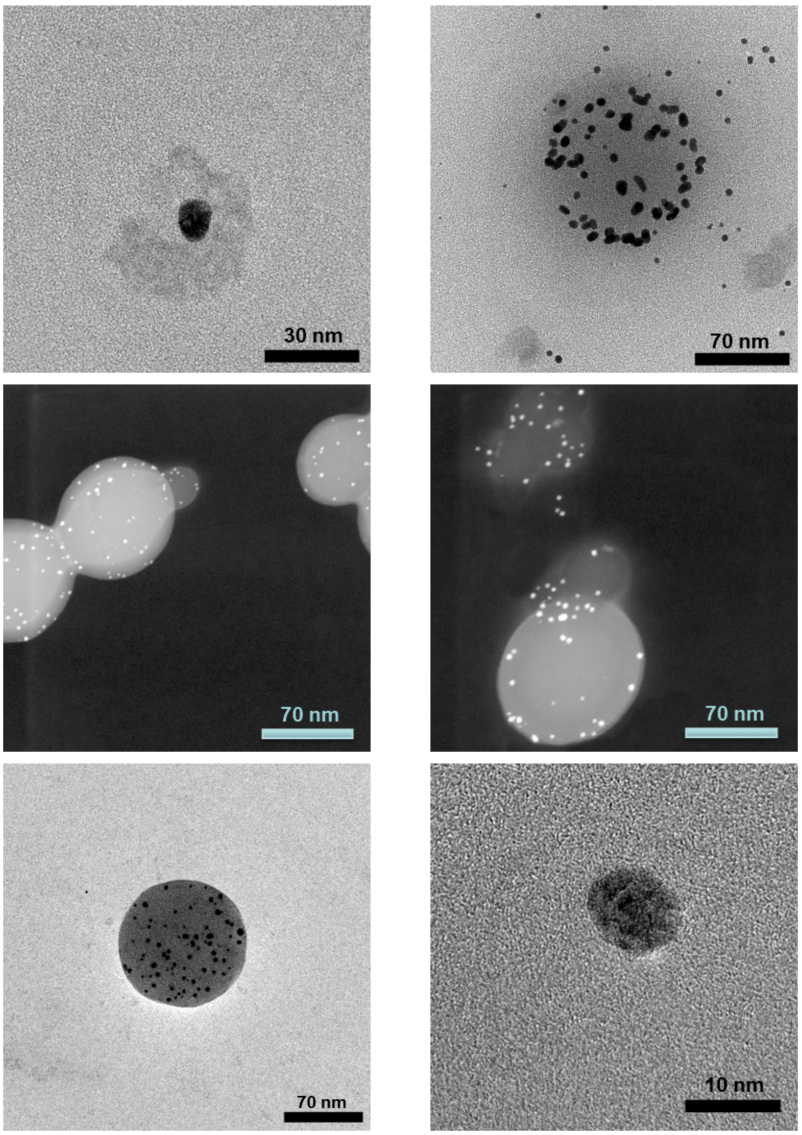


Figure 4.15: TEM and HAADF-STEM images of Au@COL nanoparticles.

The EDX analysis of the Au@COL nanoparticles shows the gold peaks. The peak of copper comes from the TEM support grid. For this measurement, the area shown in Figure 4.16 is selected. Bright spots are the cores, which are gold nanoparticles, and the cloudy gray area is the shell, which is the COL.

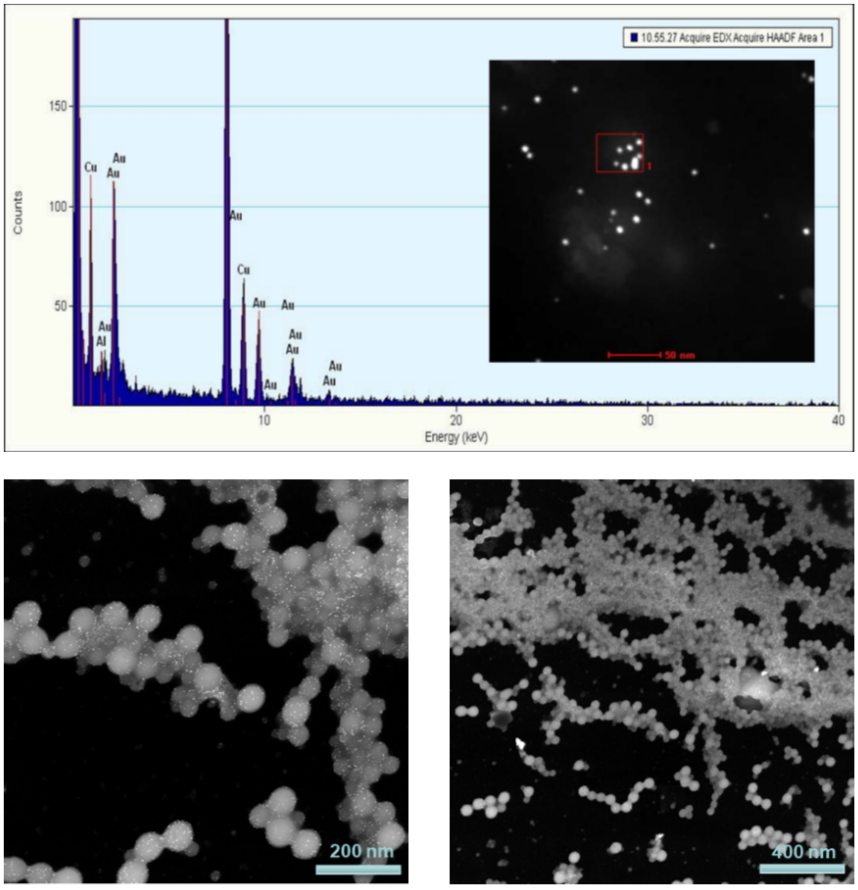


Figure 4.16: EDX spectrum and HAADF-STEM images of Au@COL nanoparticles.

4.2.3.5 XPS

Figure 4.17 shows the XPS spectra of water-dispersed Au@COL nanoparticles which was drop casted on the silicon wafer. The resolution scan for the carbon owns five peaks at 284.1 ± 0.1 eV for carbon sp^2, 284.8 ± 0.1 eV for carbon sp^3, 285.6 ± 0.1 eV for (C-N), 286.4 ± 0.1 eV for (C-O/C-Cl_x), and 287.7 ± 0.1 eV for (C=O). The resolution scan for the oxygen depicts at least two peaks at 531.8 ± 0.1 eV and 532.9 ± 0.1 eV, which both are corresponded to oxide of organic compounds. The resolution scan for the chlorine depicts a doublet peak at 198.6 ± 0.1 eV (Cl $2p_{3/2}$) and 200.2 ± 0.1 eV (Cl $2p_{1/2}$), which is corresponded to metal chlorides such as $AuCl_3$ and NaCl. The resolution scan for the gold represents at least three doublet peaks at 84.0 ± 0.1 eV and 87.6 ± 0.1 eV for elemental gold (Au^0), 85.0 ± 0.1 eV and 88.6 ± 0.1 eV for (Au^{+1}), and 85.9 ± 0.1 eV and 89.5 ± 0.1 eV for (Au^{+3}). The resolution scan for the sulfur possesses three doublet peaks at 163.5 ± 0.1 eV and 164.6 ± 0.1 eV for (R-S), 165.6 ± 0.1 eV and 166.7 ± 0.1 eV for benzothiadiazole (N-S-N), and 167.9 ± 0.1 eV and 169.0 ± 0.1 eV for (R-SO_x). The resolution scan for the nitrogen shows at least three peaks at 399.7 ± 0.1 eV for benzothiadiazole (N-S-N), 398.8 ± 0.1 eV for (-NR_2) and 402.3 ± 0.1 eV for (-NH_3^+) [130].

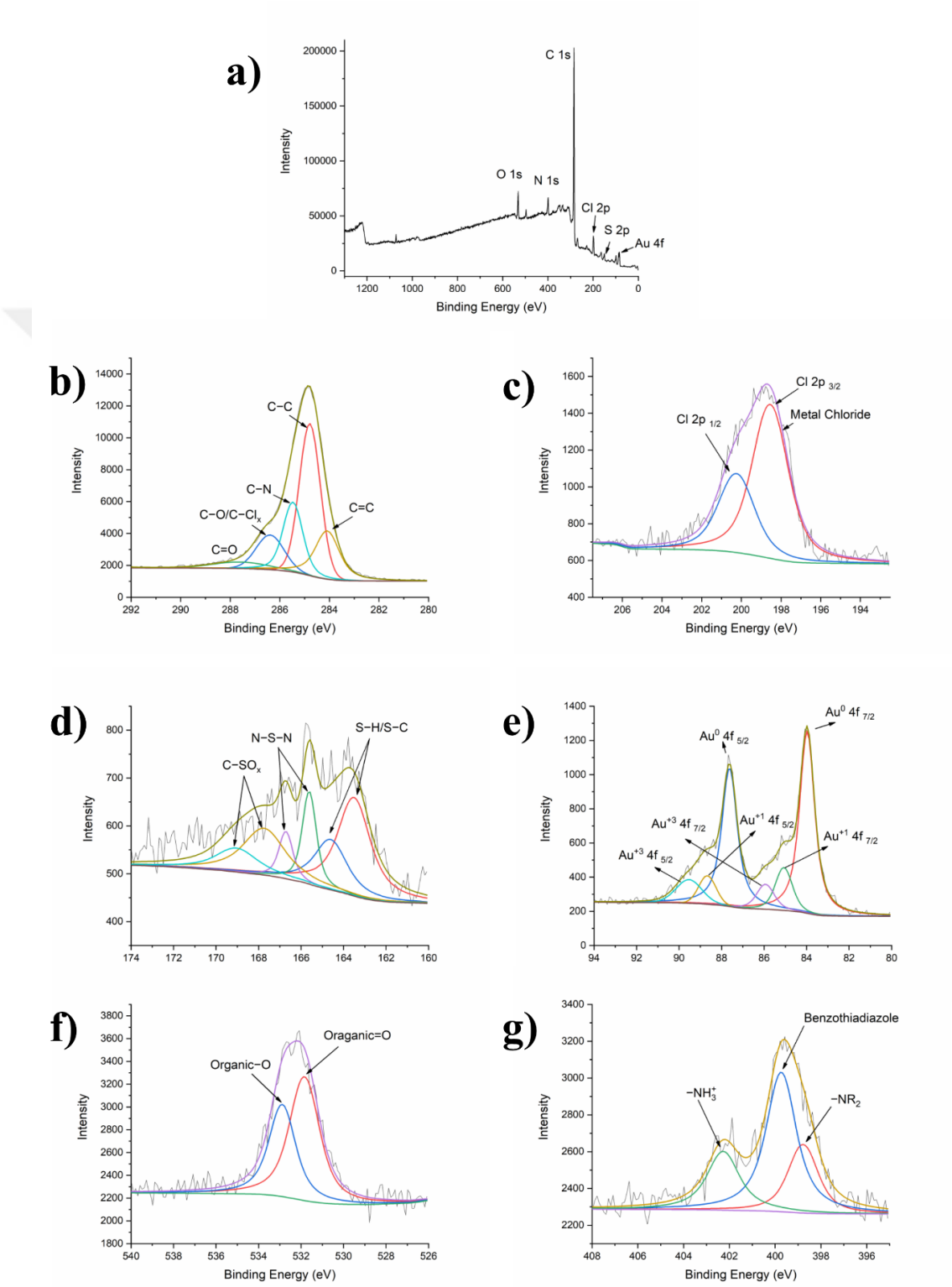


Figure 4.17: The XPS spectra of water-dispersed Au@COL which was drop casted on the silicon wafer. a) Survey scan, b) C 1s, c) Cl 2p d) S 2p , e) Au 4f f) O 1s, and g) N 1s.

4.2.3.6 XRD

For acquiring data, a sufficient amount of water-dispersed Au@COL was drop casted on the microscope slide. The X-ray diffraction (XRD) patterns of the Au@COL nanoparticles are shown in Figure 4.18. It is evident from the pattern that the conjugated oligomer itself is amorphous however the 2θ peaks obtained at 38.1, 44.3, 64.5, and 77.7 corresponds to the reflections from the (111), (200), (220), and (311) planes for gold nanoparticles inside the shell. The peak corresponding to (111) plane has the height intensity, signifying the predominant orientation of (111) plane in the gold nanoparticles [131].

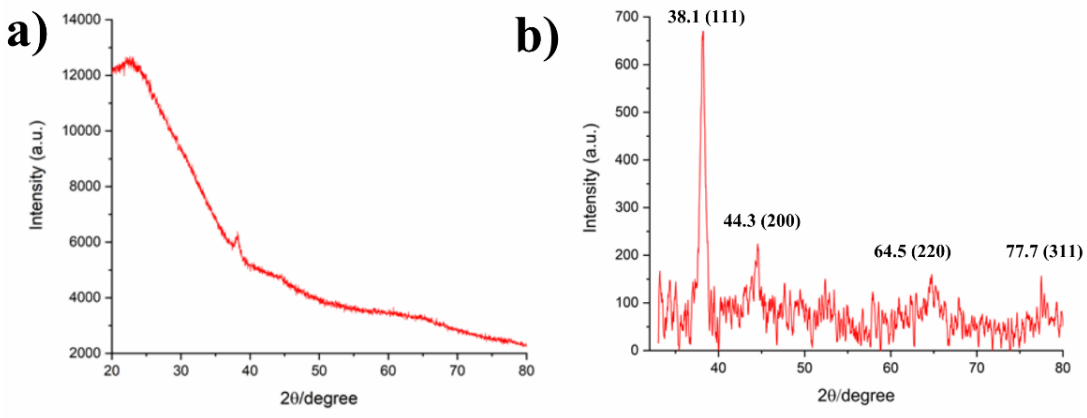


Figure 4.18: X-ray diffraction pattern of Au@COL nanoparticles (drop casted on glass). a) The overall shape of pattern, b) baseline corrected pattern.

4.3 Interpretation of Characterization Data

Figure 4.19 shows the suggested mechanism of spontaneous reduction of gold ions and the formation of gold atoms. While the COL dissolved in THF is added to the gold aqueous solution, the gold ions will be trapped inside the formed COL nanoparticles. The encapsulated gold ions will undergo reduction and form gold atoms. These gold atoms will form nuclei and eventually, due to the coalescence of the gold nuclei, the gold nanoparticles will be formed inside the COL nanoparticles (Figure 4.20). According to this straightforward mechanism, the confined gold ions can coordinate with the nucleophile species such as sulfur residues and amine groups as well as forming π–ion complexes with the benzene rings of the oligomer backbone. The nitrogen in tertiary alkyl amine can transfer electrons to the gold ions and form gold atoms. At the end of this reaction, the tertiary alkyl amine (NR_3) will be converted to alkyl amine (R-NH_2). As it is depicted in Figure 4.19, the formed formaldehyde can also act as a reducing agent. It reduces gold ions to gold atoms and produces formic acid. Production of formic acid and the presence of chlorine ions will decrease the pH of the solution. The protons (H^+) will make a coordinate covalent bond with the nitrogen of alkyl amine and will produce protonated alkyl amine (R-NH_3^+).

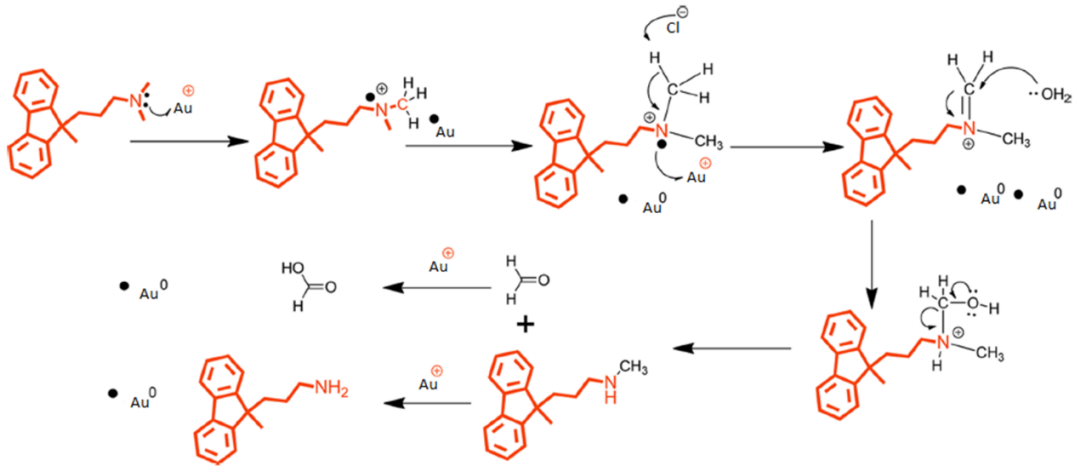


Figure 4.19: Suggested mechanism of reduction of gold ions and formation of gold atoms.

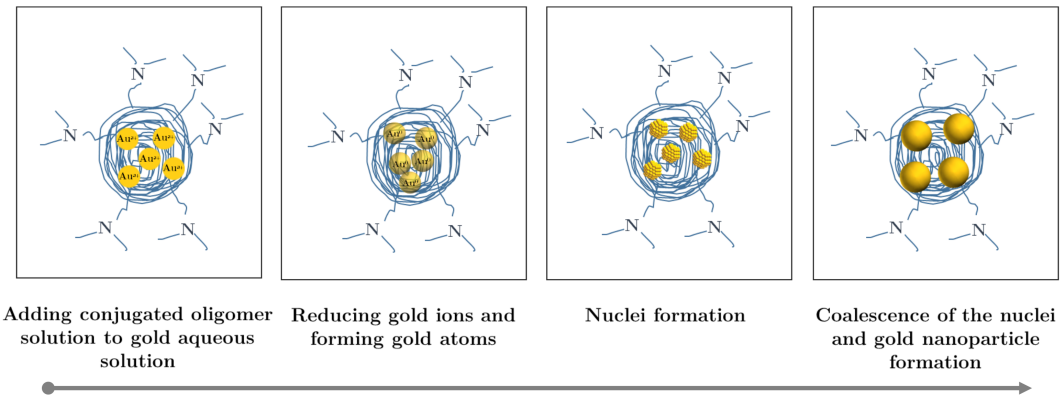


Figure 4.20: The scheme of formation of gold nanoparticles inside the shell.

4.3.1 Optical properties

The optical properties of COL dissolved in THF, COL nanoparticles in water and Au@COL nanoparticles in water are different. UV-Vis absorbance and fluorescence spectra of these three structures can be found in Figure 4.21. According to this Figure, the Stokes shift of COL dissolved in THF is 112 nm while when the solvent is changed from THF to water the shift is 158 nm. In the case of water-dispersed Au@COL nanoparticles, the change is even greater and calculated as 163 nm. The main reasons for changes in the magnitude of the Stokes shift are changes in the chemical structure of the oligomer and polarity of the solvent. As explained earlier, the gold ions can convert tertiary alkyl amine (NR_3) to alkyl amine (R-NH_2). The change in polarity of the solvent can cause a blue or red-shift in the position of the absorbance maxima peak. With these results, it can be concluded that the excited state of COL is less polar in comparison to its ground state. The polar solvent tries to stabilize the ground state more than the excited state. In this case, the gap between excited and the ground increases, which means higher energy is required for excitation, and there will be a blue shift in the spectrum. For both the COL nanoparticles in water and Au@COL nanoparticles in water cases, the fluorescence lifetime and quantum yield are significantly decreased, which indicate the contribution of the nonradiative channels has been significantly increased. The change in the dielectric and polarity of the solvent, and the chemical structure of the COL may cause this. Table 4.1 summarizes all

the optical properties of the three structures.

Table 4.1: The overall optical properties of COL dissolved in THF, COL nanoparticles in water, and Au@COL nanoparticles in water.

Sample	λ_{Abs} (nm)	λ_{Em} (nm)	Stokes shift (nm)	Florescence lifetime (ns)	Φ_f (%)
COL dissolved in THF	469	581	112	4.41	65
COL nanoparticles in Water	459	617	158	0.49	6
Au@COL nanoparticles in Water	457	620	163	0.36	3

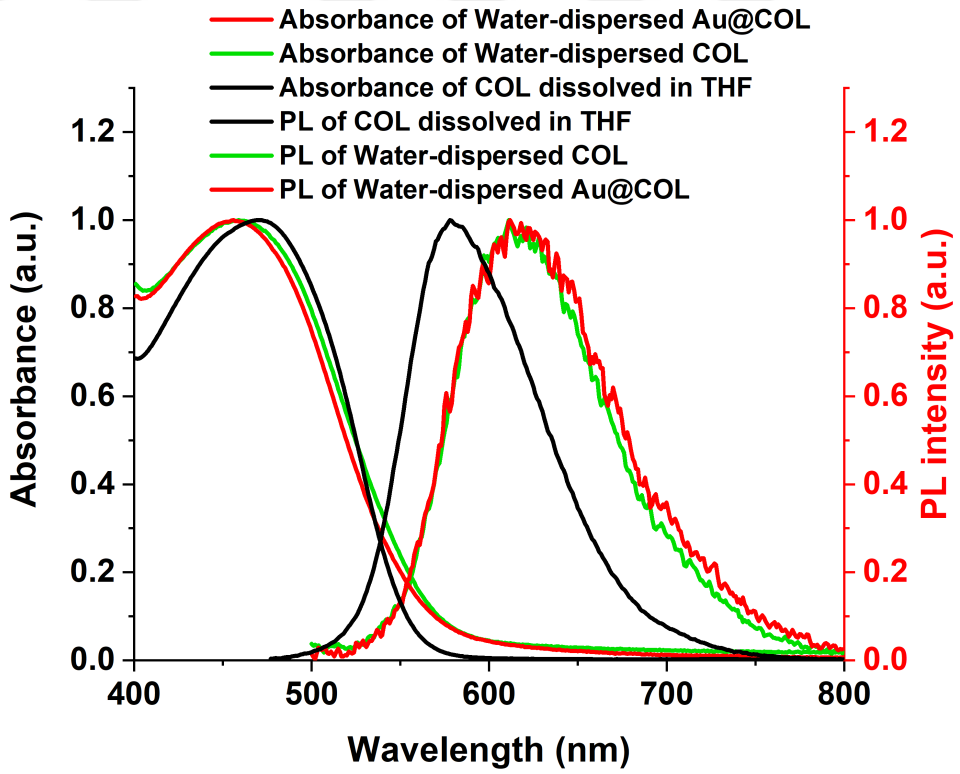


Figure 4.21: UV-Vis absorbance and fluorescence spectra of COL dissolved in THF, COL nanoparticles in water, and Au@COL nanoparticles in water.

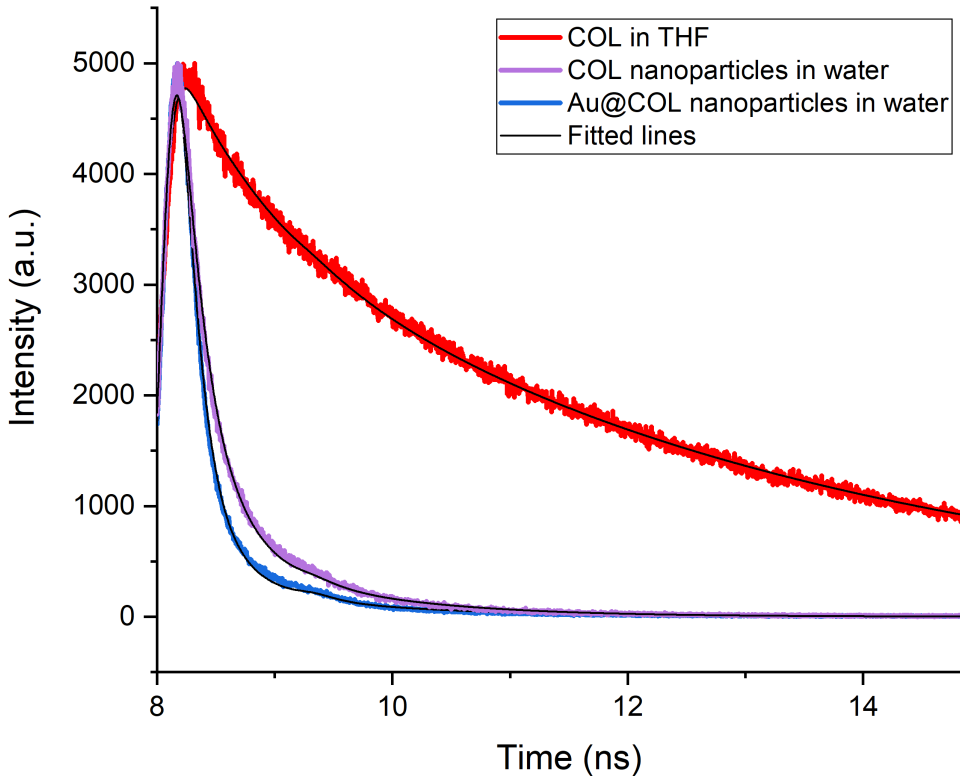


Figure 4.22: Photoluminescence decay curves of COL dissolved in THF, COL nanoparticles in water, and Au@COL nanoparticles in water, collected at the their PL emission peak.

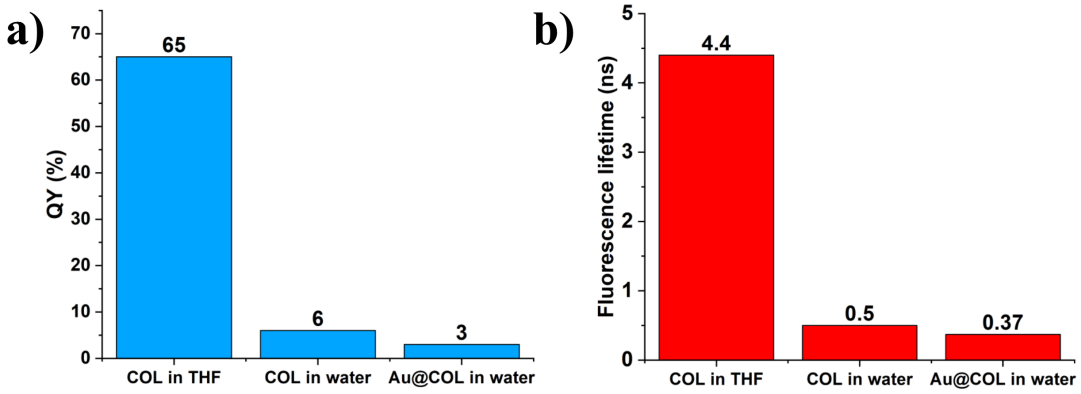


Figure 4.23: a) Quantum yield comparison bar chart, b) Fluorescence lifetime comparison bar chart.

4.3.2 Structural Analyses

A comparison of the FT-IR spectrum of all three structures suggests changes in the chemical structure of COL. Figure 4.24 depicts the differences in position and intensity of peaks. Three regions of A, B, and C are marked in this figure. According to the suggested mechanism, the gold ions can convert tertiary alkyl amine (NR_3) to alkyl amine (R-NH_2). The region A shows a significant increase in the intensity of 3,400 cm^{-1} peak, which belongs to N-H stretching of primary amines. The region B shows a noticeable decrease in intensity of 2,770 cm^{-1} doublet peak, which belongs to C-H stretching of aldehyde. This decrease supports the suggested mechanism, which claims that the formed formaldehyde will be oxidized to formic acid. In the region C, a peak in 1,310 cm^{-1} has appeared which belongs to S=O stretching in sulfone. These results are further verified by XPS results.

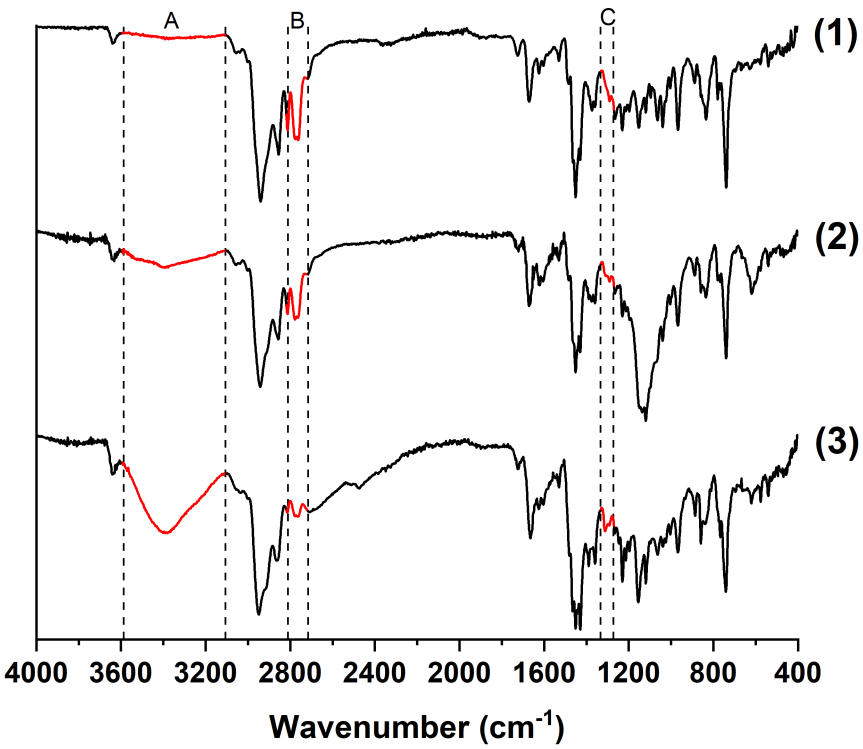


Figure 4.24: FT-IR spectra of (1) COL, (2) water-dispersed COL nanoparticles, and (3) water-dispersed Au@COL nanoparticles in one plot.

The XPS spectra of drop casted COL, water-dispersed COL nanoparticles and water-dispersed Au@COL nanoparticles on the silicon wafer illustrates some changes in the position and intensity of peaks of carbon, nitrogen, and sulfur. In Figure 4.25, all the spectrum of all three structures has been drawn. In the carbon spectrum, the peak at 286.5 eV in Au@COL nanoparticles in water, which belongs to C-O and C-Cl bonds has a higher intensity in comparison to two other structures. The presence of chlorine ions in the solution and the formation of formic acid have increased the intensity of this peak. In the nitrogen spectrum, the peak at 402.3 $\pm$ 0.1 eV is only can be seen in Au@COL nanoparticles in water which represents the formation of (-NH_3^+) due to the presence of protons (H^+) in the solution. The hike of this peak also has been seen in the FT-IR spectrum. In the sulfur spectrum, the formation of sulfone can be only confirmed in Au@COL nanoparticles in water structure since the doublet peak at 167.9 $\pm$ 0.1 eV, and 169.0 $\pm$ 0.1 eV can be only seen in the spectrum of Au@COL nanoparticles in water. Moreover, the spectrum of gold in Au@COL nanoparticles in the water structures shows three different species that belong to gold nanoparticles, Au-S, and Au-Cl.

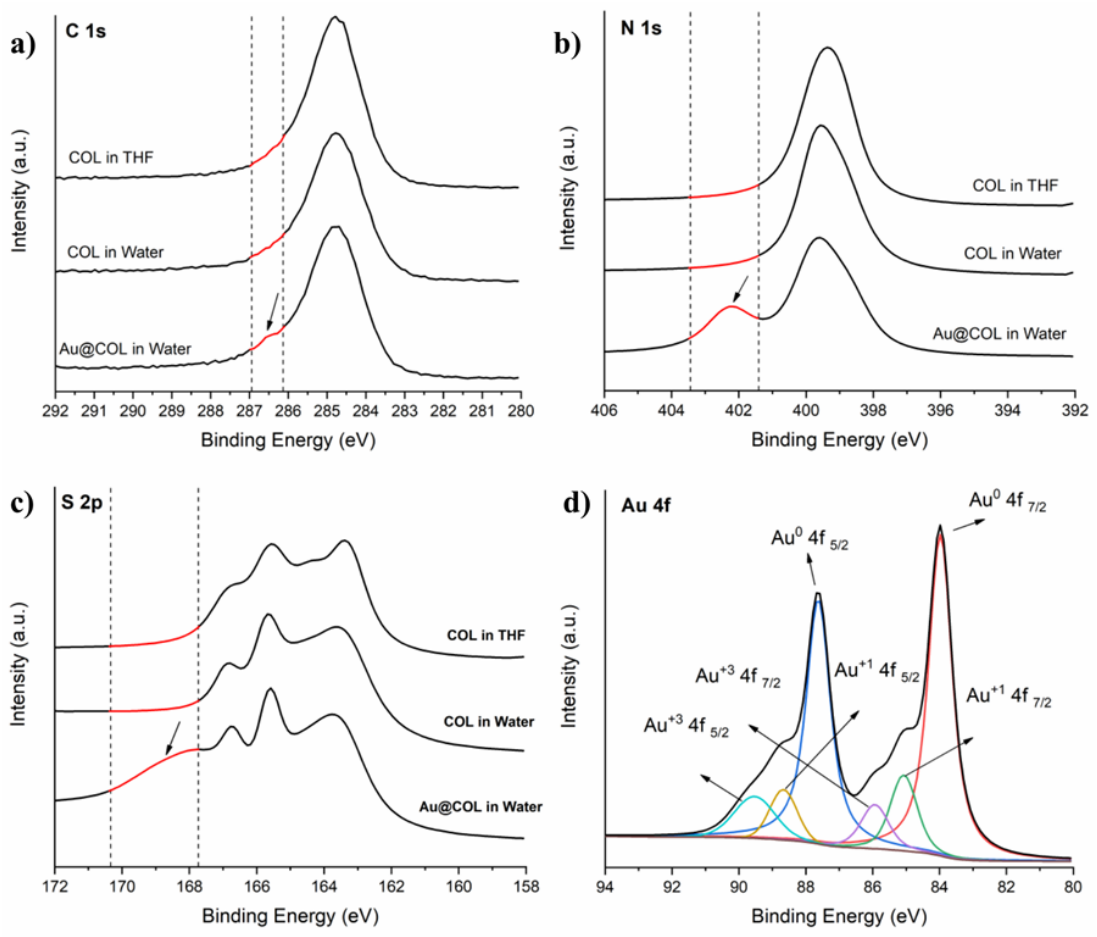


Figure 4.25: Comparison XPS diagram of COL dissolved in THF, COL nanoparticles in water, and Au@COL nanoparticles in water. a) C 1s, b) N 1s, c) S 2p, d) Au 4f.

The HRTEM image of gold nanoparticles can reveal some information about the distance among the planes of gold. In Figure 4.26, the distance between two adjacent planes (interplanar spacing) has been calculated by ImageJ software and reported 0.23 nm. Since the crystal structure of the gold is FCC, Equation 4.1 will be used. The magnitude of a for the gold is 0.41 nm. After calculation, we can conclude that the image shows reflections from the (111) plane, which occurs at 38.1 degree.

$$d = \frac{a}{\sqrt{h^2 + l^2 + k^2}} \tag{4.1}$$

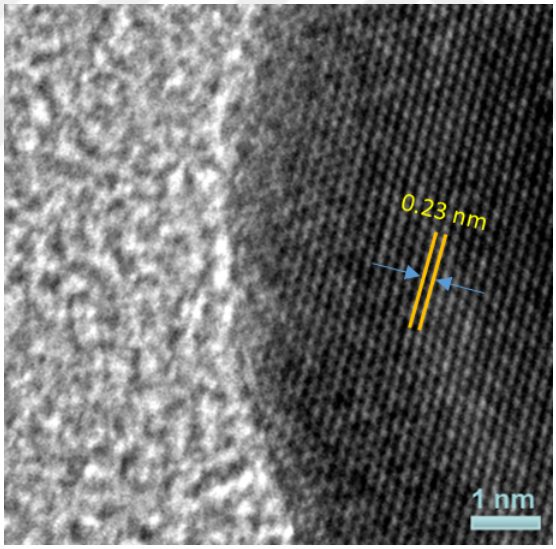


Figure 4.26: HRTEM image of a gold nanoparticle. The interplanar spacing of the particle shows a good agreement with that of the gold (111) plane.

4.3.3 Morphology, Size, and Surface Properties

Both the DLS and zeta potential data of COL nanoparticles in water and Au@COL nanoparticles in water can be found in table 4.2. As mentioned earlier, the zeta potential is very sensitive to the concentration of hydronium ion inside the sample. According to the suggested mechanism, which already has been verified with both the XPS and FT-IR analyses, the estimated pH of the Au@COL nanoparticles aqueous solution should be less than the COL nanoparticles aqueous solution due to both the presence of the chlorine ions and formation of formic acid. Considering this, as expected, the zeta potential of Au@COL nanoparticles is higher. Considering the value of calculated zeta potential, the type of repulsion force among the particles for both cases is electrostatic. The PDI for the COL nanoparticles aqueous solution is almost half of the Au@COL nanoparticles aqueous solution, but the reported size for the COL nanoparticles is greater than the Au@COL nanoparticles. The presence of gold nanoparticles outside of COL nanoparticles, changes in the chemical structure of the COL and pH of the final solution can be the reasons for recording smaller particles and higher PDI in the case of Au@COL nanoparticles aqueous solution in comparison to COL nanoparticles aqueous solution in both the DLS and TEM techniques.

Table 4.2: Summary of reported sizes and calculated zeta potentials.

Sample	PDI	DLS reported size(nm)	TEM reported size(nm)	Zeta potential (mV)
COL NPs in Water	0.127	107	70±10	+ 43.3
Au@COL NPs in Water	0.249	75	50±10	+ 47.0

4.3.4 Stability of the Au@COL nanoparticles aqueous solution over the time

Besides the stability of these colloids in an extended period, another concern is how long the COL shell can keep the gold nanoparticles inside it and maintain the core-shell structure. To answer this question, three samples in a different configuration of core-shell (adding COL dissolved in THF to gold solution), raspberry structure (adding the gold solution to COL nanoparticles in water) and the mixture of both have been synthesized and left in dark and cold place for six months. After that, the samples were characterized by UV-Vis spectroscopy. The results indicate that the shell can protect the gold nanoparticles (the core) and maintain the core-shell structure for at least six months. However, the UV-Vis spectrum shows a significant change in peak position (in comparison to its initial position) of the raspberry structure hybrid nanoparticles that means the unprotected gold nanoparticles have been aggregated and made blocks of gold. It can be concluded that the COL is a reliable shell for holding the gold nanoparticles inside it.

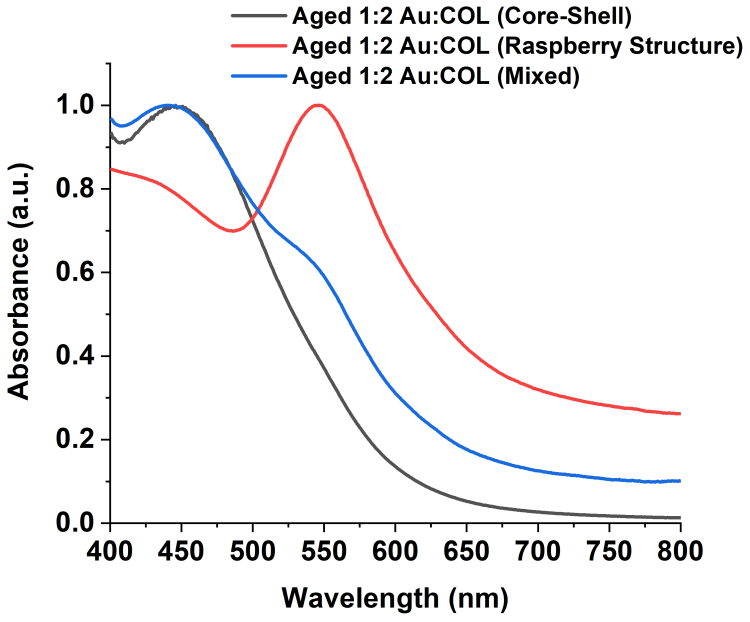


Figure 4.27: UV-Vis absorbance and fluorescence spectra of aged core-shell, aged raspberry structure, and mixture of both structures. The plasmonic peak of gold at 560 nm for raspberry structure is an indication of aggregation of unprotected gold nanoparticles.

4.4 Application of Au@COL Nanoparticles

As discussed earlier, the aim of this work is the design and synthesis of a novel hybrid core-shell nanoparticles, which can be utilized for antibacterial photodynamic therapy. For investigating the efficiency of this novel material application in antibacterial photodynamic therapy, the material has been studied on the E. coli bacteria. The reason for selecting the E. coli bacteria is its resistance to conventional PSs and antibacterial agents and its special properties such as negative surface charge. It is expected that the Au@COL nanoparticles because of their considerably small size and possessing positive charge at their surface can easily penetrate to the shell of E. coli bacteria and kill them while Au@COL nanoparticles have been illuminated with proper wavelength. It is also expected that the Au@COL nanoparticles outperform the COL nanoparticles in killing the efficiency of bacteria since the Au@COL nanoparticles benefit from ME^1O_2, which is absent in COL nanoparticles.

4.4.1 Investigation of PDT-killing of E. coli

4.4.1.1 ROS measurements

The singlet oxygen generation efficiency of both the COL nanoparticles and Au@COL nanoparticles has been studied using the 2,7-dichlorofluorescein (DCFH). The DCFH is a chemical, which is very sensitive to reactive oxygen species (ROS). It will react with the singlet oxygen that the PS has been produced and will be converted to 2,7-dichlorofluorescein (DCF) (Figure 4.28). DCF is a fluorescent material that can emit in 524 nm. The intensity of this emission at that particular wavelength (524 nm) is directly proportional to the amount of singlet oxygen generated by the PS.

With this in mind, the relative efficiency of singlet oxygen generation of different materials can be evaluated. Figure 4.31 shows the relative singlet oxygen generation efficiency of both the COL and the Au@COL nanoparticles aqueous

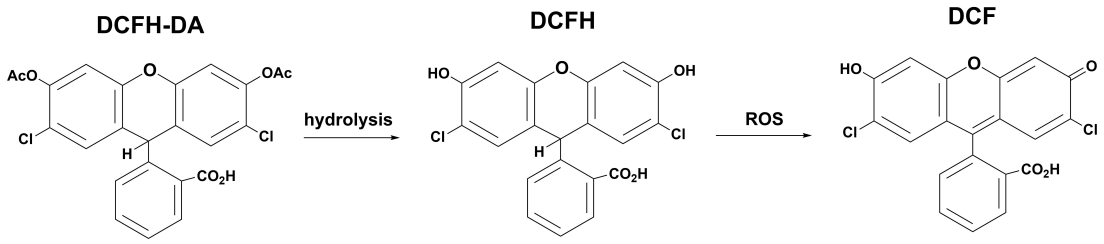


Figure 4.28: The formation of DCF from DCFH in the presence of ROS such as singlet oxygen.

solutions. Changes in the chemical structure and conjugation, presence of gold nanoparticles inside COL shell and different pH of solutions will cause a change in the singlet oxygen generation efficiency of two structures. Singlet oxygen generation of the COL and Au@COL nanoparticles was studied upon exposure to white light with the flux of 1.0 mW/cm^2 for four times and each time for one minute. In the absence of PS, the emission peak at 524 nm did not change much, with adding the Au@COL or COL nanoparticles to the solution and starting the illumination, the peak intensity at 524 nm started increasing significantly and continue raising gradually over the illumination time. The results indicate both the COL and Au@COL nanoparticles are appropriate photosensitizers while they are inactive in the dark and do not generate singlet oxygen. As it is shown in Figure 4.31, the slope of Au@COL nanoparticles is greater than the slope of the COL nanoparticles, which means the Au@COL nanoparticles have higher singlet oxygen capacity induced by metal-enhanced singlet oxygen generation.

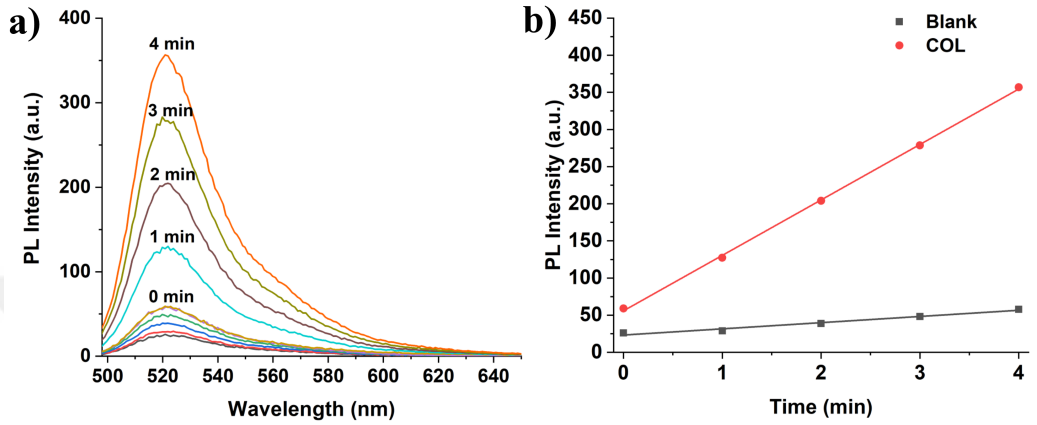


Figure 4.29: a) PL spectra of the DCF in the absence and the presence of (3.1 μM) COL nanoparticles under continuous white light irradiation. b) Time response curve of PL intensity of DCF in the presence of COL nanoparticles and blank (R^2 = 0.98 for blank, R^2 = 0.99 in the presence of COL nanoparticles).

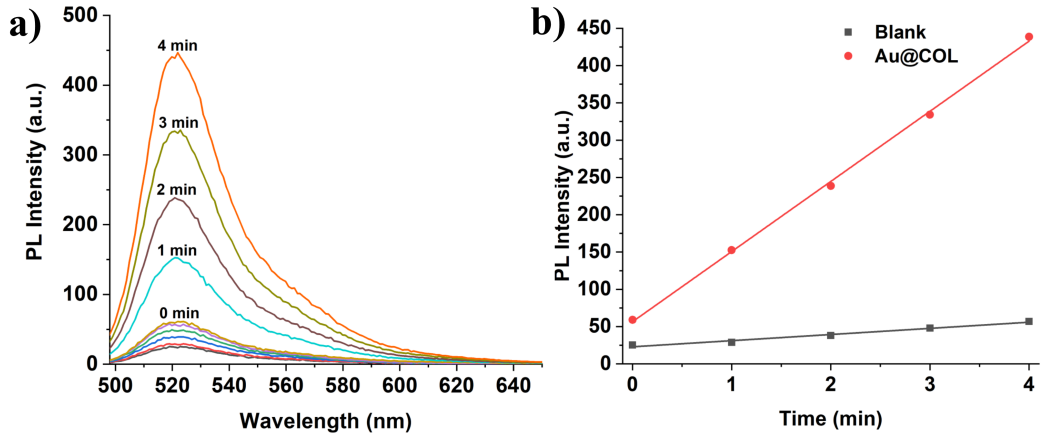


Figure 4.30: a) PL spectra of the DCF in the absence and the presence of (3.1 μM) Au@COL nanoparticles under continuous white light irradiation. b) Time response curve of PL intensity of DCF in the presence of Au@COL nanoparticles and blank (R^2 = 0.97 for blank, R^2 = 0.99 in the presence of Au@COL nanoparticles).

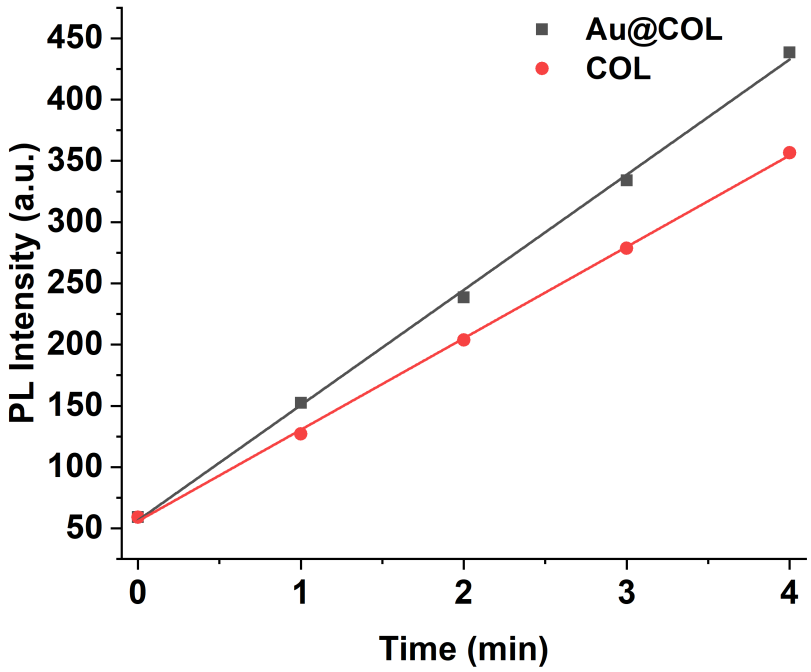


Figure 4.31: Time response curve of PL intensity of DCF in the presence of Au@COL and COL nanoparticles.(slope = 74.65 for COL nanoparticles, slope = 94.04 for Au@COL nanoparticles).

4.4.1.2 Bacterial Survival Experiments

All the light irradiation for bacteria survival experiments in this thesis has been done with the white light with the flux of 22 mW/cm^2 for 30 seconds unless otherwise stated. The MIC values of two structures (under light irradiation) are in line with the results of ROS measurement (Figure 4.32). The Au@COL nanoparticles show a better performance in comparison to COL nanoparticles due to their higher singlet oxygen generation efficiency.

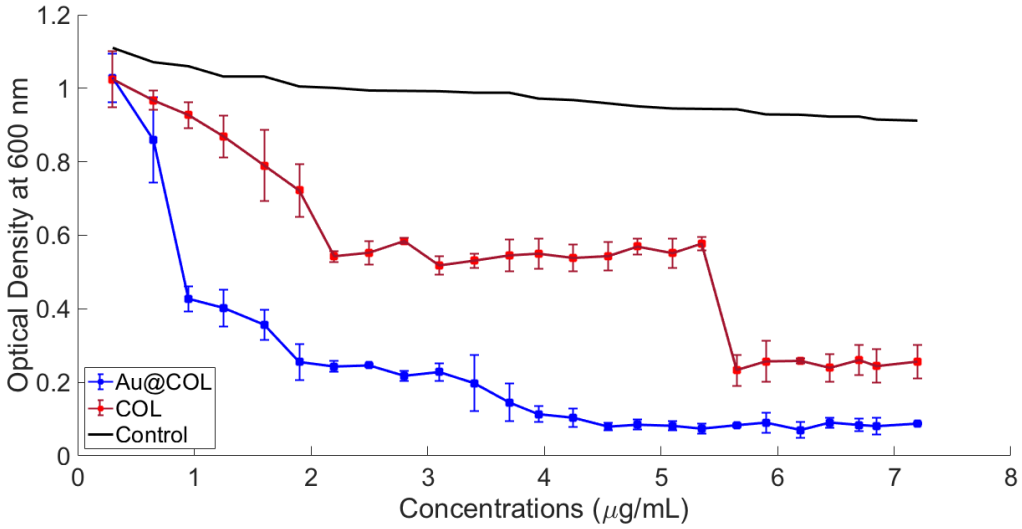


Figure 4.32: MIC assay for different concentration of Au@COL and COL nanoparticles under white light irradiation.

After obtaining the MIC values for both the COL and Au@COL nanoparticles, bacterial survival experiments for each of them were conducted by the spread plate technique in two conditions of dark and under light irradiation. Killing efficiency of E. coli bacteria incubated with COL nanoparticles (5.5 μg/ml concentration) under light irradiation and dark have been determined by colony counting method and reported as 60% and 3%, respectively (Figure 4.33).

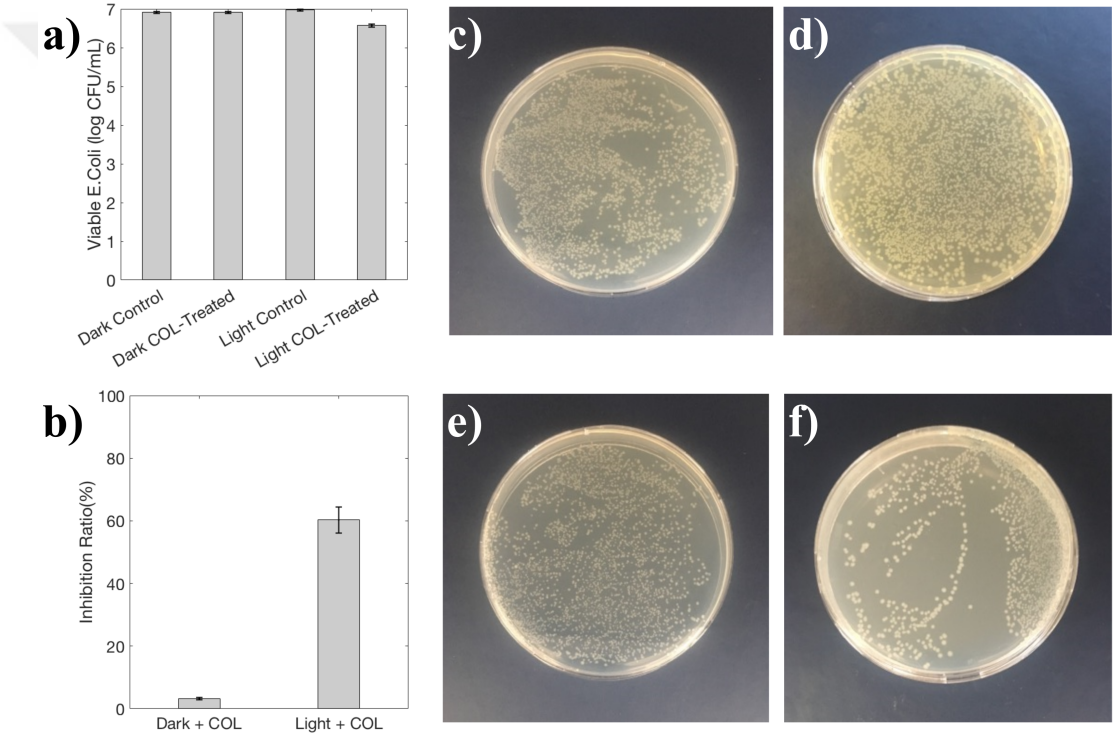


Figure 4.33: a) Biocidal activities of COL nanoparticles toward E. coli in the dark and under light irradiation. b) Inhibition ratio comparison bar chart in the dark and under light irradiation. Plate photographs for E. coli on YTD agar plate treated c) without the COL nanoparticles in the dark (dark control), d) with the COL nanoparticles in the dark, e) without the COL nanoparticles under light irradiation (light control), f) with the COL nanoparticles under light irradiation.

Killing efficiency of E. coli bacteria incubated with Au@COL nanoparticles (4.0 μg/ml concentration) under light irradiation and dark have been determined by colony counting method and reported as 99.8% and 22%, respectively (Figure 4.34).

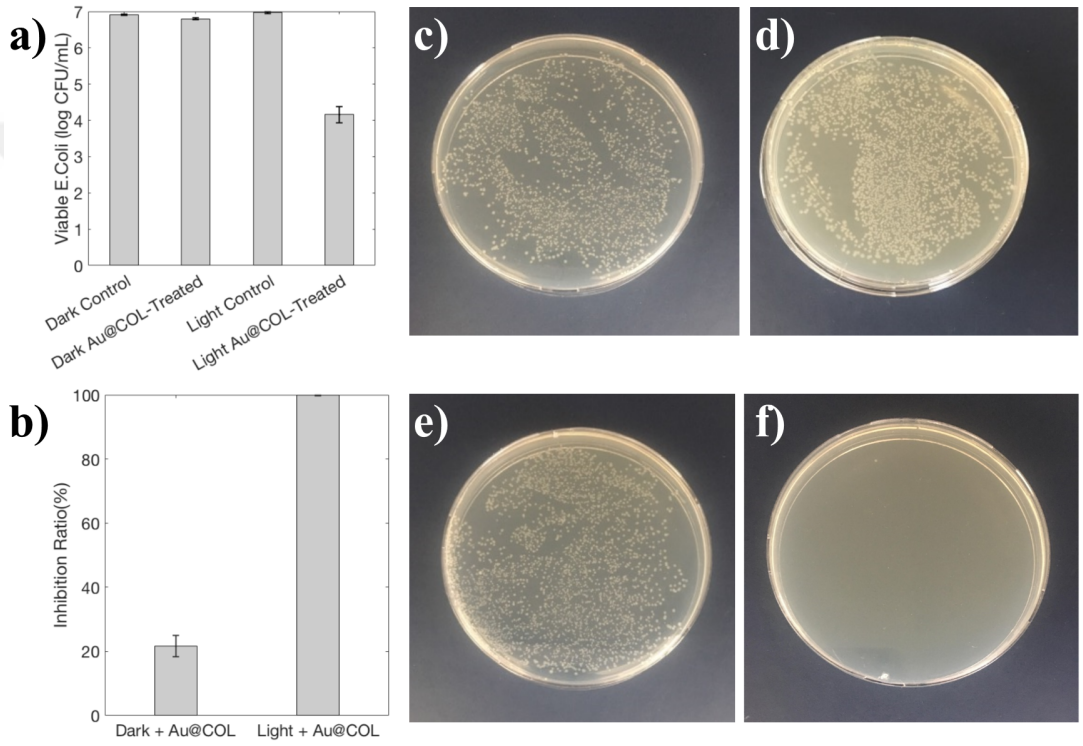


Figure 4.34: a) Biocidal activities of Au@COL nanoparticles toward E. coli in the dark and under light irradiation. b) Inhibition ratio comparison bar chart in the dark and under light irradiation. Plate photographs for E. coli on YTD agar plate treated c) without the Au@COL nanoparticles in the dark (dark control), d) with the Au@COL nanoparticles in the dark, e) without the Au@COL nanoparticles under light irradiation (light control), f) with the Au@COL nanoparticles under light irradiation.

The COL nanoparticles-bacteria and Au@COL nanoparticles-bacteria interaction are further investigated with SEM and zeta potential. Figure 4.35 shows the SEM image of E. coli for the control experiment in the dark and under light irradiation. As can be seen, the light does not affect the bacteria and does not directly contribute to killing since the overall shape of light irradiated bacteria are the same as the bacteria in the dark.

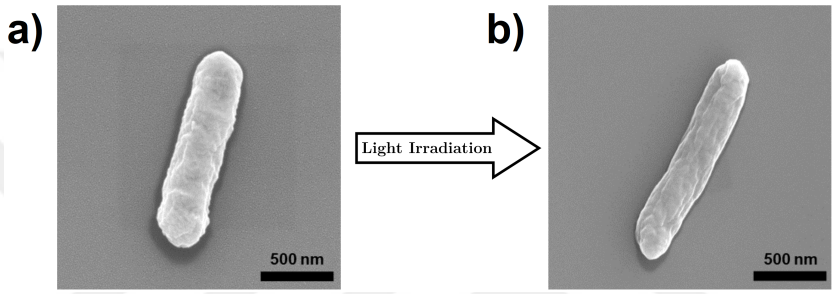


Figure 4.35: SEM images of E. coli. a) in the dark, b) under light irradiation.

Figure 4.36 depicts the bacteria treated with COL nanoparticles in the dark along under light irradiation. As it is shown in the figure, In the dark, the positively charge COL nanoparticles just have bonded to the wall of negatively charged E. coli and have not penetrated the cell. In under light irradiated bacteria, however, the COL nanoparticles have penetrated the wall of the E. coli shallowly. Although COL nanoparticles under light irradiation have penetrated the wall, there is no sign of rupturing or visible damage to the cell walls. This means that the PDT-Killing mechanism of the COL nanoparticles damage cell without rupturing the cell wall.

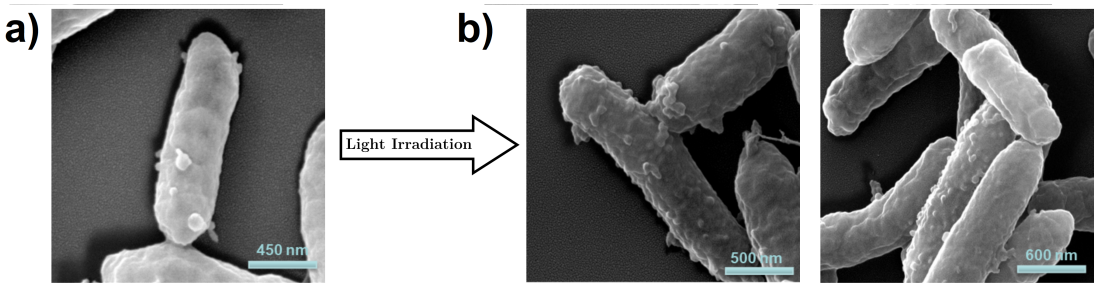


Figure 4.36: SEM images of E. coli treated a) with COL nanoparticles (5.5 μg/ml) in the dark, b) with COL nanoparticles (5.5 μg/ml) under light irradiation.

Figure 4.37 illustrates the bacteria treated with Au@COL nanoparticles in the dark along under light irradiation. As it is shown in the figure, In the dark, the positively charge Au@COL nanoparticles just have bonded to the wall of negatively charged E. coli and have not penetrated the cell. In under light irradiated bacteria, however, the Au@COL nanoparticles have penetrated deeply into the wall of the E. coli, and there are signs of rupturing and visible damage to the cell walls. It can be concluded that the PDT-Killing mechanism of Au@COL nanoparticles is different from the PDT-Killing mechanism of the COL nanoparticles. Au@COL nanoparticles damage the cell by rupturing the cell wall. From both the COL nanoparticles-bacteria and the Au@COL nanoparticles-bacteria interaction images, it can be concluded that the Au@COL nanoparticles killing mechanism is much more effective than the COL nanoparticles. This also implies that the effect of singlet oxygen provided by Au@COL nanoparticles will dominate the effect of singlet oxygen provided by the COL nanoparticles.

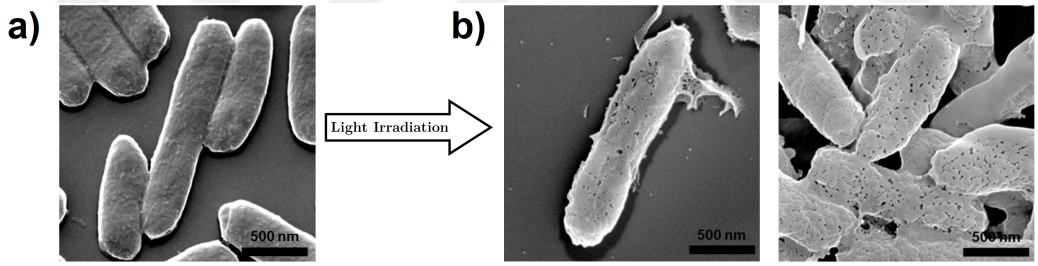


Figure 4.37: SEM images of E. coli treated a) with Au@COL nanoparticles (4.0 μg/ml) in the dark, b) with Au@COL nanoparticles (4.0 μg/ml) under light irradiation.

The antibacterial experiment results are further supported by zeta potential measurements. Since E. coli possesses a negative charge on its surface, its measured zeta potential is negative. If the bacteria has been killed, the calculated zeta potential is expected to be more positive (the magnitude of absolute zeta potential value will be smaller). It should also be mentioned that the changes in the surface of bacteria cause the drop in zeta potential value. Since in most of the cases killing is the counterpart of changes in the surface of bacteria, the drop in zeta potential value is considered as the sign of dead bacterial cell [132]. In some cases, although, the surface of bacteria is untouched, the bacteria are all or partially dead. The same scenario happened for the case of the COL

nanoparticles-bacteria treatment. Since the surface of bacteria is not changed much by COL nanoparticles, the zeta potential value dropped slightly. Figure 4.38 shows the results, which have been recorded in six different conditions. The decrease of zeta potential values in the dark for both the COL and Au@COL nanoparticles is negligible, which means the low dark toxicity of both structures. However, the decreases under light irradiation are much more significant. The drop in the case of treatment with Au@COL nanoparticles is more than the case of COL nanoparticles. This can be explained by different killing mechanisms of structures that end up in higher killing efficiency and more bacteria surface distortion in the case of Au@COL nanoparticles.

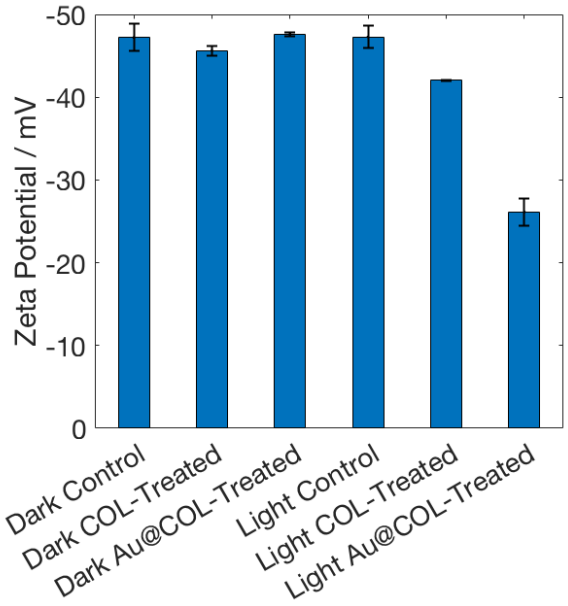


Figure 4.38: Zeta potential comparison bar chart of E. coli upon the addition of COL and Au@COL nanoparticles in the dark and under light irradiation (at 25 °C).

By referring to a higher decrease in absolute zeta potential value, higher inhibition ratio and biocidal activities, slightly higher singlet oxygen generation quantum yield and SEM images it can be concluded that the Au@COL nanoparticles outperform the COL nanoparticles in killing the E. coli by virtue of ME^1O_2,which results in higher singlet oxygen generation capacity.

Chapter 5

Conclusion

One-pot synthesis of hybrid core-shell nanoparticles (Au@COL) has been undertaken and optimized, and the resulted nanoparticles were fully characterized, and their application in antibacterial photodynamic therapy has been investigated. For synthesizing the Au@COL nanoparticles, different concentration ratios of gold to COL have been studied. Among all of the studied concentrations, the 1:2 (Au:COL) ratio showed the best properties in terms of morphology, stability, and performance in the application. The COL could spontaneously reduce the gold ions to zero-valent gold. The resulted Au@COL nanoparticles possess a positive charge on their surface, and their colloidal stability has been confirmed for at least six months. In this core-shell structure, the cores (gold nanoparticles) have been protected by a shell. The overall shape of core-shell nanoparticles are spherical and reported sizes with DLS, and TEM are 75 and 50 $\pm$10 nm, respectively. In comparison to COL dissolved in THF, the Au@COL nanoparticles in water own a higher Stokes shift, which is mostly caused by changes in polarity and dielectric constant of solvent and the chemical structure of COL. Changes in the chemical structure of COL have been evidenced with both the XPS and the FT-IR analysis. Changing the solvent from THF to water and changes in the chemical structure of the COL increased the contribution of non-radiative recombination significantly, which ended up with a substantial decrease

in the QY and fluorescence lifetime of Au@COL nanoparticles. The ROS measurements suggest that the Au@COL nanoparticles have a higher singlet oxygen generation capacity compared to COL nanoparticles as a result of ME^1O_2. The E. coli bacteria-killing efficiency of COL and Au@COL nanoparticles under light irradiation is 60% and 99.8%, respectively. The 40% hike in the inhibition ratio is the evidence of the contribution of gold nanoparticles (cores) in the therapy with an enhancing singlet oxygen generation capacity. With this being said, it can be concluded that Au@COL nanoparticles have successfully operated an enhanced antibacterial photodynamic therapy. They could compensate for the low PDT-killing efficiency of E. coli with COL nanoparticles and improve it up to 40%.

5.1 Future works

The core-shell structure is very tunable. With this in mind, by changing the configuration of core and shell, adding a new core or a new shell, the properties of the new core-shell structure can be altered dramatically. Since the COL could spontaneously reduce the silver ions, it possesses a reduction potential of at least 0.8 V. Considering this, theoretically other metals whose reduction potential is higher than 0.8 V can also be utilized as the core. Considerably high PDT-killing efficiency of Au@COL nanoparticles is convincing enough to consider using them in cell culture and cancer therapy. The Au@COL nanoparticles because of their remarkable properties, can also be utilized in photocatalysis applications. Also, more investigation may be planed to systematically study the nanostructure of these hybrid nanoparticles and conclusively clarify their architecture.

Bibliography

[1] Jaison Jeevanandam, Ahmed Barhoum, Yen S Chan, Alain Dufresne, and Michael K Danquah. Review on nanoparticles and nanostructured materials: history, sources, toxicity and regulations. *Beilstein Journal of Nanotechnology*, 9:1050–1074, April 2018.

[2] Jerome C. Glenn. Nanotechnology: Future military environmental health considerations. *Technological Forecasting and Social Change*, 73(2):128–137, February 2006.

[3] S.K. Sahoo, S. Parveen, and J.J. Panda. The present and future of nanotechnology in human health care. *Nanomedicine: Nanotechnology, Biology and Medicine*, 3(1):20–31, March 2007.

[4] Je Hulla, Sc Sahu, and Aw Hayes. Nanotechnology: History and future. *Human & Experimental Toxicology*, 34(12):1318–1321, December 2015.

[5] Donglu Shi, Zizheng Guo, and Nicholas Bedford. *Nanomaterials and devices*. Elsevier, WA, William Andrew is an imprint of Elsevier, Amsterdam ; Boston, 2015.

[6] Murielle A. Watzky and Richard G. Finke. Nanocluster size-control and "magic number" investigations. Experimental tests of the "living-metal polymer" concept and of mechanism-based size-control predictions leading to the syntheses of iridium(0) nanoclusters centering about four sequential magic numbers †. *Chemistry of Materials*, 9(12):3083–3095, December 1997.

[7] Hans-Dieter Beckhaus, Sergej Verevkin, Christoph Rüchardt, François Diederich, Carlo Thilgen, Hans-Ulrich ter Meer, Holger Mohn, and Wolfgang Müller. C70 is more stable than c60: experimental determination of the heat of formation of c70. *Angewandte Chemie International Edition in English*, 33(9):996–998, May 1994.

[8] Bo Feng, Zhixin Li, and Xing Zhang. Prediction of size effect on thermal conductivity of nanoscale metallic films. *Thin Solid Films*, 517(8):2803–2807, February 2009.

[9] Jahangeer Ahmed, Bharat Kumar, Amos M. Mugweru, Phong Trinh, Kandalam V. Ramanujachary, Samuel E. Lofland, and Ashok K. Ganguli. Binary fe-co alloy nanoparticles showing significant enhancement in electrocatalytic activity compared with bulk alloys. *The Journal of Physical Chemistry C*, 114(44):18779–18784, November 2010.

[10] Ph. Buffat and J-P. Borel. Size effect on the melting temperature of gold particles. *Physical Review A*, 13(6):2287–2298, June 1976.

[11] Munir H Nayfeh. *Fundamentals and Applications of Nano Silicon in Plasmonics and Fullerines: Current and Future Trends*. 2018. OCLC: 1042158898.

[12] Jianlu Zhang, editor. *PEM fuel cell testing and diagnosis*. Elsevier, Amsterdam ; Boston, 2013. OCLC: ocn828670774.

[13] Fuat Topuz and Tamer Uyar. RNA-mediated, green synthesis of palladium nanodendrites for catalytic reduction of nitroarenes. *Journal of Colloid and Interface Science*, 544:206–216, May 2019.

[14] V. Srikant and D. R. Clarke. On the optical band gap of zinc oxide. *Journal of Applied Physics*, 83(10):5447–5451, May 1998.

[15] Howard W. Starkweather, George E. Moore, John E. Hansen, Thomas M. Roder, and Richard E. Brooks. Effect of crystallinity on the properties of nylons. *Journal of Polymer Science*, 21(98):189–204, August 1956.

[16] Donald R. Baer, Mark H. Engelhard, Grant E. Johnson, Julia Laskin, Jinfeng Lai, Karl Mueller, Prabhakaran Munusamy, Suntharampillai Thevuthasan, Hongfei Wang, Nancy Washton, Alison Elder, Brittany L. Baisch, Ajay Karakoti, Satyanarayana V. N. T. Kuchibhatla, and DaeWon Moon. Surface characterization of nanomaterials and nanoparticles: Important needs and challenging opportunities. *Journal of Vacuum Science & Technology A: Vacuum, Surfaces, and Films*, 31(5):050820, September 2013.

[17] X. Wang, L. Yang, Z. Chen, and D. M. Shin. Application of nanotechnology in cancer therapy and imaging. *CA: A Cancer Journal for Clinicians*, 58(2):97–110, January 2008.

[18] Ranjita Misra, Sarbari Acharya, and Sanjeeb K. Sahoo. Cancer nanotechnology: application of nanotechnology in cancer therapy. *Drug Discovery Today*, 15(19-20):842–850, October 2010.

[19] Sumita B. Mitra, Dong Wu, and Brian N. Holmes. An application of nanotechnology in advanced dental materials. *The Journal of the American Dental Association*, 134(10):1382–1390, October 2003.

[20] W. Zhu, P. J. M. Bartos, and A. Porro. Application of nanotechnology in construction: Summary of a state-of-the-art report. *Materials and Structures*, 37(9):649–658, November 2004.

[21] Li Mu and Robert L. Sprando. Application of nanotechnology in cosmetics. *Pharmaceutical Research*, 27(8):1746–1749, August 2010.

[22] Xiaolei Qu, Pedro J.J. Alvarez, and Qilin Li. Applications of nanotechnology in water and wastewater treatment. *Water Research*, 47(12):3931–3946, August 2013.

[23] Tom O. McDonald, Marco Siccardi, Darren Moss, Neill Liptrott, Marco Giardiello, Steve Rannard, and Andrew Owen. The application of nanotechnology to drug delivery in medicine. In *Nanoengineering: Global Approaches to Health and Safety Issues*, pages 173–223. Elsevier, 2015.

[24] Thomas J Webster and Iustin Seil. Antimicrobial applications of nanotechnology: methods and literature. *International Journal of Nanomedicine*, page 2767, June 2012.

[25] Hung-Ju Yen, Changsheng Shan, Leeyih Wang, Ping Xu, Ming Zhou, and Hsing-Lin Wang. Development of Conjugated Polymers for Memory Device Applications. *Polymers*, 9(12):25, January 2017.

[26] Paul von Ragué Schleyer. Introduction: delocalizationpi and sigma. *Chemical Reviews*, 105(10):3433–3435, October 2005.

[27] F. Ebisawa, T. Kurokawa, and S. Nara. Electrical properties of polyacetylene/polysiloxane interface. *Journal of Applied Physics*, 54(6):3255–3259, June 1983.

[28] H. Letheby. XXIX.—On the production of a blue substance by the electrolysis of sulphate of aniline. *J. Chem. Soc.*, 15(0):161–163, 1862.

[29] Adam Pron and Patrice Rannou. Processible conjugated polymers: from organic semiconductors to organic metals and superconductors. *Progress in Polymer Science*, 27(1):135–190, February 2002.

[30] Akira Imamura and Yuriko Aoki. Molecular design of a pi-conjugated single-chain electronically conductive polymer. *International Journal of Quantum Chemistry*, 106(8):1924–1933, 2006.

[31] Alyssa B. Chinen, Chenxia M. Guan, Jennifer R. Ferrer, Stacey N. Barnaby, Timothy J. Merkel, and Chad A. Mirkin. Nanoparticle Probes for the Detection of Cancer Biomarkers, Cells, and Tissues by Fluorescence. *Chemical Reviews*, 115(19):10530–10574, October 2015.

[32] Xingfen Liu, Wei Huang, and Quli Fan. Water-soluble conjugated polymers for sensing and imaging applications. In Bin Liu Liu, editor, *Conjugated Polymers for Biological and Biomedical Applications*, pages 171–213. Wiley-VCH Verlag GmbH & Co. KGaA, Weinheim, Germany, March 2018.

[33] Liheng Feng, Chunlei Zhu, Huanxiang Yuan, Libing Liu, Fengting Lv, and Shu Wang. Conjugated polymer nanoparticles: preparation, properties,

functionalization and biological applications. *Chemical Society Reviews*, 42(16):6620, 2013.

[34] Filipe Vilela, Kai Zhang, and Markus Antonietti. Conjugated porous polymers for energy applications. *Energy & Environmental Science*, 5(7):7819, 2012.

[35] Guigang Zhang, Zhi-An Lan, and Xinchen Wang. Conjugated Polymers: Catalysts for Photocatalytic Hydrogen Evolution. *Angewandte Chemie International Edition*, 55(51):15712–15727, December 2016.

[36] Andrew C. Grimsdale, Khai Leok Chan, Rainer E. Martin, Pawel G. Jokisz, and Andrew B. Holmes. Synthesis of Light-Emitting Conjugated Polymers for Applications in Electroluminescent Devices. *Chemical Reviews*, 109(3):897–1091, March 2009.

[37] André Moliton and Roger C Hiorns. Review of electronic and optical properties of semiconducting pi-conjugated polymers: applications in optoelectronics. *Polymer International*, 53(10):1397–1412, October 2004.

[38] E. Smela. Conjugated Polymer Actuators for Biomedical Applications. *Advanced Materials*, 15(6):481–494, March 2003.

[39] Susie Eustis and Mostafa A. El-Sayed. Why gold nanoparticles are more precious than pretty gold: Noble metal surface plasmon resonance and its enhancement of the radiative and nonradiative properties of nanocrystals of different shapes. *Chem. Soc. Rev.*, 35(3):209–217, 2006.

[40] Huanjun Chen, Lei Shao, Qian Li, and Jianfang Wang. Gold nanorods and their plasmonic properties. *Chem. Soc. Rev.*, 42(7):2679–2724, 2013.

[41] Matthew Rycenga, Claire M. Cobley, Jie Zeng, Weiyang Li, Christine H. Moran, Qiang Zhang, Dong Qin, and Younan Xia. Controlling the Synthesis and Assembly of Silver Nanostructures for Plasmonic Applications. *Chemical Reviews*, 111(6):3669–3712, June 2011.

[42] George H. Chan, Jing Zhao, Erin M. Hicks, George C. Schatz, and Richard P. Van Duyne. Plasmonic Properties of Copper Nanoparticles

Fabricated by Nanosphere Lithography. *Nano Letters*, 7(7):1947–1952, July 2007.

[43] Christoph Langhammer, Zhe Yuan, Igor Zorić, and Bengt Kasemo. Plasmonic Properties of Supported Pt and Pd Nanostructures. *Nano Letters*, 6(4):833–838, April 2006.

[44] Davy Gérard and Stephen K Gray. Aluminium plasmonics. *Journal of Physics D: Applied Physics*, 48(18):184001, May 2015.

[45] Sotirios Baskoutas and Andreas F. Terzis. Size-dependent band gap of colloidal quantum dots. *Journal of Applied Physics*, 99(1):013708, January 2006.

[46] Matthew L. Landry, Thomas E. Morrell, Theodora K. Karagounis, Chih-Hao Hsia, and Chia-Ying Wang. Simple Syntheses of CdSe Quantum Dots. *Journal of Chemical Education*, 91(2):274–279, February 2014.

[47] Vincenzo Amendola, Roberto Pilot, Marco Frasconi, Onofrio M Maragò, and Maria Antonia Iatì. Surface plasmon resonance in gold nanoparticles: a review. *Journal of Physics: Condensed Matter*, 29(20):203002, May 2017.

[48] Xiao Wei Cao, Yang Kong, and Hong Can Shi. Sea Urchin-Like Gold Nanoparticles: Controllable Preparation and SERS Properties. *Key Engineering Materials*, 789:1–5, November 2018.

[49] K. Lance Kelly, Eduardo Coronado, Lin Lin Zhao, and George C. Schatz. The Optical Properties of Metal Nanoparticles: The Influence of Size, Shape, and Dielectric Environment. *The Journal of Physical Chemistry B*, 107(3):668–677, January 2003.

[50] Mahmoud A. Mahmoud, Maysamreza Chamanzar, Ali Adibi, and Mostafa A. El-Sayed. Effect of the Dielectric Constant of the Surrounding Medium and the Substrate on the Surface Plasmon Resonance Spectrum and Sensitivity Factors of Highly Symmetric Systems: Silver Nanocubes. *Journal of the American Chemical Society*, 134(14):6434–6442, April 2012.

[51] Nikolai G. Khlebtsov and Lev A. Dykman. Optical properties and biomedical applications of plasmonic nanoparticles. *Journal of Quantitative Spectroscopy and Radiative Transfer*, 111(1):1–35, January 2010.

[52] Suljo Linic, Phillip Christopher, and David B. Ingram. Plasmonic-metal nanostructures for efficient conversion of solar to chemical energy. *Nature Materials*, 10(12):911–921, December 2011.

[53] Alexander A. Kamnev, Lev A. Dykman, Petros A. Tarantilis, and Moschos G. Polissiou. Spectroimmunochemistry using colloidal gold bioconjugates. *Bioscience Reports*, 22(5/6):541–547, 2002.

[54] Roya Herizchi, Elham Abbasi, Morteza Milani, and Abolfazl Akbarzadeh. Current methods for synthesis of gold nanoparticles. *Artificial Cells, Nanomedicine, and Biotechnology*, 44(2):596–602, February 2016.

[55] Yu-Lin Su and Shang-Hsiu Hu. Functional Nanoparticles for Tumor Penetration of Therapeutics. *Pharmaceutics*, 10(4):193, October 2018.

[56] Vincenzo Amendola, Stefano Polizzi, and Moreno Meneghetti. Laser Ablation Synthesis of Gold Nanoparticles in Organic Solvents. *The Journal of Physical Chemistry B*, 110(14):7232–7237, April 2006.

[57] J. Kimling, M. Maier, B. Okenve, V. Kotaidis, H. Ballot, and A. Plech. Turkevich Method for Gold Nanoparticle Synthesis Revisited. *The Journal of Physical Chemistry B*, 110(32):15700–15707, August 2006.

[58] Sankar Kalidas Sivaraman, Sanjeev Kumar, and Venugopal Santhanam. Monodisperse sub-10nm gold nanoparticles by reversing the order of addition in Turkevich method – The role of chloroauric acid. *Journal of Colloid and Interface Science*, 361(2):543–547, September 2011.

[59] Nathan D. Burrows, Samantha Harvey, Fred A. Idesis, and Catherine J. Murphy. Understanding the Seed-Mediated Growth of Gold Nanorods through a Fractional Factorial Design of Experiments. *Langmuir*, 33(8):1891–1907, February 2017.

[60] Li-Ping Jiang, Shu Xu, Jian-Min Zhu, Jian-Rong Zhang, Jun-Jie Zhu, and Hong-Yuan Chen. Ultrasonic-Assisted Synthesis of Monodisperse Single-Crystalline Silver Nanoplates and Gold Nanorings. *Inorganic Chemistry*, 43(19):5877–5883, September 2004.

[61] Ji-Hwan Lee, Stephen U S Choi, Seok Jang, and Seoung Lee. Production of aqueous spherical gold nanoparticles using conventional ultrasonic bath. *Nanoscale Research Letters*, 7(1):420, 2012.

[62] I. M. Mahbubul, Tet Hien Chong, S. S. Khaleduzzaman, I. M. Shahrul, R. Saidur, B. D. Long, and M. A. Amalina. Effect of Ultrasonication Duration on Colloidal Structure and Viscosity of Alumina–Water Nanofluid. *Industrial & Engineering Chemistry Research*, 53(16):6677–6684, April 2014.

[63] Ping Xu, Xijiang Han, Bin Zhang, Yunchen Du, and Hsing-Lin Wang. Multifunctional polymer–metal nanocomposites via direct chemical reduction by conjugated polymers. *Chem. Soc. Rev.*, 43(5):1349–1360, 2014.

[64] V Tsakova, D Borissov, B Ranguelov, Ch Stromberg, and J.W Schultze. Electrochemical incorporation of copper in polyaniline layers. *Electrochimica Acta*, 46(26-27):4213–4222, August 2001.

[65] Yongliang Zhao, Zhi Chen, Xiaomin Zhu, and Martin Möller. A Facile One-Step Approach toward Polymer@SiO $_2$ Core–Shell Nanoparticles via a Surfactant-Free Miniemulsion Polymerization Technique. *Macromolecules*, 49(5):1552–1562, March 2016.

[66] S Srinivasan. The formation of titanium oxide monolayer coatings on silica surfaces. *Journal of Catalysis*, 131(1):260–275, September 1991.

[67] Hani Amouri, Christophe Desmarets, and Jamal Moussa. Confined Nanospaces in Metallocages: Guest Molecules, Weakly Encapsulated Anions, and Catalyst Sequestration. *Chemical Reviews*, 112(4):2015–2041, April 2012.

[68] Lincoln J. Lauhon, Mark S. Gudiksen, Deli Wang, and Charles M. Lieber. Epitaxial core–shell and core–multishell nanowire heterostructures. *Nature*, 420(6911):57–61, November 2002.

[69] Hye Hun Park, Kyoungja Woo, and Jae-Pyoung Ahn. Core–Shell Bimetallic Nanoparticles Robustly Fixed on the Outermost Surface of Magnetic Silica Microspheres. *Scientific Reports*, 3(1):1497, December 2013.

[70] Keun Sang Oh, Kyung Eun Lee, Sung Sik Han, Sun Hang Cho, Dongmin Kim, and Soon Hong Yuk. Formation of Core/Shell Nanoparticles with a Lipid Core and Their Application as a Drug Delivery System. *Biomacromolecules*, 6(2):1062–1067, March 2005.

[71] P. B. Shete, R. M. Patil, R. S. Ningthoujam, S. J. Ghosh, and S. H. Pawar. Magnetic core–shell structures for magnetic fluid hyperthermia therapy application. *New Journal of Chemistry*, 37(11):3784, 2013.

[72] Junyu Zhong, Chuanbao Cao, Youyong Liu, Yanan Li, and Waheed S. Khan. Hollow core–shell n-Fe2o3 microspheres with excellent lithium-storage and gas-sensing properties. *Chemical Communications*, 46(22):3869, 2010.

[73] Xingyi Huang and Pingkai Jiang. Core-Shell Structured High- k Polymer Nanocomposites for Energy Storage and Dielectric Applications. *Advanced Materials*, 27(3):546–554, January 2015.

[74] Youngjo Tak, Suk Joon Hong, Jae Sung Lee, and Kijung Yong. Fabrication of ZnO/CdS core/shell nanowire arrays for efficient solar energy conversion. *Journal of Materials Chemistry*, 19(33):5945, 2009.

[75] Chun-Ling Zhu, Mi-Lin Zhang, Ying-Jie Qiao, Gang Xiao, Fan Zhang, and Yu-Jin Chen. Fe $_3$ O $_4$ /TiO $_2$ Core/Shell Nanotubes: Synthesis and Magnetic and Electromagnetic Wave Absorption Characteristics. *The Journal of Physical Chemistry C*, 114(39):16229–16235, October 2010.

[76] Gang Xiao, Haijia Su, and Tianwei Tan. Synthesis of core–shell bioaffinity chitosan–TiO2 composite and its environmental applications. *Journal of Hazardous Materials*, 283:888–896, February 2015.

[77] Xiaoxiao Tan, Jinping Wang, Xiaojuan Pang, Li Liu, Qi Sun, Qing You, Fengping Tan, and Nan Li. Indocyanine Green-Loaded Silver Nanoparticle@Polyaniline Core/Shell Theranostic Nanocomposites for

Photoacoustic/Near-Infrared Fluorescence Imaging-Guided and Single-Light-Triggered Photothermal and Photodynamic Therapy. *ACS Applied Materials & Interfaces*, 8(51):34991–35003, December 2016.

[78] R. J. Hunter. "Colloidal systems and interfaces", by s. Ross and i. D. Morrison. 1st ed. (1988)Pp. Xviii + 422. John wiley and son, new york. Price $us 49. 95. *The Canadian Journal of Chemical Engineering*, 67(1):175–176, February 1989.

[79] Willem Norde. *Colloids and interfaces in life sciences and bionanotechnology*. CRC Press, Boca Raton, FL, 2nd rev. & expanded ed edition, 2011. OCLC: ocn432995212.

[80] J. Gregory. Introduction to modern colloid science, Robert J. Hunter. Oxford University Press, Oxford, 1993. pp. viii + 338, price £14.95 (Paperback). ISBN 0-19-855386-2. *Polymer International*, 35(1):105–106, September 1994.

[81] Yuncheng Liang and Jon Binner. Effect of triblock copolymer non-ionic surfactants on the rheology of 3 mol% yttria stabilised zirconia nanosuspensions. *Ceramics International*, 34(2):293–297, March 2008.

[82] Claudia Jacobs and Rainer Helmut Müller. Production and characterization of a budesonide nanosuspension for pulmonary administration. *Pharmaceutical Research*, 19(2):189–194, 2002.

[83] Jerry Z. Yang, Anthony L. Young, Po-Chang Chiang, Archie Thurston, and Denise K. Pretzer. Fluticasone and budesonide nanosuspensions for pulmonary delivery: Preparation, characterization, and pharmacokinetic studies. *Journal of Pharmaceutical Sciences*, 97(11):4869–4878, November 2008.

[84] M Sato, Y Watanabe, S Ueda, S Iseki, Y Abe, N Sato, S Kimura, K Okubo, and M Onji. Microwave coagulation therapy for hepatocellular carcinoma. *Gastroenterology*, 110(5):1507–1514, May 1996.

[85] Feng Wu, Wen-Zhi Chen, Jin Bai, Jian-Zhong Zou, Zhi-Long Wang, Hui Zhu, and Zhi-Biao Wang. Pathological changes in human malignant carcinoma treated with high-intensity focused ultrasound. *Ultrasound in Medicine & Biology*, 27(8):1099–1106, August 2001.

[86] Frederick W. Kremkau. Cancer therapy with ultrasound: A historical review. *Journal of Clinical Ultrasound*, 7(4):287–300, August 1979.

[87] G. Scott Gazelle, S. Nahum Goldberg, Luigi Solbiati, and Tito Livraghi. Tumor Ablation with Radio-frequency Energy. *Radiology*, 217(3):633–646, December 2000.

[88] S. Nahum Goldberg and Damian E. Dupuy. Image-guided Radiofrequency Tumor Ablation: Challenges and Opportunities—Part I. *Journal of Vascular and Interventional Radiology*, 12(9):1021–1032, September 2001.

[89] Lars O. Svaasand, Charles J. Gomer, and Elisa Morinelli. On the physical rationale of laser induced hyperthermia. *Lasers in Medical Science*, 5(2):121–128, June 1990.

[90] A. C. Steger, W. R. Lees, K. Walmsley, and S. G. Bown. Interstitial laser hyperthermia: a new approach to local destruction of tumours. *BMJ*, 299(6695):362–365, August 1989.

[91] R. Anderson and J. Parrish. Selective photothermolysis: precise microsurgery by selective absorption of pulsed radiation. *Science*, 220(4596):524–527, April 1983.

[92] A. Welch. The thermal response of laser irradiated tissue. *IEEE Journal of Quantum Electronics*, 20(12):1471–1481, December 1984.

[93] Giulio Jori and John D. Spikes. Photothermal sensitizers: Possible use in tumor therapy. *Journal of Photochemistry and Photobiology B: Biology*, 6(1-2):93–101, June 1990.

[94] Vladimir P. Zharov, Elena N. Galitovskaya, Carl Johnson, and Thomas Kelly. Synergistic enhancement of selective nanophotothermolysis with gold

nanoclusters: Potential for cancer therapy. *Lasers in Surgery and Medicine*, 37(3):219–226, September 2005.

[95] Boris Khlebtsov, Vladimir Zharov, Andrei Melnikov, Valery Tuchin, and Nikolai Khlebtsov. Optical amplification of photothermal therapy with gold nanoparticles and nanoclusters. *Nanotechnology*, 17(20):5167–5179, October 2006.

[96] Barbara W. Henderson and Thomas J. Dougherty. HOW DOES PHOTODYNAMIC THERAPY WORK? *Photochemistry and Photobiology*, 55(1):145–157, January 1992.

[97] T. J. Dougherty, C. J. Gomer, B. W. Henderson, G. Jori, D. Kessel, M. Korbelik, J. Moan, and Q. Peng. Photodynamic Therapy. *JNCI Journal of the National Cancer Institute*, 90(12):889–905, June 1998.

[98] Michael H. Gold. Introduction to Photodynamic Therapy: Early Experience. *Dermatologic Clinics*, 25(1):1–4, January 2007.

[99] Laura Villén, Francisco Manjón, David García-Fresnadillo, and Guillermo Orellana. Solar water disinfection by photocatalytic singlet oxygen production in heterogeneous medium. *Applied Catalysis B: Environmental*, 69(1-2):1–9, December 2006.

[100] Wenbo Wu, Duo Mao, Shidang Xu, Kenry, Fang Hu, Xueqi Li, Deling Kong, and Bin Liu. Polymerization-Enhanced Photosensitization. *Chem*, 4(8):1937–1951, August 2018.

[101] Melis Özkan, Yağmur Keser, Seyed Ehsan Hadi, and Dönüs Tuncel. A [5]Rotaxane-Based Photosensitizer for Photodynamic Therapy: A [5]Rotaxane-Based Photosensitizer for Photodynamic Therapy. *European Journal of Organic Chemistry*, 2019(21):3534–3541, June 2019.

[102] Denis Girard, Glenn Weagle, Atul Gupta, Gervais Bérubé, and Camille Chapados. Preparation and in vitro biological evaluation of tetrapyrrole ethanolamide derivatives as potential anticancer agents. *Bioorganic & Medicinal Chemistry Letters*, 18(1):360–365, January 2008.

[103] Denise Bechet, Pierre Couleaud, Céline Frochot, Marie-Laure Viriot, François Guillemin, and Muriel Barberi-Heyob. Nanoparticles as vehicles for delivery of photodynamic therapy agents. *Trends in Biotechnology*, 26(11):612–621, November 2008.

[104] J. W. Verhoeven. Glossary of terms used in photochemistry (IUPAC Recommendations 1996). *Pure and Applied Chemistry*, 68(12):2223–2286, January 1996.

[105] Xingxing Sun, Xijun Wang, Xinyang Li, Jing Ge, Qun Zhang, Jun Jiang, and Guoqing Zhang. Polymerization-Enhanced Intersystem Crossing: New Strategy to Achieve Long-Lived Excitons. *Macromolecular Rapid Communications*, 36(3):298–303, February 2015.

[106] Wenbo Wu, Duo Mao, Shidang Xu, Shenglu Ji, Fang Hu, Dan Ding, Deling Kong, and Bin Liu. High performance photosensitizers with aggregation-induced emission for image-guided photodynamic anticancer therapy. *Materials Horizons*, 4(6):1110–1114, 2017.

[107] Ursula Theuretzbacher. Global antibacterial resistance: The never-ending story. *Journal of Global Antimicrobial Resistance*, 1(2):63–69, June 2013.

[108] Henrik Krarup Nielsen, Javier Garcia, Michael Væth, and Sebastian Schlafer. Comparison of Riboflavin and Toluidine Blue O as Photosensitizers for Photoactivated Disinfection on Endodontic and Periodontal Pathogens In Vitro. *PLOS ONE*, 10(10):e0140720, October 2015.

[109] Nicolas Macia, Roger Bresoli-Obach, Santi Nonell, and Belinda Heyne. Hybrid Silver Nanocubes for Improved Plasmon-Enhanced Singlet Oxygen Production and Inactivation of Bacteria. *Journal of the American Chemical Society*, 141(1):684–692, January 2019.

[110] Kadir Aslan, Meng Wu, Joseph R. Lakowicz, and Chris D. Geddes. Fluorescent Core/Shell Ag@SiO $_2$ Nanocomposites for Metal-Enhanced Fluorescence and Single Nanoparticle Sensing Platforms. *Journal of the American Chemical Society*, 129(6):1524–1525, February 2007.

[111] Yongxia Zhang, Kadir Aslan, Michael J. R. Previte, Stuart N. Malyn, and Chris D. Geddes. Metal-Enhanced Phosphorescence: Interpretation in Terms of Triplet-Coupled Radiating Plasmons. *The Journal of Physical Chemistry B*, 110(49):25108–25114, December 2006.

[112] Yongxia Zhang, Kadir Aslan, Stuart N. Malyn, and Chris D. Geddes. Metal-enhanced phosphorescence (MEP). *Chemical Physics Letters*, 427(4-6):432–437, August 2006.

[113] Yongxia Zhang, Kadir Aslan, Michael J. R. Previte, and Chris D. Geddes. Metal-enhanced Singlet Oxygen Generation: A Consequence of Plasmon Enhanced Triplet Yields. *Journal of Fluorescence*, 17(4):345–349, July 2007.

[114] Zachary R. Stromberg, Angelica Van Goor, Graham A. J. Redweik, Meghan J. Wymore Brand, Michael J. Wannemuehler, and Melha Mellata. Pathogenic and non-pathogenic *Escherichia coli* colonization and host inflammatory response in a defined microbiota mouse model. *Disease Models & Mechanisms*, 11(11):dmm035063, November 2018.

[115] Laurent Poirel, Jean-Yves Madec, Agnese Lupo, Anne-Kathrin Schink, Nicolas Kieffer, Patrice Nordmann, and Stefan Schwarz. Antimicrobial Resistance in Escherichia coli. *Microbiology Spectrum*, 6(4), August 2018.

[116] Stephanie Brown, John P. Santa Maria, and Suzanne Walker. Wall Teichoic Acids of Gram-Positive Bacteria. *Annual Review of Microbiology*, 67(1):313–336, September 2013.

[117] Felipe F Sperandio, Ying-Ying Huang, and Michael R Hamblin. Antimicrobial Photodynamic Therapy to Kill Gram-negative Bacteria. *Recent patents on anti-infective drug discovery*, 8(2):108–120, August 2013.

[118] Timuçin Balkan, Seda Kizir, and Dönüs Tuncel. One-Pot Synthesis of Hybrid Conjugated Oligomer-Ag Nanoparticles. *ACS Omega*, 2(9):5470–5477, September 2017.

[119] Mehmet Gumustas, Ceyda T. Sengel-Turk, Aysen Gumustas, Sibel A. Ozkan, and Bengi Uslu. Effect of Polymer-Based Nanoparticles on the Assay of Antimicrobial Drug Delivery Systems. In *Multifunctional Systems for Combined Delivery, Biosensing and Diagnostics*, pages 67–108. Elsevier, 2017.

[120] Graham Hungerford, Archie Allison, David McLoskey, Marina K. Kuimova, Gokhan Yahioglu, and Klaus Suhling. Monitoring Sol-to-Gel Transitions via Fluorescence Lifetime Determination Using Viscosity Sensitive Fluorescent Probes. *The Journal of Physical Chemistry B*, 113(35):12067–12074, September 2009.

[121] William D. Pyrz and Douglas J. Buttrey. Particle Size Determination Using TEM: A Discussion of Image Acquisition and Analysis for the Novice Microscopist. *Langmuir*, 24(20):11350–11360, October 2008.

[122] Julie L. Fenton, James M. Hodges, and Raymond E. Schaak. Synthetic Deconvolution of Interfaces and Materials Components in Hybrid Nanoparticles. *Chemistry of Materials*, 29(14):6168–6177, July 2017.

[123] B.J. Inkson. Scanning electron microscopy (SEM) and transmission electron microscopy (TEM) for materials characterization. In *Materials Characterization Using Nondestructive Evaluation (NDE) Methods*, pages 17–43. Elsevier, 2016.

[124] Tuncer M. Kuzay, Michael Kazmierczak, and B. J. Hsieh. X-ray beam/biomaterial thermal interactions in third-generation synchrotron sources. *Acta Crystallographica Section D Biological Crystallography*, 57(1):69–81, January 2001.

[125] Jousheed Pennakalathil, Ermira Jahja, E. Sıla Özdemir, Özlen Konu, and Dönüs Tuncel. Red Emitting, Cucurbituril-Capped, pH-Responsive Conjugated Oligomer-Based Nanoparticles for Drug Delivery and Cellular Imaging. *Biomacromolecules*, 15(9):3366–3374, September 2014.

[126] G. A. Pankuch, G. Lin, D. B. Hoellman, C. E. Good, M. R. Jacobs, and P. C. Appelbaum. Activity of Retapamulin against Streptococcus pyogenes and Staphylococcus aureus Evaluated by Agar Dilution, Microdilution, E-Test, and Disk Diffusion Methodologies. *Antimicrobial Agents and Chemotherapy*, 50(5):1727–1730, May 2006.

[127] Kai Liu, Yiliu Liu, Yuxing Yao, Huanxiang Yuan, Shu Wang, Zhiqiang Wang, and Xi Zhang. Supramolecular Photosensitizers with Enhanced Antibacterial Efficiency. *Angewandte Chemie International Edition*, 52(32):8285–8289, August 2013.

[128] Ludovic Bourré, Sonia Thibaut, Amélie Briffaud, Nathalie Rousset, Sabine Eléouet, Youenn Lajat, and Thierry Patrice. Indirect detection of photosensitizer ex vivo. *Journal of Photochemistry and Photobiology B: Biology*, 67(1):23–31, May 2002.

[129] M. K. Fung, S. L. Lai, S. W. Tong, S. N. Bao, C. S. Lee, W. W. Wu, M. Inbasekaran, J. J. O'Brien, and S. T. Lee. Distinct interfaces of poly (9,9-dioctylfluorene-co-benzothiadiazole) with cesium and calcium as observed by photoemission spectroscopy. *Journal of Applied Physics*, 94(9):5763–5770, November 2003.

[130] Nancy Tawil, Edward Sacher, Etienne Boulais, Rosemonde Mandeville, and Michel Meunier. X-ray Photoelectron Spectroscopic and Transmission Electron Microscopic Characterizations of Bacteriophage–Nanoparticle Complexes for Pathogen Detection. *The Journal of Physical Chemistry C*, 117(40):20656–20665, October 2013.

[131] Manohar A. Bhosale, Divya R. Chenna, Jayendra P. Ahire, and Bhalchandra M. Bhanage. Morphological study of microwave-assisted facile synthesis of gold nanoflowers/nanoparticles in aqueous medium and their catalytic application for reduction of p-nitrophenol to p-aminophenol. *RSC Advances*, 5(65):52817–52823, 2015.

[132] Suman Halder, Kirendra Kumar Yadav, Ratul Sarkar, Sudipta Mukherjee, Pritam Saha, Saubhik Haldar, Sanmoy Karmakar, and Tuhinadri Sen. Alteration of Zeta potential and membrane permeability in bacteria: a study with cationic agents. *SpringerPlus*, 4(1):672, December 2015.